2013

Modeling And Simulation Of All-electric Aircraft Power Generation And Actuation

David Woodburn
University of Central Florida

STARS Citation

Woodburn, David, "Modeling And Simulation Of All-electric Aircraft Power Generation And Actuation" (2013). *Electronic Theses and Dissertations, 2004-2019*. 2798.
https://stars.library.ucf.edu/etd/2798

MODELING AND SIMULATION OF ALL-ELECTRIC AIRCRAFT POWER GENERATION AND ACTUATION

by

DAVID ANDREW WOODBURN
B.S. John Brown University, 2004
M.S. University of Central Florida, 2010

A dissertation submitted in partial fulfillment of the requirements for
the degree of Doctor of Philosophy
in the Department of Electrical Engineering and Computer Science
in the College of Engineering and Computer Science
at the University of Central Florida
Orlando, Florida

Fall Term
2013

Major Professor: Thomas X. Wu

ABSTRACT

Modern aircraft, military and commercial, rely extensively on hydraulic systems. However, there is great interest in the avionics community to replace hydraulic systems with electric systems. There are physical challenges to replacing hydraulic actuators with electromechanical actuators (EMAs), especially for flight control surface actuation. These include dynamic heat generation and power management.

Simulation is seen as a powerful tool in making the transition to all-electric aircraft by predicting the dynamic heat generated and the power flow in the EMA. Chapter 2 of this dissertation describes the nonlinear, lumped-element, integrated modeling of a permanent magnet (PM) motor used in an EMA. This model is capable of representing transient dynamics of an EMA, mechanically, electrically, and thermally.

Inductance is a primary parameter that links the electrical and mechanical domains and, therefore, is of critical importance to the modeling of the whole EMA. In the dynamic mode of operation of an EMA, the inductances are quite nonlinear. Chapter 3 details the careful analysis of the inductances from finite element software and the mathematical modeling of these inductances for use in the overall EMA model.

Chapter 4 covers the design and verification of a nonlinear, transient simulation model of a two-step synchronous generator with three-phase rectifiers. Simulation results are shown.

To God from whom all good gifts come.

ACKNOWLEDGMENTS

This dissertation is the culmination of many years of research and hard work. But, it was not done in a vacuum. I have benefited tremendously from the help and guidance of many others.

I am deeply grateful for the patient and caring guidance of my adviser and committee chair, Professor Thomas Xinzhang Wu. His intelligence, insight, and wisdom have helped me develop, mature, and excel. His attitude toward research has built in me an enjoyment for the work. I would not have reached this point without his help.

I would like to thank my other committee members for their help and support: Dr. M. Georgiopoulos, Dr. M. Haralambous, Dr. I. Batarseh, and Dr. L. Chow. I am especially grateful for the significant help, support, and guidance of Dr. Chow.

I want to thank my lab mates through the years for their input and insights: Tony Camarano, Yang Hu, Shaohua Lin, Hanzhou Liu, Shan Wan, Kejiu Zhang, Jared Bindl, Wendell Brokaw, and Chih-Hang Wu. I also want to thank Lei Zhou, Yeong-Ren Lin, Nicholas Rolinski, and Justin DelMar for their help with experimentation.

I am deeply grateful for the continual support of my parents. They have been there for me from beginning to end.

Finally, I want to thank my wife for her supportive heart and understanding attitude as I worked to finish my degree.

This material is based on research sponsored by Air Force Research Laboratory under agreement number FA8650-09-2-2940. The U.S. Government is authorized to reproduce and distribute reprints for Governmental purposes notwithstanding any copyright notation thereon.

TABLE OF CONTENTS

LIST OF FIGURES

LIST OF TABLES

LIST OF ACRONYMS

DQ0	Direct-quadrature-zero
EMA	Electromechanical actuator
FEM	Finite element method
FOC	Field oriented control
PM	Permanent magnet
PWM	Pulse width modulation
SM	Synchronous machine

CHAPTER ONE: INTRODUCTION

Objective

The heat loads in an electromechanical actuator (EMA) and the electrical power demands of an EMA system are both highly transient; therefore, thermal and electrical modeling designed for time-averaged, steady-state behavior are inadequate. The heat loads and power demands of EMAs must be accurately known before EMAs can be trusted as replacements to current hydraulic actuators in controlling flight surfaces on aircraft. Therefore, a comprehensive, nonlinear, dynamic simulation model including electromagnetics with non-linearities, rotor dynamics, power electronics, control, and heat transfer thermodynamics are designed for an EMA.

The second chapter details the comprehensive analysis of the EMA simulation model and includes experimental validation. The third chapter focuses on how the nonlinear inductances of the EMA's electric motor are obtained from finite element method (FEM) and how a mathematical model is developed to fit the tables of inductance data. These inductance formulas can be used in the full EMA simulation model of the second chapter. The third chapter includes a comparison of running the full simulation using the nonlinear inductance formulas versus running the simulation using scalar values.

Using [1] extensively, the rest of this chapter details the motivation for this research and an overview of the work done.

The All-Electric Aircraft (AEA) Concept

System-level benefits

Current airplanes use a combination of pneumatic, hydraulic, and electric systems. It is expected that future airplanes will just have an electric system. Such all-electric aircraft (AEA) would use electric power exclusively for onboard systems [2]. Some of the expected benefits are the following [1], [3]-[5]:

- Improved aircraft maintainability
    - No hydraulic components
    - Faster aircraft turnaround
    - Fewer necessary tools and spares
    - Better fault-diagnosis through built-in testing (BIT)
- Improved system availability and reliability
    - More easily reconfigurable – Electrical distribution is more practical and offers system reconfiguration flexibility (a capability previously difficult to achieve using hydraulics).
    - Improved mean time between failures (MTBF)
- Improved flight safety – avoiding common-mode failures by using dissimilar power supplies
- Reduced system weight – Electric actuators would replace not just the hydraulic actuators but their entire hydraulic system, including pumps, distribution networks (pipes and fluid), and valve blocks.
- Reduction of aircraft operating costs – reduced fuel consumption from reduced weight; reduced maintenance costs

Unit-level benefits

As seen above, the primary advantages of EMAs over current actuators are in the comparison of the entire systems, rather than the units themselves. However, the EMA unit itself does have a number of advantages:

- EMAs are more energy efficient than hydraulic systems in that EMAs only require energy when force is required [6]. Hydraulic systems must keep running just to maintain line pressure. Hydraulic transmissions also incur energy losses from pumping [7].
- EMAs lack hydraulic fluid, which can leak, is corrosive, and is a fire hazard. Without hydraulic fluid, EMAs can be simpler to install and maintain.
- EMAs tend to be stiffer than hydraulics. This happens because hydraulic transmissions have an elastic quality that EMAs lack.

Predicted progress

In spite of the benefits of an all-electric aircraft, there is no aircraft that fulfills this goal yet. However, when an AEA is realized, it will likely happen in the following order [5]:

- Stage 1: Electro-hydrostatic actuators (EHAs) serve as auxiliary to standard hydraulic actuators.
- Stage 2: EHAs operate as primary control actuators.
- Stage 3: Electromechanical actuator (EMA) technology improves in the areas of thermal management, power density, and jam tolerance. Aircraft power generation systems advance to support the very high electrical demands.
- Stage 4: EMAs serve as auxiliary to EHAs.
- Stage 5: EMAs operate as both primary and auxiliary control actuators.

Given that the commercial aircraft Airbus A380 uses electro-hydrostatic backup actuators (EHBA) in its flight control system, it is safe to say that the first stage has been accomplished. The assumption is that with experience of EHAs in flight control systems, EHAs will naturally progress to being used as primary control actuators. Clearly, overcoming current deficiencies of EMA technology will require significant research during the third stage. Success at this stage would make it possible for EMAs to be introduced in commercial aircraft by the fourth stage, and subsequently to become the exclusive control actuators by the fifth stage. So, at this point, a primary focus must be overcoming the deficiencies of EMA technology.

EMA Development Challenges

EMAs have been shown to match the performance of hydraulic actuators by flight tests from several research programs [8]. However, whether the current EMAs are suitable as the primary flight control is still debated [4]. The development of EMAs has three remaining major challenges: increasing power density, increasing jam tolerance, and resolving thermal management. These issues must each be solved before EMAs can replace hydraulics as primary flight control actuators.

First, as experience with actuators grows and designs of power electronics and electric motors are enhanced, the power density (power per unit mass) of EMAs will certainly increase. Though an EMA system already has the potential of being lighter than a hydraulic system, this power density increase will make the EMA actuators themselves more competitive with hydraulic actuators in weight.

Typically, an EMA mechanical transmission has dozens of gear teeth, the failure of any one of which can cause critical jamming, the second major challenge. An EMA must be able to bypass this failure by some means, such as including several transmission paths, or by removing the gearbox altogether and using a low-speed, high-torque “direct drive,” a currently investigated alternative [9].

The third major challenge to developing a high-power, flight worthy EMA system is thermal management. The heat generated by an EMA system can easily be enough to cause failure. Already, the environment for which the EMA system must be designed ranges from -40 °C to 125 °C. Furthermore, the actuator and its electronics do not offer a convenient path for heat transfer. So, either new approaches to heat transfer must be developed or the actuator and its surrounding structure must be designed to operate properly at higher temperatures.

EMAs can be used on the ailerons, elevators, spoilers, and rudder, the primary flight control surfaces of an aircraft. EMAs also can be used for the propulsion system actuation and secondary functions such as landing gear and high-lift devices. However, thermal management makes primary flight control surfaces, which are in continuous use, much more critical than secondary actuators, which required only intermittent use allowing plenty of time for heat to dissipate. Features important to the military for their strike aircraft, such as high acceleration maneuvering loads and inverted or supersonic flight, further increase the demands on thermal management system designs. If EMAs are to enter stage four and succeed EHAs as the primary actuators, heat generation must be well understood. Consequently, dynamic heat generation in EMAs is one of the most important research areas in the mission of all-electric aircraft.

Heat Generation

An EMA couples an electric motor to a load, such as a flight control surface, using mechanical gearing, such as a rotary gearbox, and may use a ball screw (Figure 1) or roller screw.

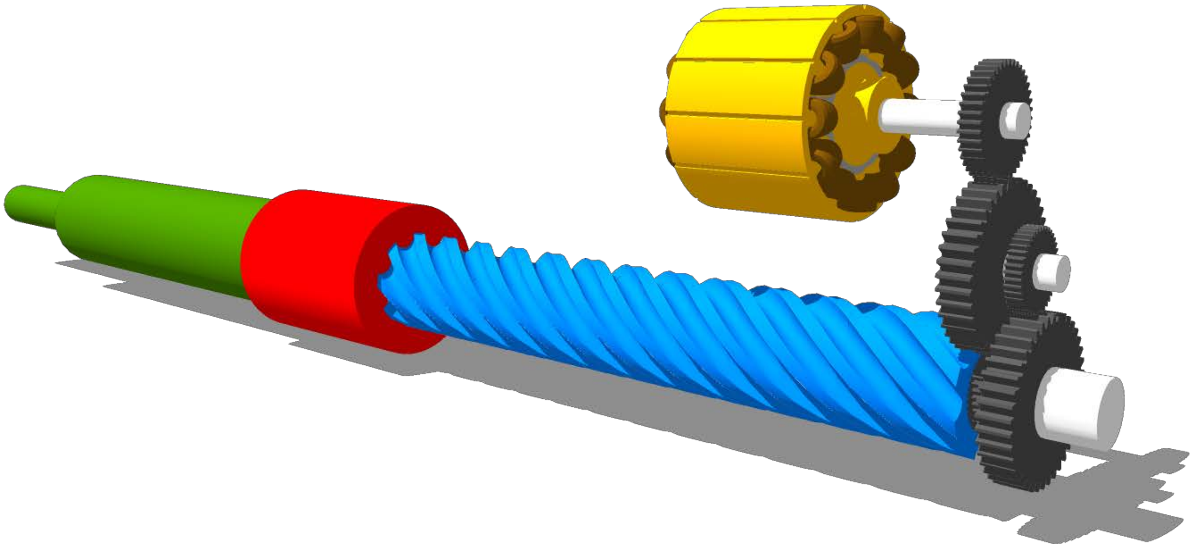

Figure 1. Guts of an electromechanical actuator [4] showing the motor (yellow) with its windings, the gears (gray) of the gear box, the screw (blue) of the ball screw, the ball housing (red) of the ball screw, and the rod (green) into which the screw slides.

Figure 2 shows the block diagram of an EMA system (Iden, Lockheed Martin Company, 2005). The EMA has three major sources of heat: the motor, the power electronics inside the electronic unit (EU), and the gearbox. In steady-state operation, the efficiency is typically 93% for the power electronics, 80% for the motor, and 80% for the gearbox. It should be noted that the actual heat generation is highly transient and localized in nature. Quantifying these transient power losses and the temperature distribution is a key objective of this research.

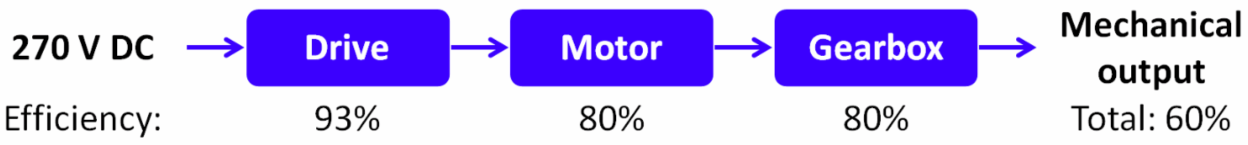

Figure 2. Block diagram of an EMA system

Generally, gearboxes and ball screws are temperature insensitive [10]. The electric motor is probably the most temperature-sensitive component. The thermal resistance of the air gap between the stator and the rotor makes dissipating heat from the rotor difficult. However, switched-reluctance motors (SRM) and permanent magnet (PM) motors both lack rotor windings, thereby preventing heat-buildup from copper losses on the rotor altogether [10].

Motor losses mainly come from the copper winding losses and magnetic material losses (hysteresis and eddy current losses). Since ball screws are very efficient and have low friction, even when the EMA is not moving, current must still be supplied to the motor stator to provide a torque balance for the load and to keep the EMA from being back-driven. Therefore, heat will still be generated even when nothing is moving. FEM is done on the motor design to analyze the heat flow and determine thermal lumped-element parameters (Figure 3).

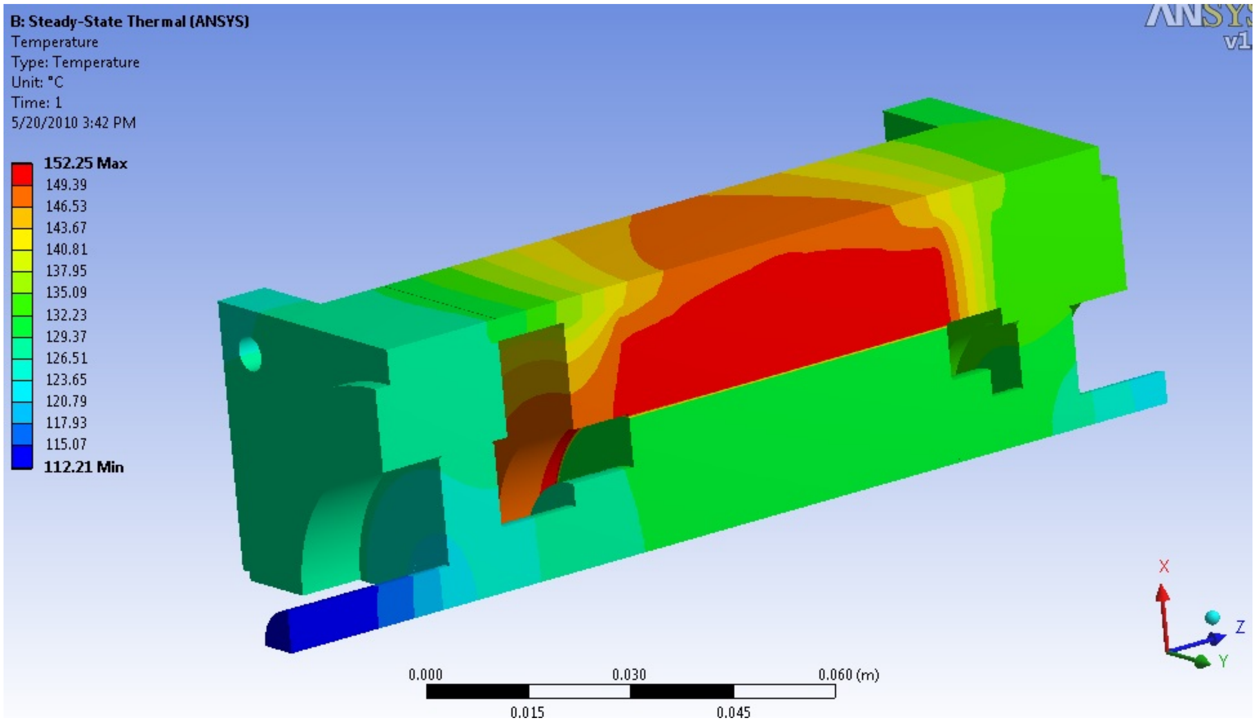

Figure 3. FEM diagram of a quarter of a PM motor showing the temperature distribution during a simulation.

High operating temperatures lead to the following problems in motors [10]:

- The insulation melts, leading to electrical shorts (a catastrophic failure)
- The copper resistivity increases, generating more heat and further reducing efficiency (a reversible problem)
- The magnetic permeability decreases (a gradual, but irreversible failure), further increasing magnetic losses and reducing efficiency.

The power electronics in the EU, controlling the direction and speed of the motor [4], generate heat mostly in the semiconductors. Semiconductors generate heat in four major ways [11]:

- On or off switching losses. At high switching frequencies, as are necessary in motor control, this heat contribution becomes significant.
- Resistive losses of forward conduction
- Leakage losses in off mode. Some current from the blocked voltage gets through.
- Control terminal contact losses of the semiconductor

The combined heat from these effects is significant [4], often of the same order of magnitude as from the motor [12], [13], and, unless removed, could irreversibly damage the electronics [4]. Even though electronics can survive high transient temperatures, their mean time between failures (MTBF) is considerably reduced.

Besides heat from semiconductor power devices, heat can also be generated from the copper traces and the magnetic components (winding and core losses) on the power electronics board. These losses are even greater during a transient current surge.

Simulation

Accurately modeling heat generation, including transients, is important in developing good thermal management of the whole EMA system. Transient heat-generation simulation of an EMA system involves comprehensive multi-physics, multi-scale, and multi-domain simulation efforts. The procedure can be divided into two steps.

First, critical simulation parameters for the EMA are obtained. Some parameters are obtained through experimentation. For others, experimentation would be either very difficult or impractical. In such cases, FEM simulations of the PM motor can provide accurate information. FEM simulations of the magnetic field distribution of the motor are used to find the nonlinear self and mutual-inductances of the three-phase windings. Figure 4 shows an example PM motor in a 2D cross-sectional view with the magnetic flux density distribution.

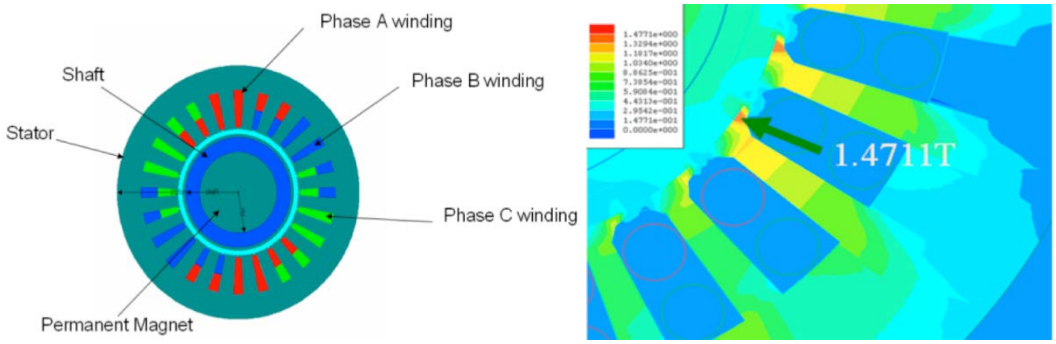

Figure 4. Cross-sectional view of a PM (left) and magnetic flux density distribution (right)

Because FEM simulations for inductances are very time-consuming, the simulations are done on 2D cross-sections of the motor. This is an accurate approach since for a motor with a small radius to length ratio the edge effects do not significantly influence the simulation results.

In the system simulation, the motor is integrated in a complete system that consists of an input voltage source, various load conditions, a feedback control scheme, etc. Rotor dynamics are also included in the system dynamical equations. Instead of using empirical formula calculations, the flux linkage and inductances of the motor can be extracted from the FEM model, where EM field effects have been taken into account. Therefore, the motor dynamic model is very accurate.

Transient heat transfer simulation using FEM is performed on the motor. Because thermal simulations do not require mesh resolutions nearly as detailed as those of electrical simulations, the thermal simulations run much faster. Therefore, the thermal simulations are performed on 3D segments of the motor. Once, simulation data is obtained, correlations between input heat and output nodal temperatures can be made to derive thermal resistances and capacitances. These values are then used in a lumped-element thermal network within the full EMA simulation model.

Second, a nonlinear, lumped-element model (NLEM) is built and the previously obtained parameters are used in the model. This approach provides the high accuracy of FEM with the simulation speed of lumped-element modeling.

Chapter 2 details the overall simulation model. It explains how the model is designed, how many of its parameters are obtained, and how the various components, such as the thermal network, interact. It also shows how the model performs when a full simulation is run.

Chapter 3 details the development of the nonlinear inductance formulas that are used in the overall simulation model of the EMA. This represents a large portion of the work and one of the most critical components of the model. This chapter explains in detail how FEM is used to get tables of inductances, how that data is correlated with currents, and how a formula is fitted to the data.

Chapter 4 covers the design and verification of a nonlinear, transient simulation model of a two-step synchronous generator with three-phase, full-wave rectifiers. A new magnetics model is developed and compared to FEM data of a synchronous machine. Simulation results are included.

Finally, Chapter 5 concludes the dissertation. This work covers the primary components involved in an all-electric aircraft system.

CHAPTER TWO: DYNAMIC HEAT GENERATION MODELING OF HIGH-PERFORMANCE ELECTROMECHANICAL ACTUATOR

Introduction

The development of all-electric aircraft is a high priority in the avionics community [1]. Current aircraft use a combination of hydraulic, pneumatic, and electric systems. However, future airplanes are expected to use a single, electric system, with electromechanical actuators (EMAs) replacing hydraulic pistons. Such a system would reduce the cost to build, operate, and maintain aircraft [15]. It would also make aircraft lighter, more reliable, safer, and more easily reconfigurable, improving the turnaround for new technology [1].

There are two major obstacles to replacing hydraulic actuators with EMAs: heat generation management and power management. Firstly, unlike hydraulic actuators, EMAs do not have the inherent advantage of recirculating fluid to cool their components [16]. Rather, windings in EMAs can overheat rapidly depending on the demands, at which point materials can degrade. Neodymium-iron-boron is one of the most powerful permanent magnets for electric motors, but it begins to demagnetize at relatively low temperatures [17], with an operating range upper limit of 120 °C to 180 °C. Although effective, liquid cooling reinstitutes one of the systems that are being eliminated. Primary flight control actuators are of particular relevance because they are continually engaged during flight, are required to accelerate rapidly, and are often faced with high wind loads. As the complexities of aircraft systems exponentially grow and the demand for lightweight composites increases, thermal concerns are increasingly significant. Heat generation in motor windings can be highly dynamic and localized. Predicting how much heat would be generated by an EMA is critical.

Secondly, EMAs have the advantage of only using power when active, whereas hydraulic systems require that a pump continuously maintain line pressure. This difference should help to make EMA systems more efficient than hydraulic systems. However, this advantage brings with it a major complication: the power draw from the electrical supply is also highly dynamic. Compounding this problem are the highly variable demands of all the electrical systems of an entire aircraft drawing power from one source. Predicting how much power will be drawn during operation is critical for sizing system components and choosing the power supply type (e.g. battery-supercapacitor hybrid).

Given the need for predicting dynamically generated heat and power demand, an accurate simulation model is tremendously valuable in designing an EMA system. EMA systems are complex and testing them is an involved procedure. Such systems are also expensive which discourages testing them to their limits, and many different scenarios are needed to properly test an EMA. Furthermore, there are significant details which cannot be practically measured experimentally. Therefore, it is advantageous to simulate the entire EMA with all its dynamics having only measured its key parameters.

The EMA simulation model presented in this chapter meets this goal. It includes a position field-oriented control (FOC), a pulse-width modulation (PWM) component, an electro-mechanical dynamics component, and a thermal component. Model parameters are obtained by experimentation or finite element method (FEM). The full simulation model is a nonlinear, lumped-element model (NL-LEM). The model corresponds to a linear actuator with a permanent magnet (PM) rotational motor connected to a rotational-to-linear drive train (e.g. a ball screw or a roller screw).

The methodology presented here provides a means of predicting heat generation and the overall power demands of an EMA. Such tools will help in reaching the goal of an all-electric aircraft.

Simulation results, including heat generation and power demand, for a commercially available, test EMA are shown in the latter part of the chapter.

Model Layout

The four main components of the NL-LEM are shown in Figure 5.

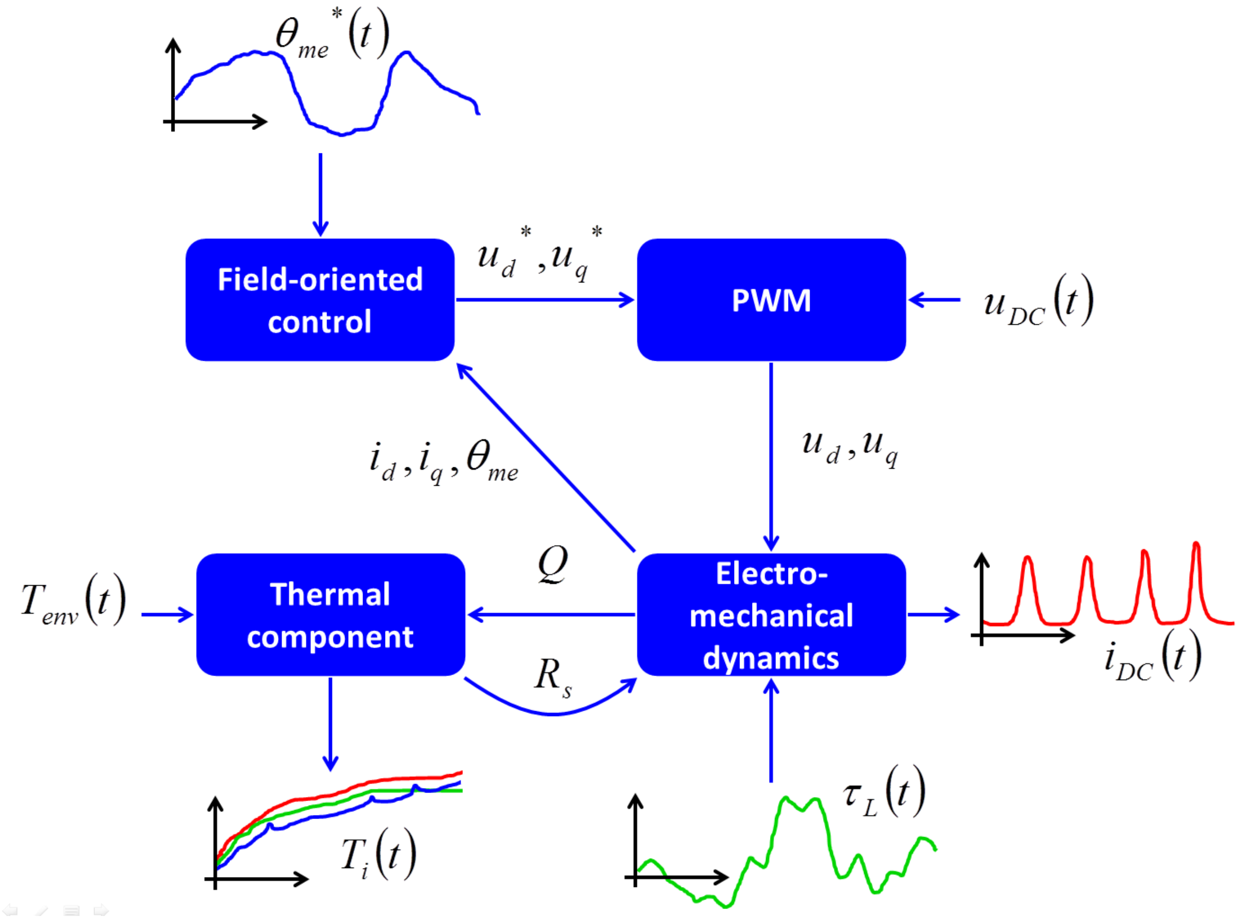

Figure 5. Model layout showing the connection of the four major components: field-oriented control, pulse-width modulation, electromechanical dynamics, and the thermal component.

The model takes the EMA rod's desired motion profile translated to an electrical reference frame of the motor's rotor, $\theta_{me}{}^{*}$ (the rotor's angle θ_m multiplied by the number of pole pairs, $P/2$), as an input to the field-oriented control (FOC). Based on the present state of the direct and quadrature (DQ0) currents, i_d and i_q, and the actual position of the EMA rod, θ_{me}, the FOC algorithm calculates the reference voltages, $u_d{}^{*}$ and $u_q{}^{*}$, in such a way that the torque angle, ϕ, (the angle formed by the i_d and i_q current vectors) is kept at ±π/2. (The power-variant DQ0 transform is used for this work.) The PWM component takes these reference voltages as well as the present state of the DC supply voltage, u_{DC}, and calculates the PWM voltages, u_d and u_q. These are the actual input voltages to the electromechanical dynamics. With these and the present load torque, τ_L, the electromechanical dynamical equations lead to the calculation of the currents, i_d and i_q, EMA position, θ_{me}, and dynamically generated heat, Q. An output of the electromechanical component is the DC current of the EMA system, i_{DC}. Together with the DC bus voltage, u_{DC}, it represents the power demands of the EMA system at its terminals. The heat generated in the motor is the input to the thermal component. With the present value of the environmental temperature, T_{env}, the thermal equations lead to the nodal temperatures, T_i, and the updated value of resistance, R_s, which is fed back into the electromechanical dynamics. The nodal temperatures represent the thermal behavior of the EMA system. Table 1 summarizes many of these terms.

Table 1. Simulation States

Symbol	Name	Units
t	Time	s
ϕ	Torque angle	rad
θ_m	Rotor angle	rad
θ_m^*	Desired rotor angle	rad
θ_{me}	Rotor angle θ_m scaled by $P/2$	rad
θ_{me}^*	Desired rotor angle θ_m^* scaled by $P/2$	rad
ω_{me}	First time-derivative of θ_{me}	rad/s
ω_{me}^*	First time-derivative of θ_{me}^*	rad/s
α_{me}	Second time-derivative of θ_{me}	rad/s^2
τ_L	Load torque	N m
τ_M	Motor-generated torque	N m
τ_g	Torque due to gravity	N m
τ_f	Frictional torque	N m
u_d	Direct voltage	V
u_q	Quadrature voltage	V
i_d	Direct current	A
i_q	Quadrature current	A
u_d^*	Desired direct voltage	V
u_q^*	Desired quadrature voltage	V
i_d^*	Desired direct current	A
i_q^*	Desired quadrature current	A
u_{DC}	DC bus voltage	V
i_{DC}	DC bus current	A
Q	Generated heat	W
R_s	Phase resistance	Ω
T_{env}	Environmental temperature	°C
T_i	Nodal temperature	°C

All the torques are in the mechanical, angular reference frame (i.e. they have not been scaled by $P/2$).

Notice that the desired position, θ_{me}^*, the load torque, τ_L, the environmental temperature, T_{env}, and the DC voltage, u_{DC}, all can be variable inputs to the model. An EMA can be run through a motion profile in the presence of a variable load profile while the bus voltage and environmental temperature change.

Parameter Measurement and FEM Calculation

Table 2 shows a summary of the key EMA parameters. Some of the parameters, such as the number of slots and number of poles, are easily obtained from the actuator's documentation, but others must be measured or carefully calculated. Some of the measurements are performed while the actuator is coupled with a hydraulic press or some other active load.

Table 2. EMA Parameters

Symbol	Name	Units
N_{cr}	Gearing ratio	rad/m
S	Number of slots	ND
P	Number of poles	ND
$\tau_{f,max}$	Maximum power train friction torque	N m
m	Rod mass	kg
I	Rotor moment of inertia	kg m^2/rad^2
$R_{s,ref}$	Phase resistance at T_{ref}	Ω
T_{ref}	Reference temperature	°C
α_R	Temperature coefficient of resistance	°C^{-1}
λ_{PM}	PM flux linkage	Wb
$L_d(i_d,i_q)$	Direct inductance	H
$L_q(i_d,i_q)$	Quadrature inductance	H

Measurement

Gearing ratio, N_{cr}

The gearing ratio is carefully calculated by counting the teeth on each gear and measuring the linear displacement of the actuator rod for one full revolution of the rotor.

Power train friction, τ_f

The hydraulic actuator is coupled to the unpowered EMA and drives the EMA's rod up and down. The static friction of the EMA's drive train is obtained by using the force and stroke data collected during this test, and the mean forces required to push or pull the EMA rod are calculated. The magnitudes of these forces are unequal due to a bias. This bias exists because of the weight of the rod itself, and the difference between this bias and the push and pull forces is the friction force. This force is then converted to a torque as seen by the motor's rotor.

Rod mass, m

The mass of the EMA's entire rod is derived from the friction test. The bias in the force required to move the EMA rod is due to the weight of the rod. This translates to a certain mass.

Rotor moment of inertia, I

The rotor moment of inertia is obtained by measuring the dimensions of the rotor and the material densities and calculating the moment of inertia.

Phase resistance, R_s

The phase resistance is measured by connecting leads to two of the three phase lines into the motor and measuring the open-circuit line-to-line resistance. This value is then divided by two if the motor is a wye-connected motor.

FEM Calculation

The material composition and geometry of the motor are used in designing an FEM model in ANSYS's Maxwell 2D. Values of rotor angle, torque angle, and current amplitude are varied as multiple simulation runs are performed.

Many of the motor modeling researchers in the past [18], [19] and even present [20], [21] use constant parameter values in simulations, although some use nonlinear inductances [22],

[23], [24]. For this chapter, FEM is used to obtain L_d and L_q as nonlinear functions of i_d and i_q. The derivatives of inductance with respect to current are numerically calculated from these tables. The inductances and their derivatives with respect to DQ0 currents can be stored in tables which are then indexed during simulation.

The FEM model is simulated with currents well above the motor's normal operating range in order to capture the behavior during highly transient moments. The torque angle should be varied from 0 to π radians to capture the full character of the inductances. Even if the rotor of an EMA is round, the rotor angle has an effect on the DQ0 reference frame inductances. Therefore, the rotor angle should also be varied over one period of variation in the DQ0 inductances. Such variation occurs mostly at relatively high current values (i.e. at saturation), so this variation is averaged out, but the calculation of inductance at a single rotor angle cannot be assumed to be representative of the average.

Note that the peak inductance values do not necessarily occur at zero current, nor are the inductances mirrored about the quadrature axis. An example of this is in Figure 6. This should clarify the highly variable nature of inductances and the need to use nonlinear modeling instead of assuming constant values.

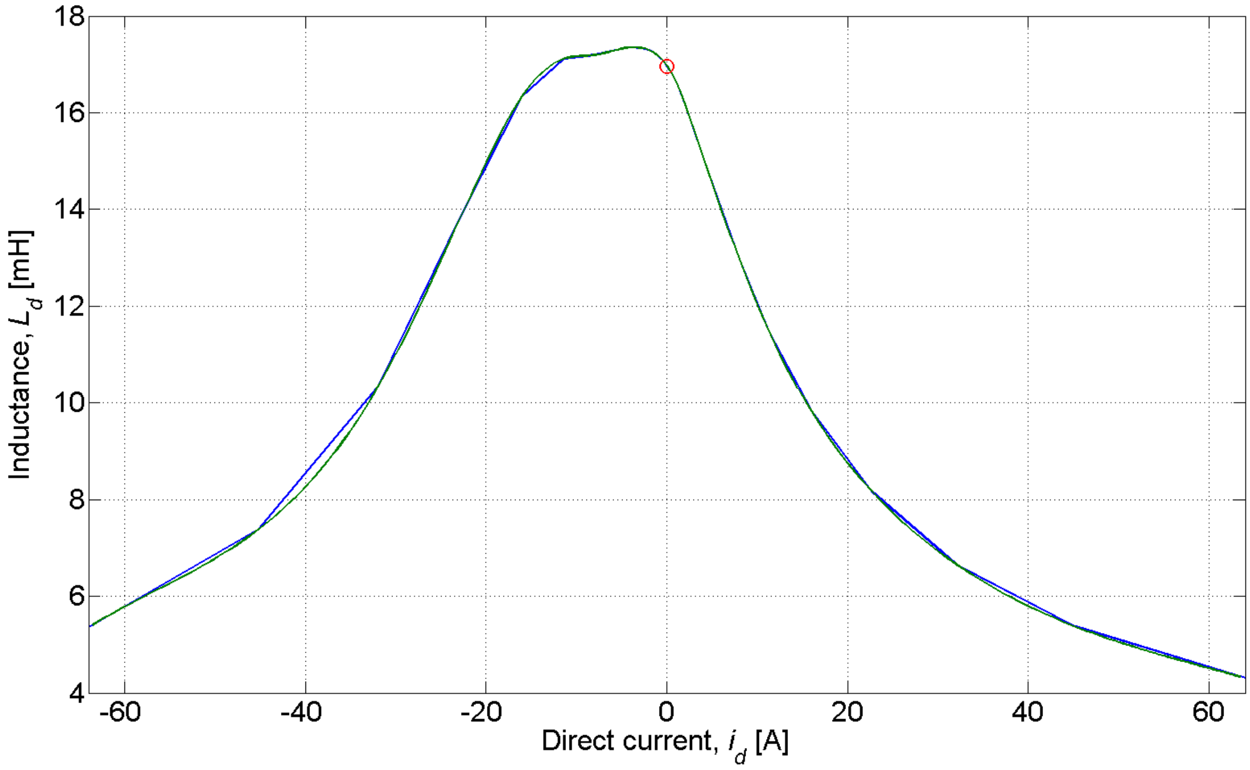

Figure 6. Direct-axis inductance along the i_d axis (blue) and the inductance value at zero current (green circle). The inductance is not mirrored about the quadrature axis (This axis goes into the page), so its values for positive i_d do not match those for negative i_d.

Electromechanical Dynamics

The motor dynamics are modeled by four primary dynamical equations in the DQ0 reference frame [25]. The first two of these equations are

$$\frac{di_d}{dt} = \frac{L_{qq}G_d - L_{dq}G_q}{L_{dd}L_{qq} - L_{dq}L_{qd}} \tag{1}$$

$$\frac{di_q}{dt} = \frac{L_{dd}G_q - L_{qd}G_d}{L_{dd}L_{qq} - L_{dq}L_{qd}}. \tag{2}$$

These come from the voltage equations (3) and (4):

$$u_d = R_s i_d + L_{dd}\frac{di_d}{dt} + L_{dq}\frac{di_q}{dt} - L_q i_q \omega_{me} \tag{3}$$

$$u_q = R_s i_q + L_{qd}\frac{di_d}{dt} + L_{qq}\frac{di_q}{dt} + \left(L_d i_d + \lambda_{PM}\right)\omega_{me}\,, \tag{4}$$

where

$$L_{dd} = L_d + i_d\frac{dL_d}{di_d} \tag{5}$$

$$L_{dq} = i_d\frac{dL_d}{di_q} \tag{6}$$

$$L_{qd} = i_q\frac{dL_q}{di_d} \tag{7}$$

$$L_{qq} = L_q + i_q\frac{dL_q}{di_q} \tag{8}$$

$$G_d = u_d - R_s i_d + \left(L_q i_q\right)\omega_{me} \tag{9}$$

$$G_q = u_q - R_s i_q - \left(L_d i_d + \lambda_{PM}\right)\omega_{me}\,. \tag{10}$$

The full derivation can be found in Appendix A: Permanent Magnet Machine Dynamics.

These equations carry the assumption that the variations in inductances over rotor angle can be reasonably averaged out, that the flux linkage from the permanent magnets appears only in the direct axis, and that the motor is balanced.

The voltages are provided by the PWM component; the current rates are calculated using (1) and (2); and the currents are found by integration.

In [26], there is a detailed analysis of the motor-generated torque equation. Given the assumptions made for (1)-(10), the motor-generated torque equation is

$$\tau_M = \frac{3P}{4} i_q\left[\lambda_{PM} + \left(L_d - L_q\right)i_d\right]. \tag{11}$$

The third dynamical equation is the torque-acceleration equation that links the motor-generated torque to the acceleration it produces:

$$\frac{d\omega_{me}}{dt} = \alpha_{me} = \frac{P}{2}\frac{1}{I_{net}}\left(\tau_M + \tau_L + \tau_g + \tau_f\right), \tag{12}$$

where I_{net} is the combined effect of all inertias from all moving parts in the EMA translated to the mechanical, angular reference frame of the rotor. The value I_{net} is calculated from the mass of the rod, *m*, and the angular moment of inertia of the rotor, *I*, by

$$I_{net} = \frac{m}{N_{cr}{}^2} + I\ . \tag{13}$$

As long as velocity is zero, the frictional torque is defined to be equal and opposite to the sum of the other component torques up to a maximum friction value. This keeps the net torque and, therefore, velocity at zero. However, when the sum of the other component torques exceeds this maximum friction, the magnitude of the friction holds at this maximum value and its sign always opposes the direction of motion (14).

$$\tau_f = \begin{cases} -\left(\tau_M + \tau_L + \tau_g\right) & : \omega_{me} = 0 \cap \left|\tau_M + \tau_L + \tau_g\right| \le \tau_{f,\max} \\ -\operatorname{sgn}\left(\omega_{me}\right)\cdot \tau_{f,\max} & : \omega_{me} \ne 0 \cup \left|\tau_M + \tau_L + \tau_g\right| > \tau_{f,\max} \end{cases} \tag{14}$$

Note that air friction is not included because EMAs use position controlled motors, which do not reach excessive speeds where air friction is a practical consideration.

Finally, the forth dynamical equation is

$$\frac{d\theta_{me}}{dt} = \omega_{me}\ . \tag{15}$$

This is simply the definition of angular velocity and is integrated to get angular position.

Thermal Component

The motor losses are related to the motor parameters. Since losses affect temperature which affects motor parameters which in turn affect losses, the losses should be modeled through the motor parameters, and not in post-processing. Copper winding loss is a primary power loss. The winding loss can be calculated as

$$Q = \left(i_a{}^2 + i_b{}^2 + i_c{}^2\right) R_s \,, \tag{16}$$

or equivalently

$$Q = \frac{3}{2}\left(i_d{}^2 + i_q{}^2\right) R_s \tag{17}$$

in the DQ0 reference frame. This heat is then fed into the lumped-element thermal model.

Some thermal models, such as in [27], use only one temperature node. The model shown here uses multiple nodes. The temperatures at multiple locations in the motor are calculated using a lumped-element thermal model (Figure 7) of the form shown in (18):

$$\frac{dT_i}{dt} = \left(Q_i + \sum_k^K T_k \rho_{ik}\right)\sigma_i \,, \tag{18}$$

where T_i and T_k are nodal temperatures, Q_i is a heat source corresponding to that node, K is the number of nodes in the network, ρ_{ik} is a sum of reciprocals of thermal resistances linking the node to nearby nodes, and σ_i is a reciprocal of thermal capacitance linking the node to the thermal sink. This model is similar to the one developed in [28] for another PM motor.

The source of heat for the temperature calculations is the copper power loss in the windings. The temperature distribution of the motor is modeled using a lumped-element network shown in Figure 7. The values of the thermal resistances and capacitances are developed using an FEM model of the motor.

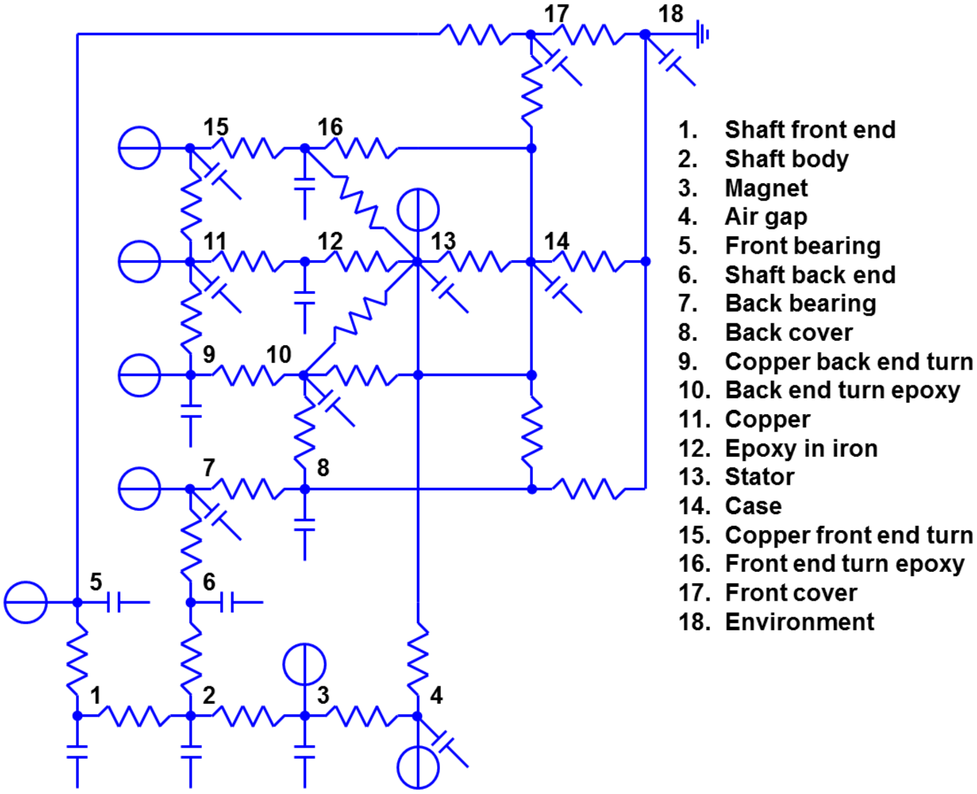

Figure 7. Thermal lumped element model. The motor is defined to have a front and a back. The space between the rotor and stator is the air gap. The rotor is composed of magnets on a shaft. The body of the shaft is the central region about which the magnets are fixed. The bearings hold the shaft in place at both of its ends. The front and back of the motor have an aluminum cover and the sides of the motor are surrounded by an aluminum case. The copper windings loop around the stator teeth concentrically and are completely embedded in epoxy. The epoxy in iron is the epoxy surrounding the windings and located in the main body of the iron stator. The end turns are the points on either end where the windings loop around the stator teeth passing from one stator slot to another. And, the environment is the surrounding atmosphere.

This model is generic with multiple heat sources. Here, however, the copper loss is considered to be the predominant heat source in the motor.

Given updated nodal temperatures, the electrical phase resistance can be updated. The relationship between copper resistance and temperature [29] is as follows:

$$R_s = R_{s,ref}\,[1 + \alpha_R\,(T - T_{ref})], \tag{19}$$

where $R_{s,ref}$ is the resistance of the copper winding at the reference temperature T_{ref}, and α_R is the temperature coefficient of resistance for the copper.

Field-oriented Control

A thorough analysis of dynamic motor heat generation should include motor drive dynamics. This model’s field-oriented control (FOC) translates the desired motion profile into simulation drive voltages. The control is an adaptive closed-loop control, which is a type of feedback linearization of the speed and position errors.

In the following derivation, the star superscript is used to indicate desired values. Starting with angular velocity and angular position errors, a desired angular acceleration, $\alpha_{me}{}^*$, is developed:

$$\alpha_{me}{}^* = k_\omega \frac{\left(\omega_{me}{}^* - \omega_{me}\right)}{\Delta t_c} + k_\theta \frac{\left(\theta_{me}{}^* - \theta_{me}\right)}{\Delta t_c}, \tag{20}$$

where Δt_c is the time step of the control loop and k_ω and k_θ are control coefficients. This equation tends toward changing the present angular velocity and position to match the desired angular velocity and position.

The desired velocity must be redefined based on this newly calculated desired acceleration:

$$\omega_{me}{}^* = \omega_{me} + \alpha_{me}{}^* \Delta t_c\,. \tag{21}$$

If the load torque is predicted by estimating the load torque from the previous step and if the frictional and gravitational torques are neglected, then (12) becomes (22).

$$\begin{aligned}\tau_M{}^* = \;& \alpha_{me}{}^* I_{net}\frac{2}{P} - \overbrace{\tau_g - \tau_f}^{0} - \\ & \underbrace{\left[\alpha_{me} I_{net}\frac{2}{P} - \left(\frac{3P}{4}\lambda_{PM} i_q\right) - \overbrace{\tau_g - \tau_f}^{0}\right]}_{\tilde{\tau}_L},\end{aligned} \tag{22}$$

Using (11) as a control equation and setting $i_d{}^*$ to zero yields

$$\tau_M{}^* = i_q{}^*\frac{3P}{4}\lambda_{PM}\;. \tag{23}$$

Substituting (23) into (22) and solving for $i_q{}^*$ results in (24).

$$i_q{}^* = \frac{8\left(\alpha_{me}{}^* - \alpha_{me}\right) I_{net}}{3P^2\lambda_{PM}} + i_q \tag{24}$$

The desired currents and current rates are then limited.

Lastly, the desired voltages are calculated:

$$u_d{}^* = R_s i_d{}^* + L_{d0}\frac{di_d{}^*}{dt} - L_{q0} i_q{}^* \omega_{me}{}^* \tag{25}$$

$$u_q{}^* = R_s i_q{}^* + L_{q0}\frac{di_q{}^*}{dt} + \left(L_{d0} i_d{}^* + \lambda_{PM}\right)\omega_{me}{}^*, \tag{26}$$

where L_{d0} and L_{q0} are the direct and quadrature inductances at zero current, respectively. These constants are used instead of the nonlinear parameters for the sake of simplicity.

PWM Component

The PWM component of the simulation model uses a trailing edge modulation carrier, as demonstrated in Figure 8. The voltages are translated into the ABC reference frame. The PWM algorithm is performed on those voltages. Then, these pulsed voltages are translated back into the DQ0 reference frame.

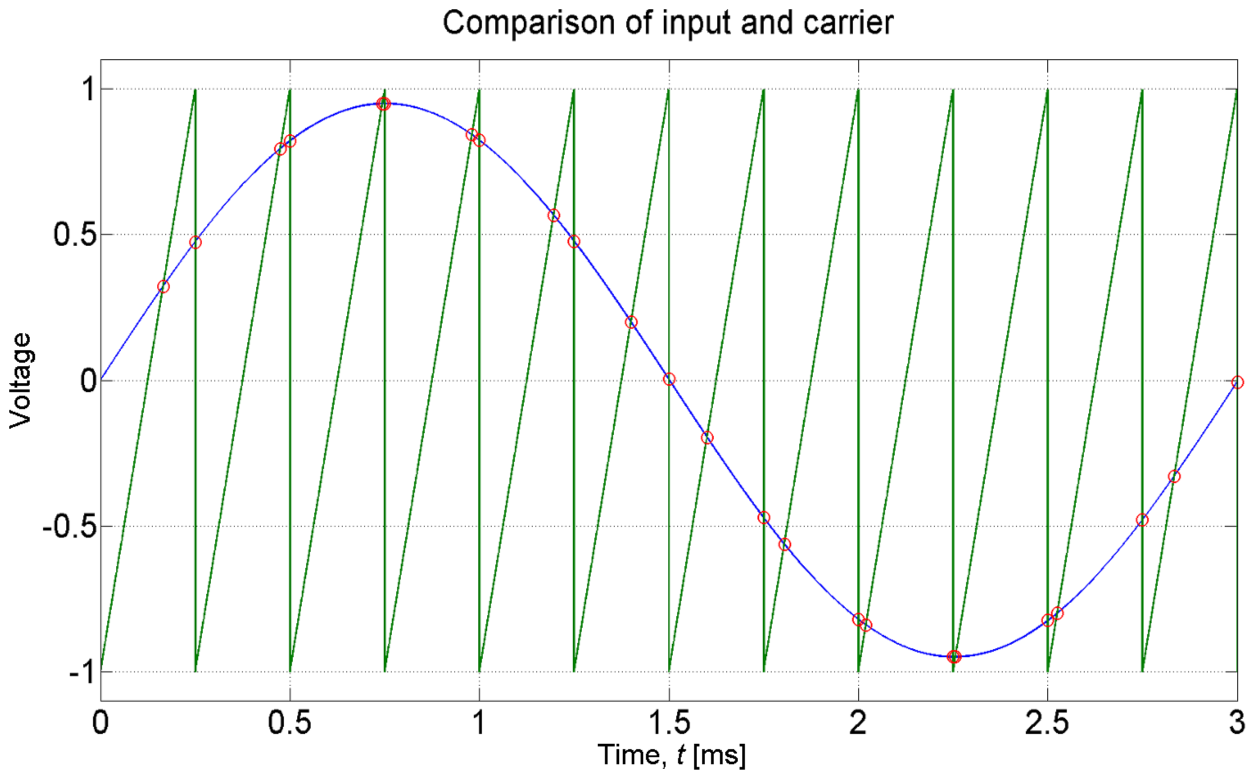
Comparison of input and carrier
Voltage
Time, t [ms]
1
0.5
0
-0.5
-1
0
0.5
1
1.5
2
2.5
3

(a)

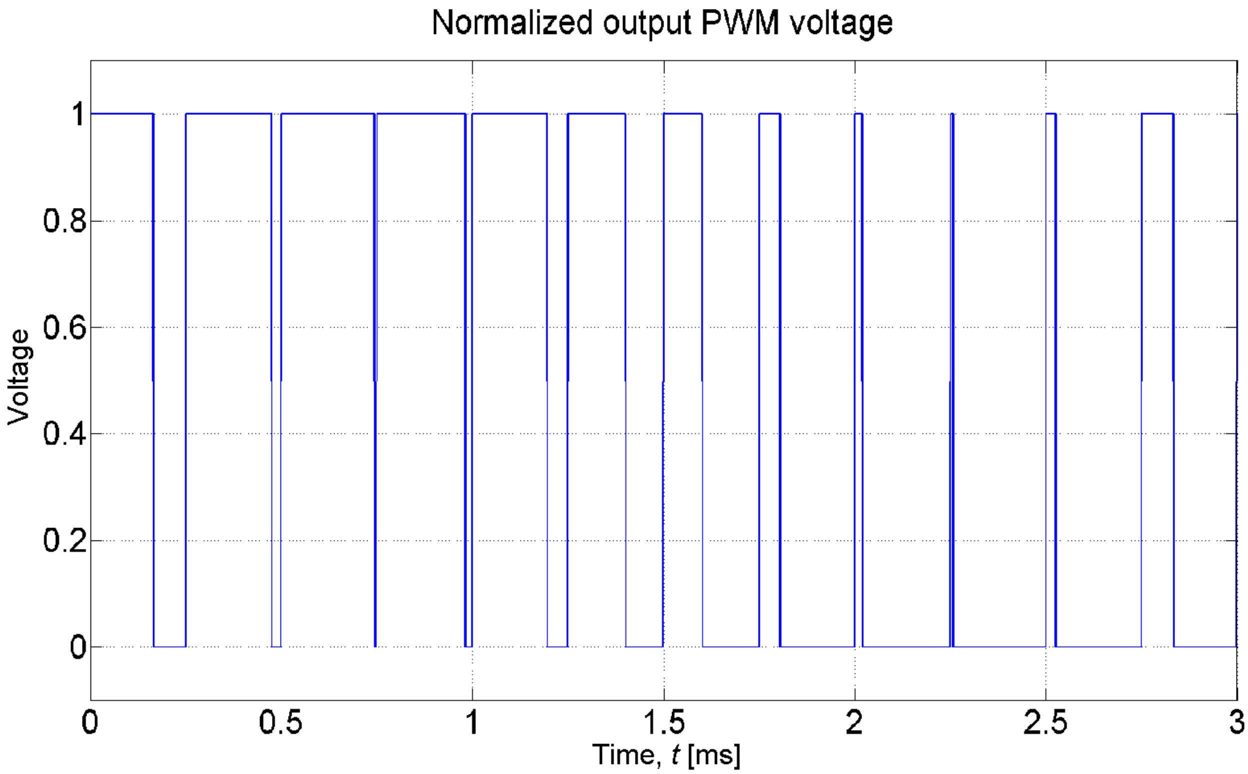

(b)

Figure 8. The general concept of the PWM. A trailing edge carrier wave (a) is compared to a normalized sinusoidal phase voltage. When the normalized wave is greater than the carrier wave, the output PWM voltage (b) is turned on. Otherwise, it is off.

Inputs

Scaling

The stroke and load force data are recorded from actual flight profiles. However, these profiles correspond to an actuator with performance characteristics that might not match those of a test actuator. Therefore, the stroke and force profiles are scaled for a range which is compatible with the test actuator. The stroke profile is also adjusted to match the acceleration limits of the actuator by stretching the profile over time. This scaling is appropriate for testing the general capability of the simulation model as is done in this chapter.

Force-stroke equation

In the absence of actual flight profiles, a force-stroke relationship can be useful in simulating the force, given a theoretical stroke profile. This force-stroke equation comes from analyzing actual flight data. The equation is

$$\begin{aligned}\hat{F} = \; & (\rho \cdot C_d + C_{d0}) \cdot \\ & \left[(x - x_0) + C_2(x - x_0)^2 + C_3(x - x_0)^3\right] s^2 + \\ & F_0 + cv + Ma \qquad , \\ C_d = & \begin{cases} C_{d1} : x < x_0 \\ C_{d2} : x \geq x_0 \end{cases}\end{aligned} \tag{27}$$

where ρ is the air density which can be derived from the altitude of the aircraft, C_{d1}, C_{d2}, C_{d0}, C_2, and C_3 are coefficients, s is the aircraft speed, F_0 is the force bias due to the weight of the aileron, c is the net friction coefficient, M is the effective mass of the aileron, x is the stroke position, x_0 is a stroke bias, v is the first derivative of x, and a is the second derivative of x. The effect of air density depends on whether the flap is down or up ($x < x_0$ or $x \geq x_0$). The effect of aircraft speed is modeled by a Taylor series function of the stroke.

The result of fitting this function to the available data is shown in Figure 9.

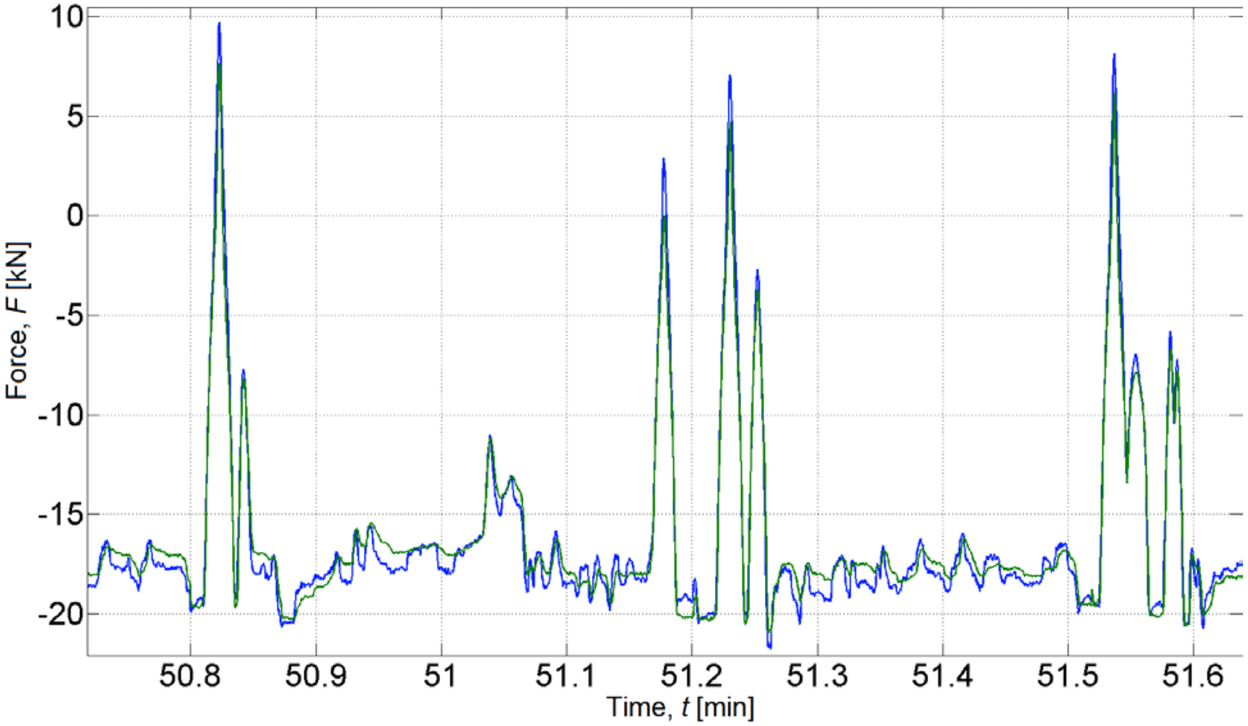

Figure 9. Actual force profile (blue) and calculated force profile (green).

The value of having this function is that it gives the freedom to run mission profiles that were never done before.

An EMA Example and Results

A commercially available EMA was measured, modeled, simulated, and experimentally tested. Following are the results.

Parameters

The key parameters for the test EMA are shown in Table 3.

Table 3. EMA Parameters

Symbol	Name	Value
N_{cr}	Gearing ratio	1963 rad/m
S	Number of slots	12
P	Number of poles	10
$\tau_{f,max}$	Maximum power train friction	0.174 N m
m	Rod mass	8.5 kg
I	Rotor moment of inertia	113.2 kg mm^2/rad^2
$R_{s,ref}$	Phase resistance at T_{ref}	1.4 Ω
T_{ref}	Reference temperature	20 °C
α_R	Temperature coefficient of resistance	0.004041 °C^{-1} [29]
λ_{PM}	PM flux linkage	0.149 Wb
$L_d(i_d,i_q)$	Direct inductance	0.01735 H
$L_q(i_d,i_q)$	Quadrature inductance	0.01727 H

Figure 10 shows the force-stroke data for the friction analysis.

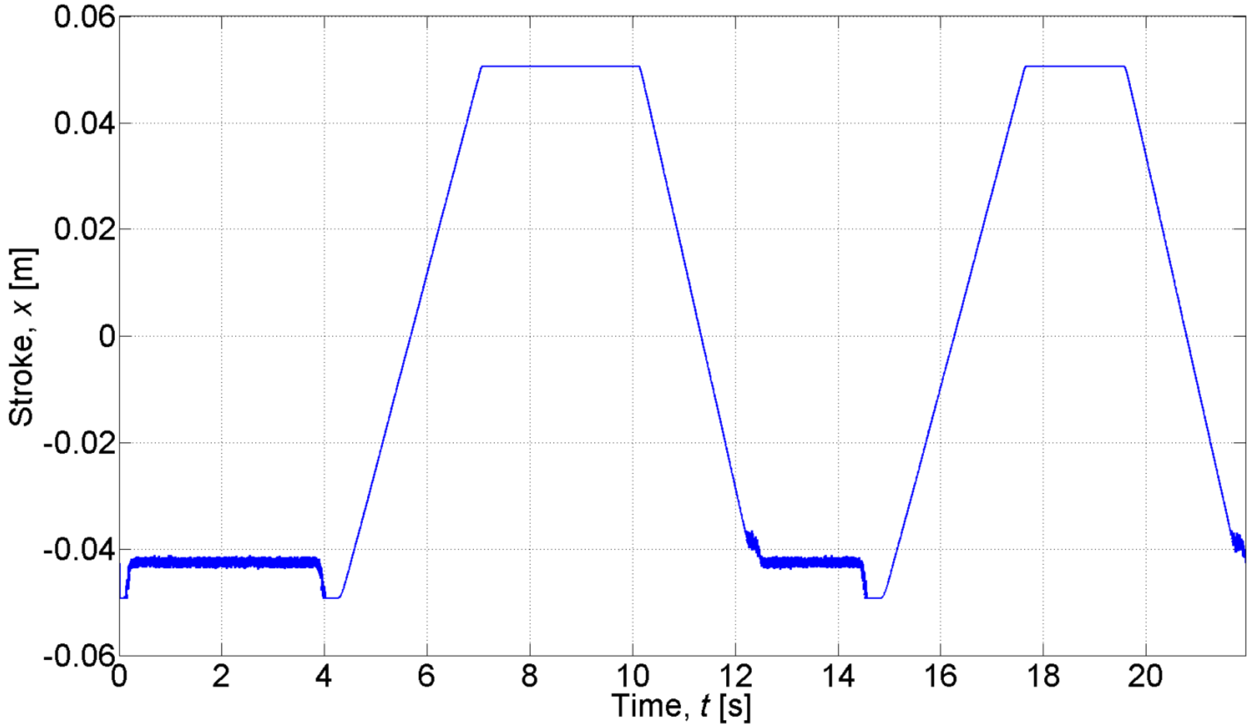

0.06
0.04
0.02
0
-0.02
-0.04
-0.06
Stroke, x [m]
0
2
4
6
8
10
12
14
16
18
20
Time, t [s]

(a)

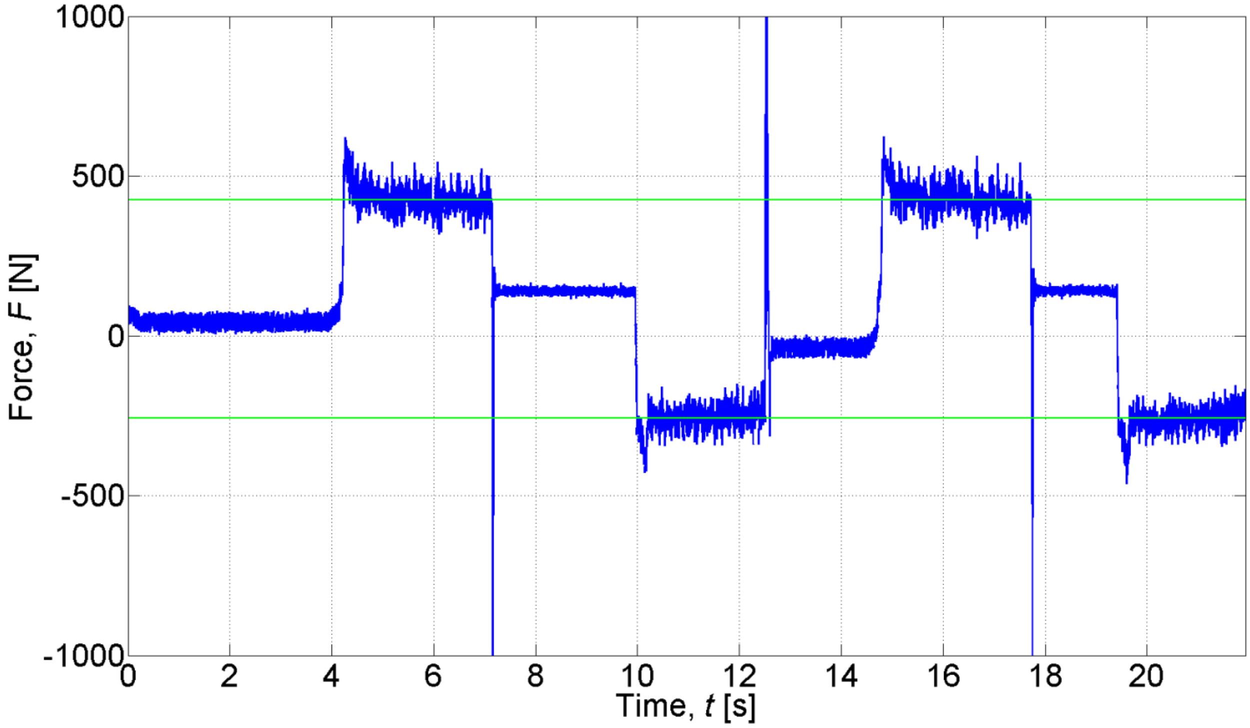

(b)

Figure 10. Static friction analysis showing (a) stroke and (b) load force. The green lines on the force plot represent the mean forces to pull (-258 N) or push (425 N) the EMA rod, overcoming the friction of the drive train (342 N). The bias force is the weight of the EMA rod (84 N).

The direct and quadrature inductances are obtained as shown in Figure 11 and Figure 12. The FEM model is simulated with a range of currents (0 to 50 A), a range of torque angles (0 to π radians), and a range of rotor angles (0 to $\pi/3$ radians). For this motor, a range of $\pi/3$ radians captures one full cycle of variation in inductance values due to rotor angle.

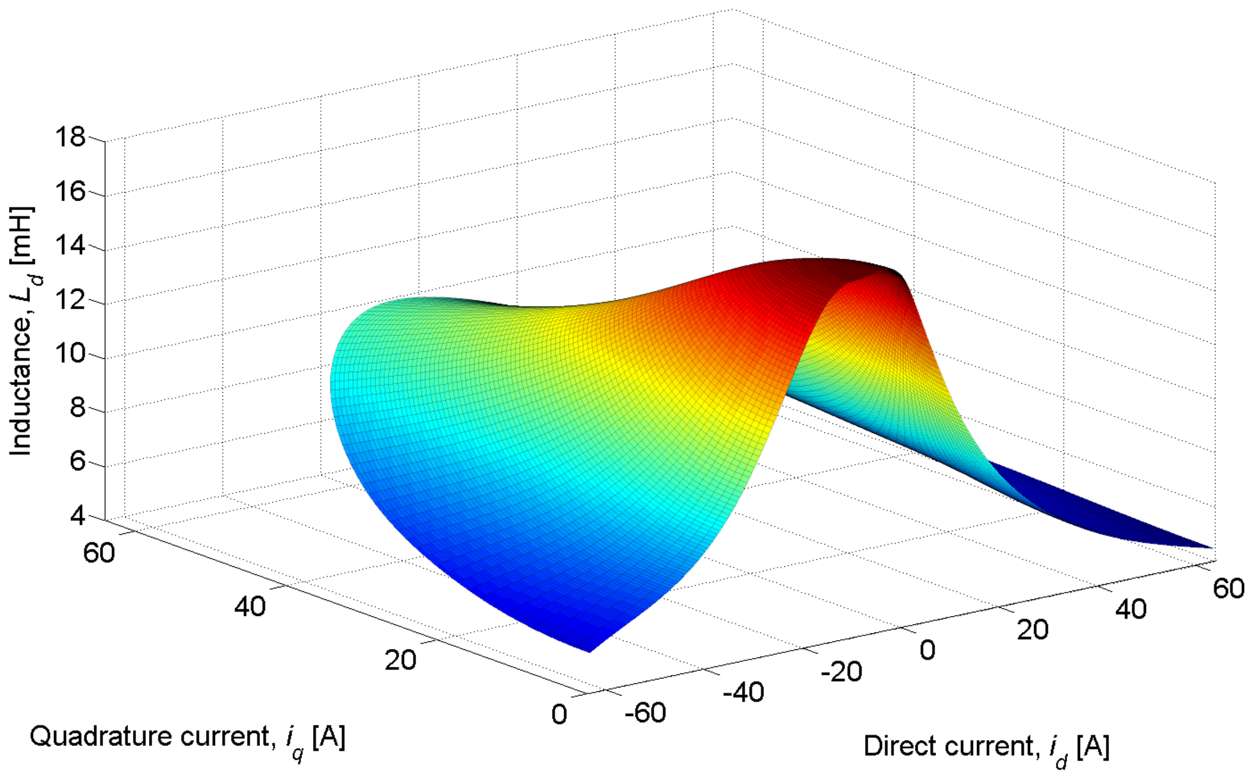

Figure 11. Direct-axis inductance as a function of direct current, i_d, and quadrature current, i_q. These inductance values are averaged over rotor angle.

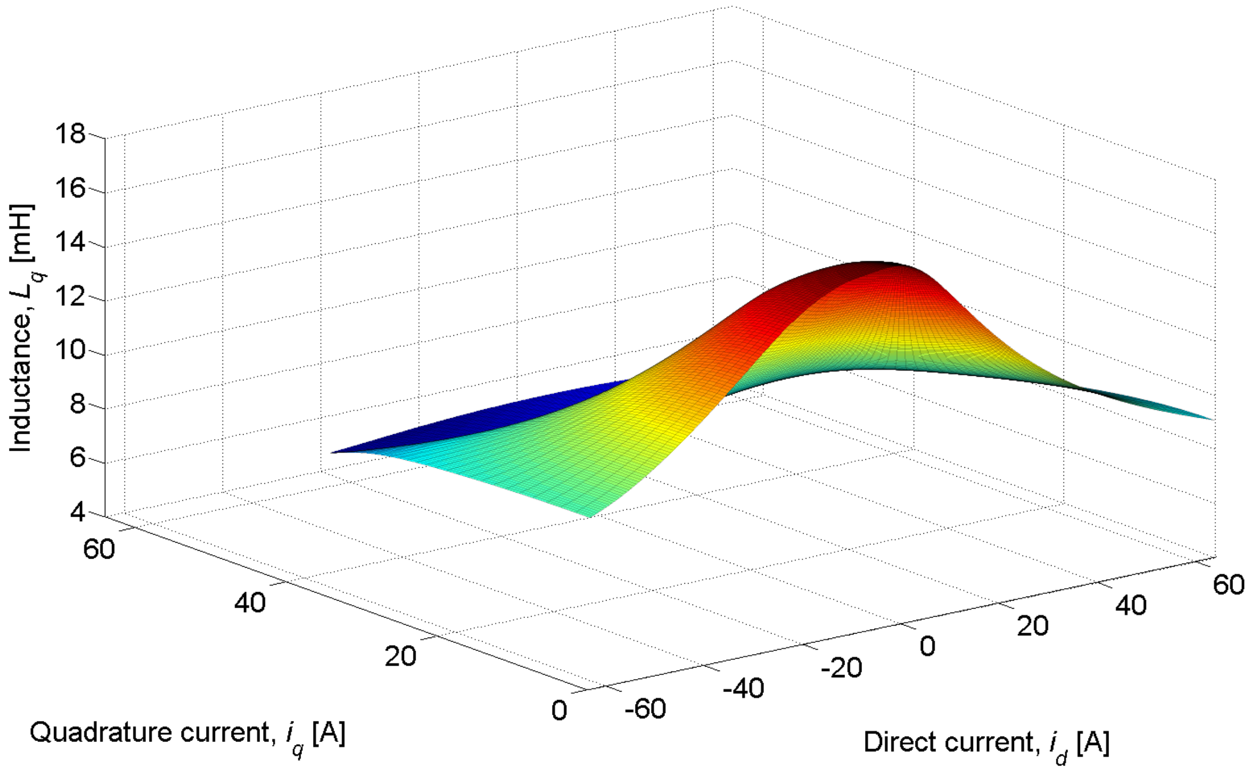

Figure 12. Quadrature-axis inductance as a function of direct current, i_d, and quadrature current, i_q. These inductance values are averaged over rotor angle.

A computer rendering of the motor geometry is shown in Figure 13. This geometry is used for FEM modeling.

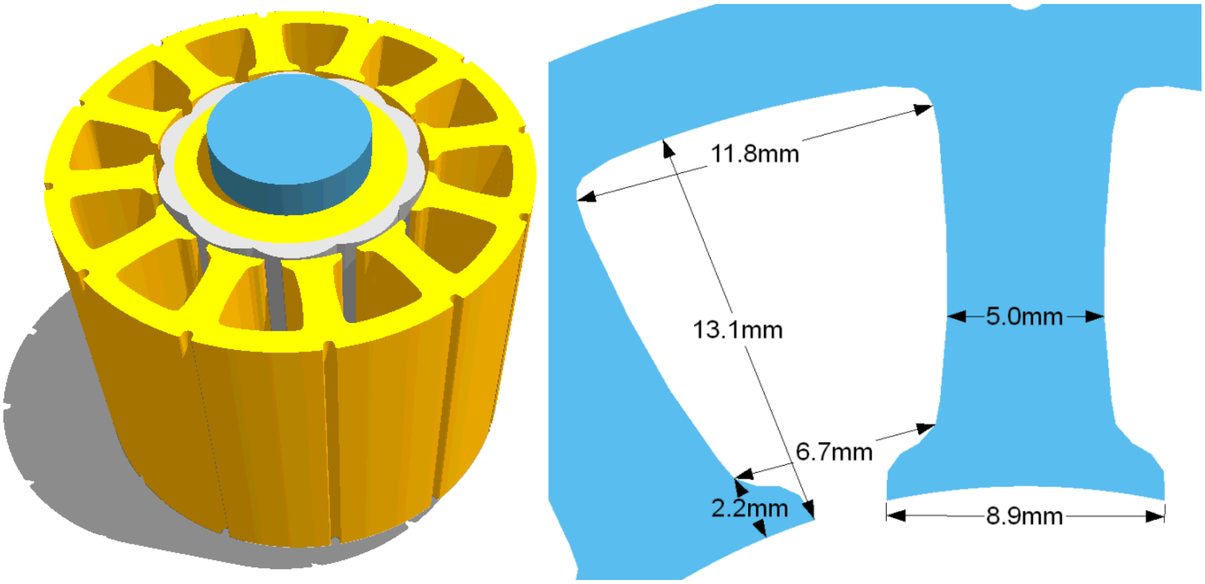

Figure 13. Motor geometry (left) and slot measurements (right).

Table 4 shows some of the material properties of the EMA motor.

Table 4. EMA Parameters

Part	Name	C_p [J/kg·K][a]	k [W/m·K][b]	ρ [kg/m3][c]
Casing	AL-384	963	96.2	2820
Lamination	Steel 1010	448	51.9	7872
Windings	Copper	385	401	8940
Epoxy	(unknown)	1050	0.85	1200
Axle	Steel	480	15	7750
Magnets	NdFeB-30	5e4	8.95	7400

[a] C_p is the specific heat capacity.

[b] k is the thermal conductivity.

[c] ρ is the density.

Table 5 shows the thermal resistances and capacitances of the thermal network for the EMA motor.

Table 5. EMA Thermal Parameters

Resistances	Value [K/W]	Capacitances	Value [J/K]
$R_{1,2}$	0.83	C_1	14.981
$R_{1,5}$	0.005	C_2	56.024
$R_{2,3}$	0.0087	C_3	6.717
$R_{2,6}$	0.5022	C_4	0
$R_{3,4}$	0.004	C_5	12.07
$R_{4,13}$	20.633	C_6	7.078
$R_{5,17}$	0.5678	C_7	7.7
$R_{6,7}$	0.004	C_8	63.675
$R_{7,8}$	4.056	C_9	2.526
$R_{8,10}$	0.09	C_{10}	8.991
$R_{8,14}$	0.124	C_{11}	38.84
$R_{8,18}$	11.1487	C_{12}	10.479
$R_{9,10}$	1.255	C_{13}	82.296
$R_{9,11}$	0.896	C_{14}	86.471
$R_{10,13}$	1.045	C_{15}	2.526
$R_{10,14}$	2.615	C_{16}	8.991
$R_{11,12}$	0.0054	C_{17}	63.675
$R_{11,15}$	0.896		
$R_{12,13}$	0.0063		
$R_{13,14}$	0.1385		
$R_{13,16}$	1.045		
$R_{14,16}$	1.015		
$R_{14,17}$	0.124		
$R_{14,18}$	1.1405		
$R_{15,16}$	0.525		
$R_{17,18}$	11.1487		

The thermal resistances are labeled according to the nodes they link. The thermal capacitances are labeled according to the nodes they are connected to.

Results

The following kinematic results are all in the linear domain. The desired stroke profile and the motor's actual stroke profile are shown in Figure 14. The motor followed the desired stroke profile very well.

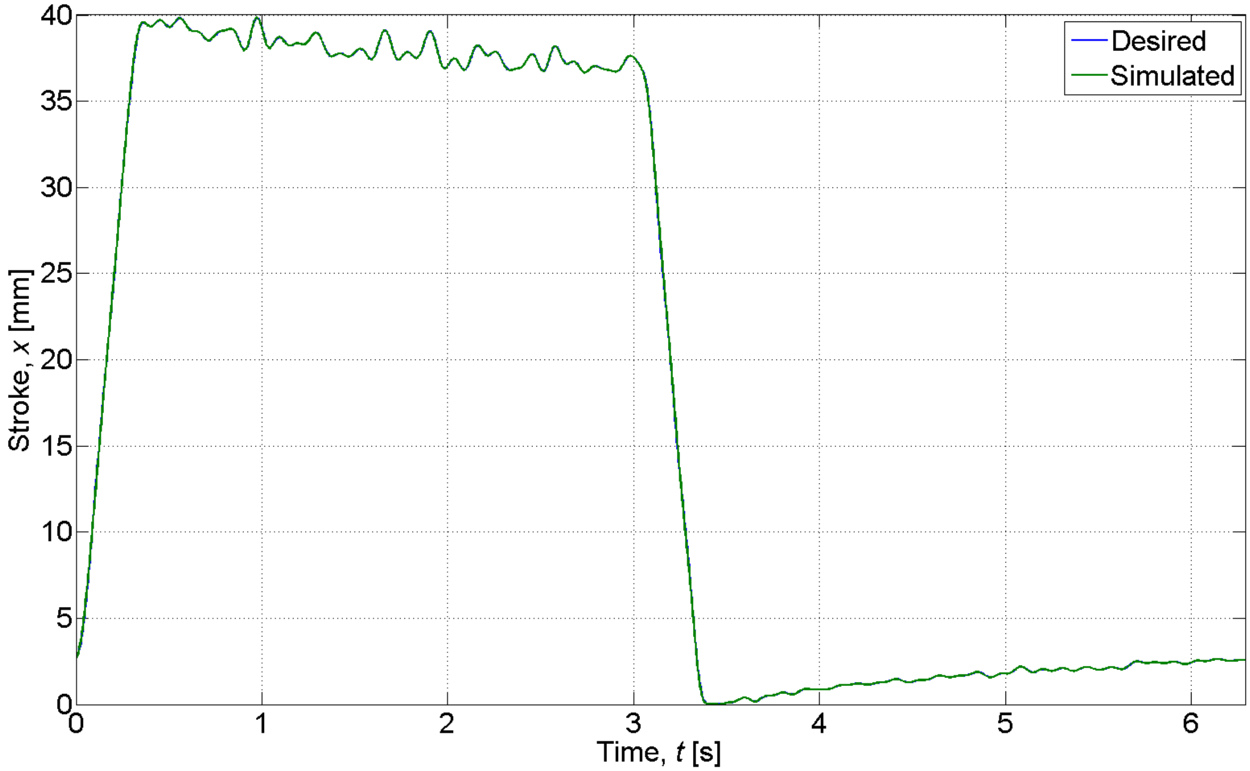

Figure 14. Desired (blue) and actual (green) stroke profiles

The load force profile and the motor-generated force are shown in Figure 15.

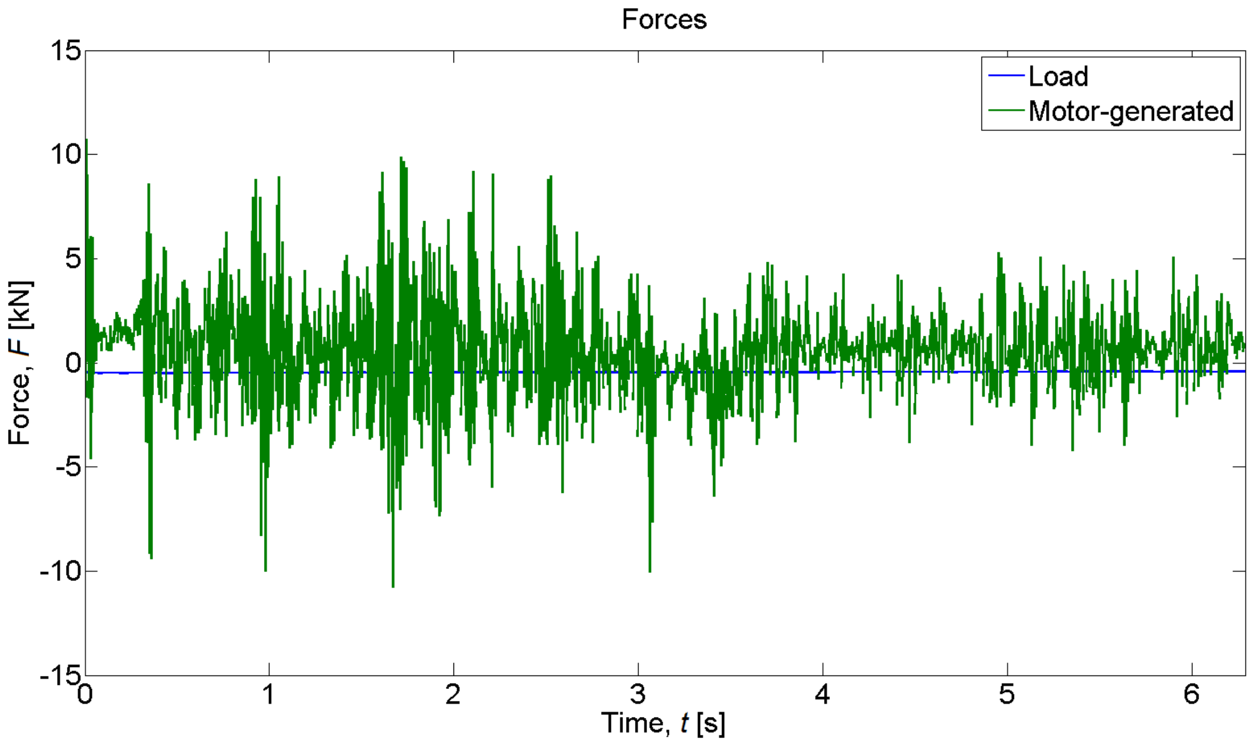

Figure 15. Input load force profile (blue) and motor-generated force (green). The load force was a sustained 0.45 kN.

The DQ0 voltages and currents are shown in Figure 16 and Figure 17, respectively.

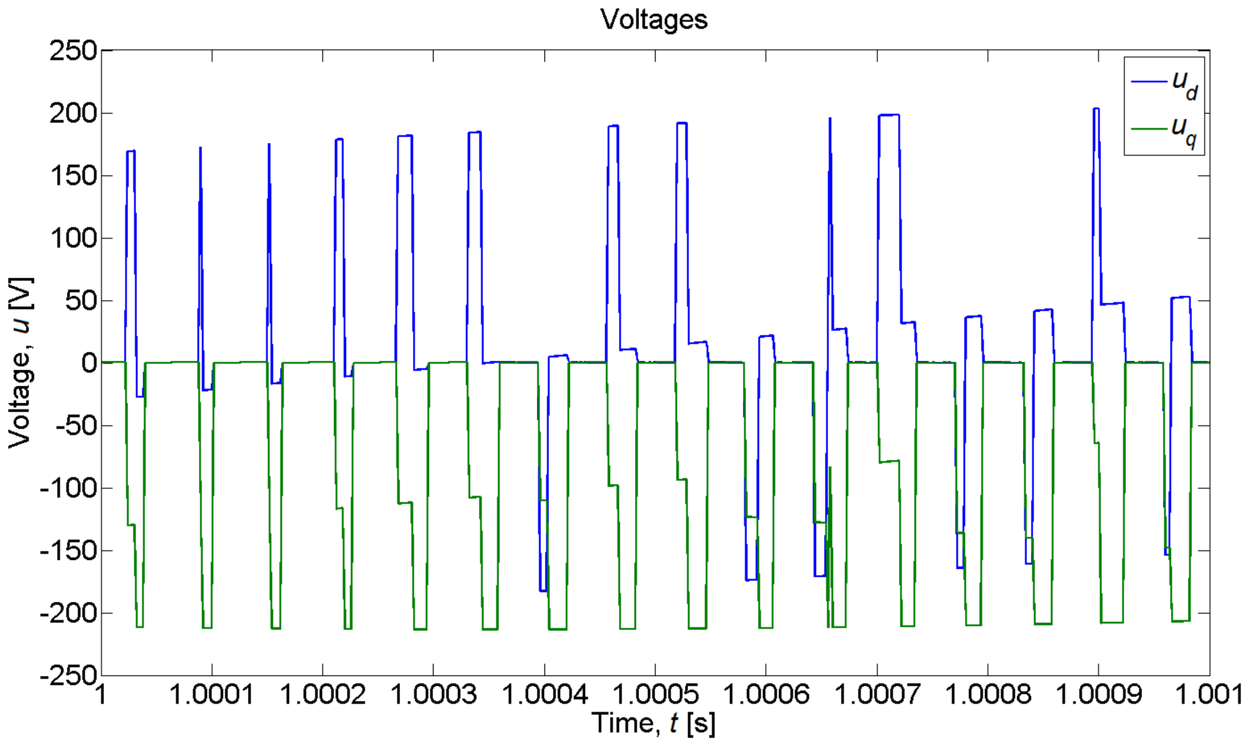

Figure 16. DQ0 voltages with pulse form due to PWM.

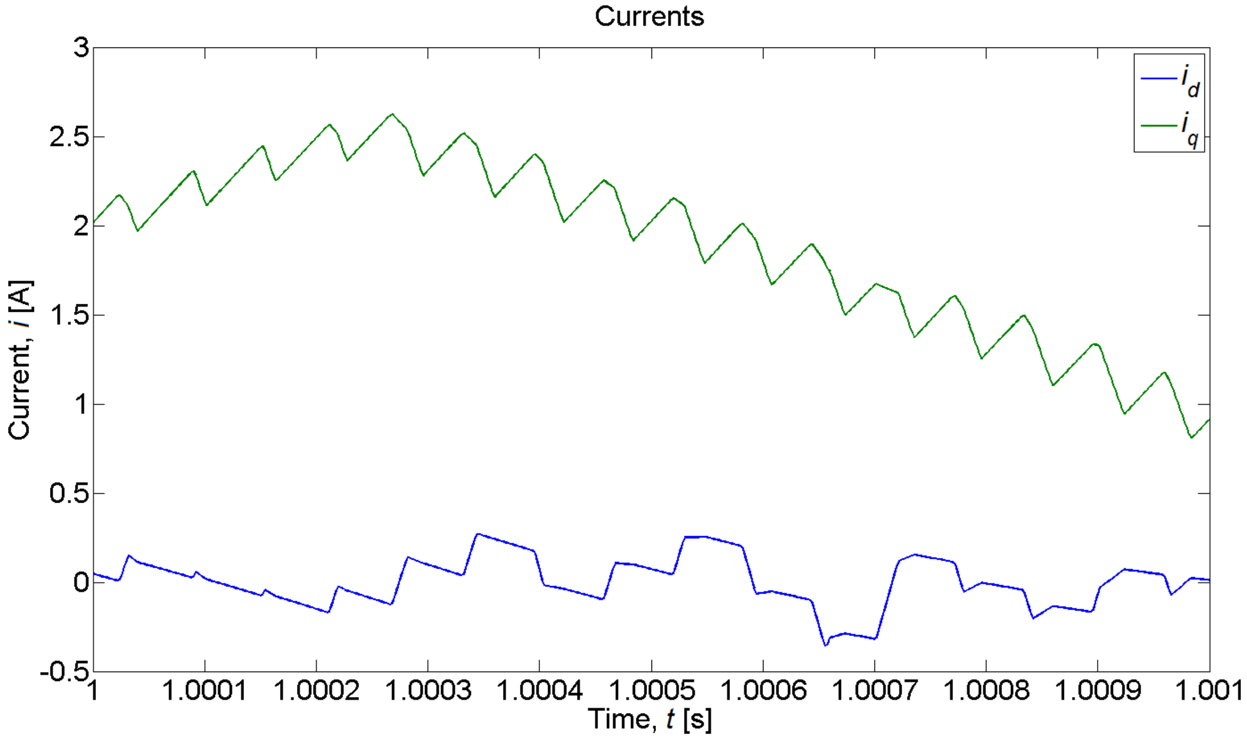

Figure 17. DQ0 currents with pulse form due to PWM.

If the motor is treated as a system, the powers into (positive) and out of (negative) this system are shown in Figure 18.

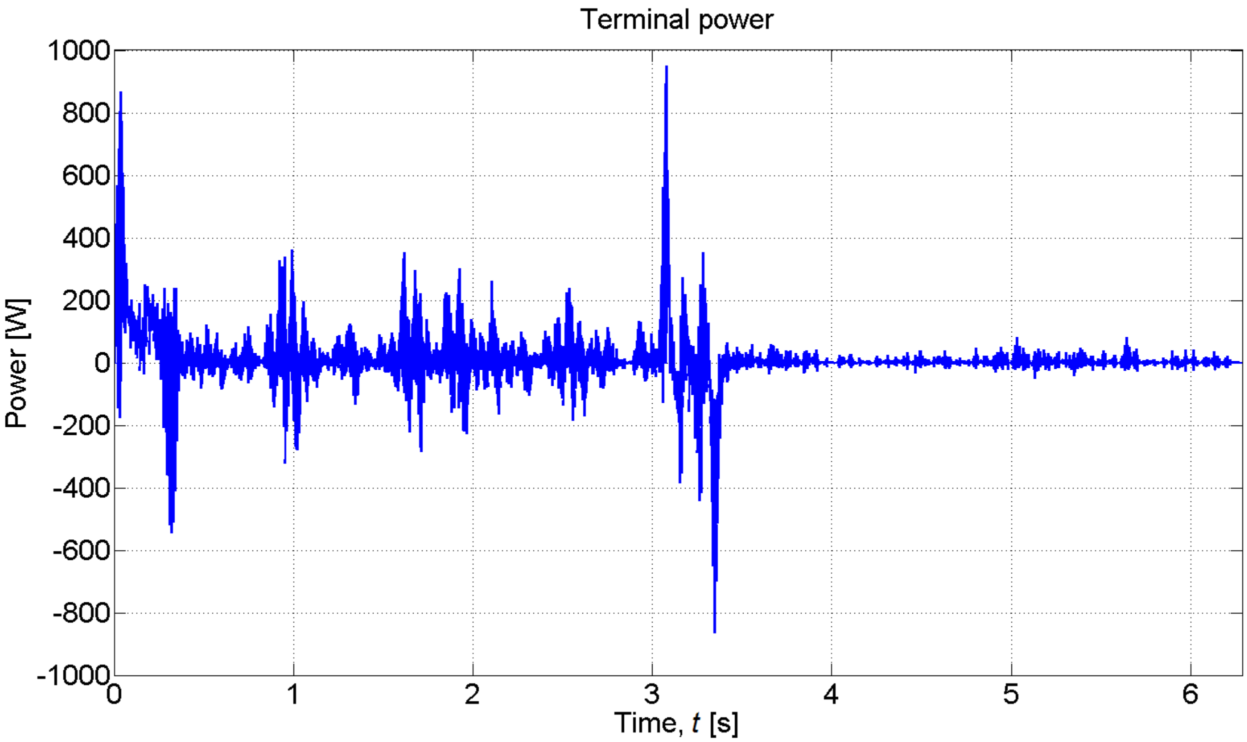
Terminal power
1000
800
600
400
200
0
-200
-400
-600
-800
-1000
Power [W]
0
1
2
3
4
5
6
Time, t [s]

(a)

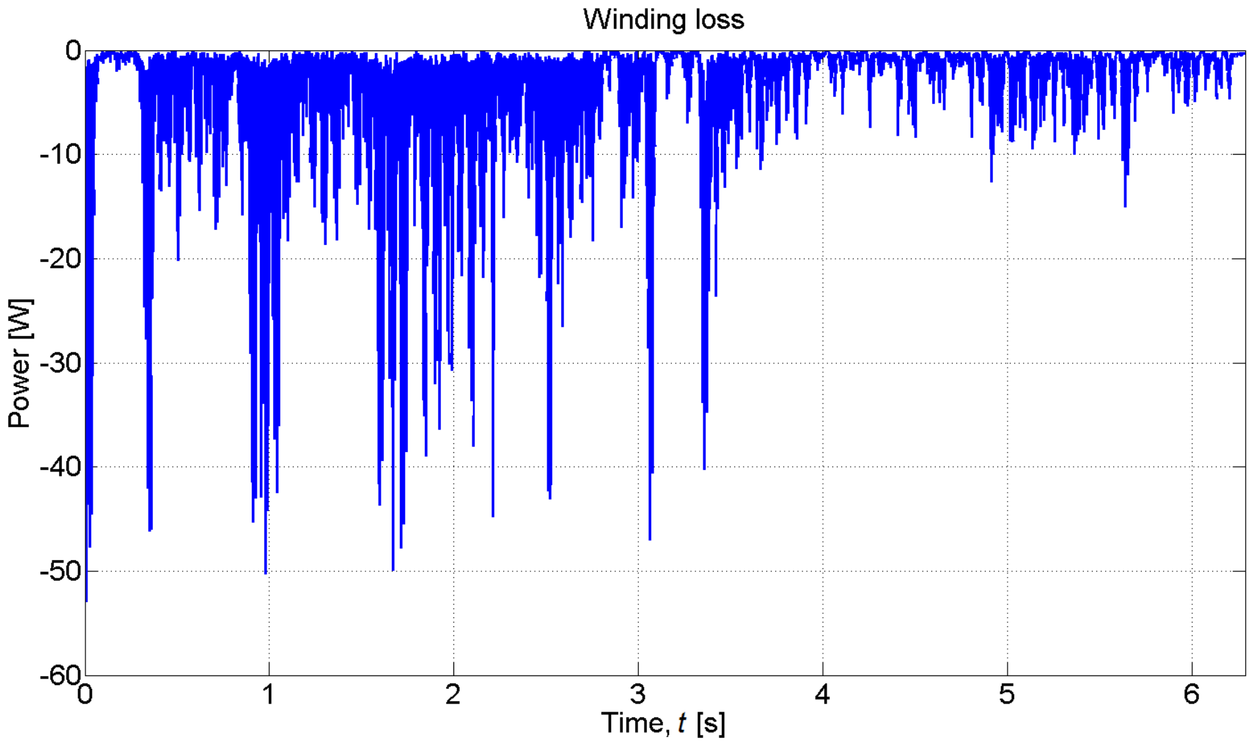

(b)

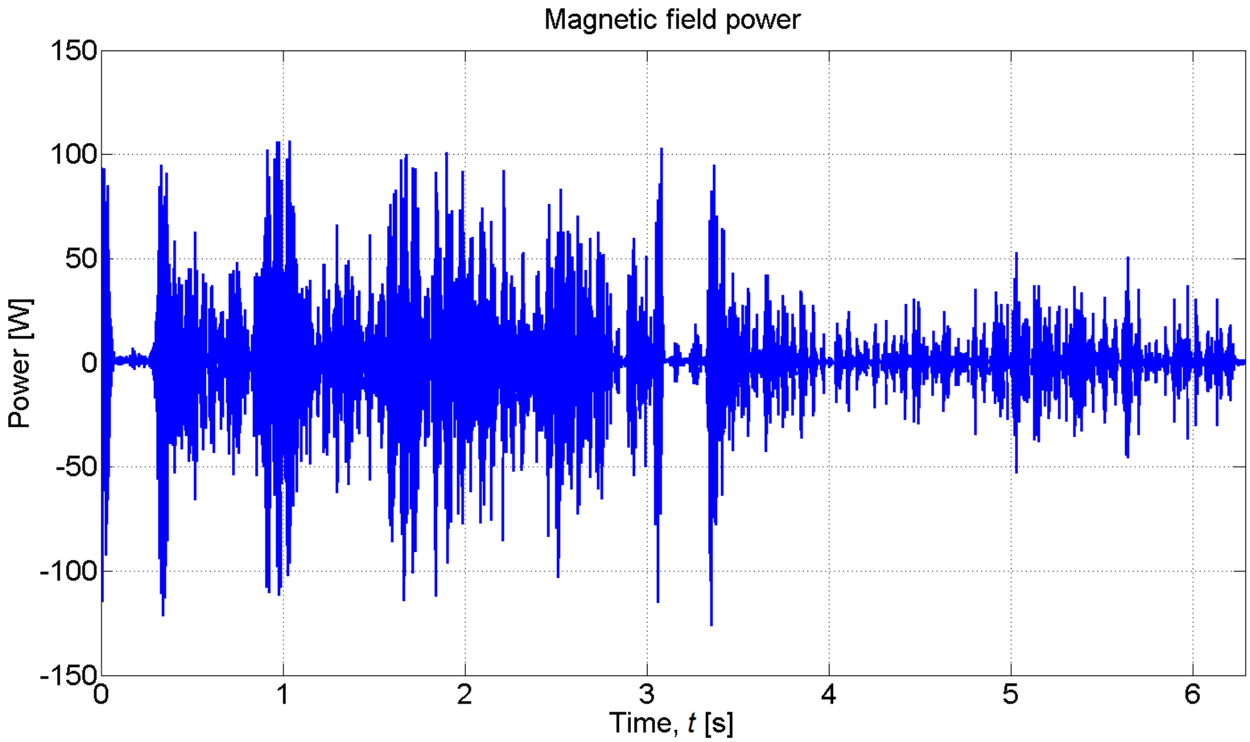
Magnetic field power
150
100
50
0
-50
-100
-150
Power [W]
0
1
2
3
4
5
6
Time, t [s]

(c)

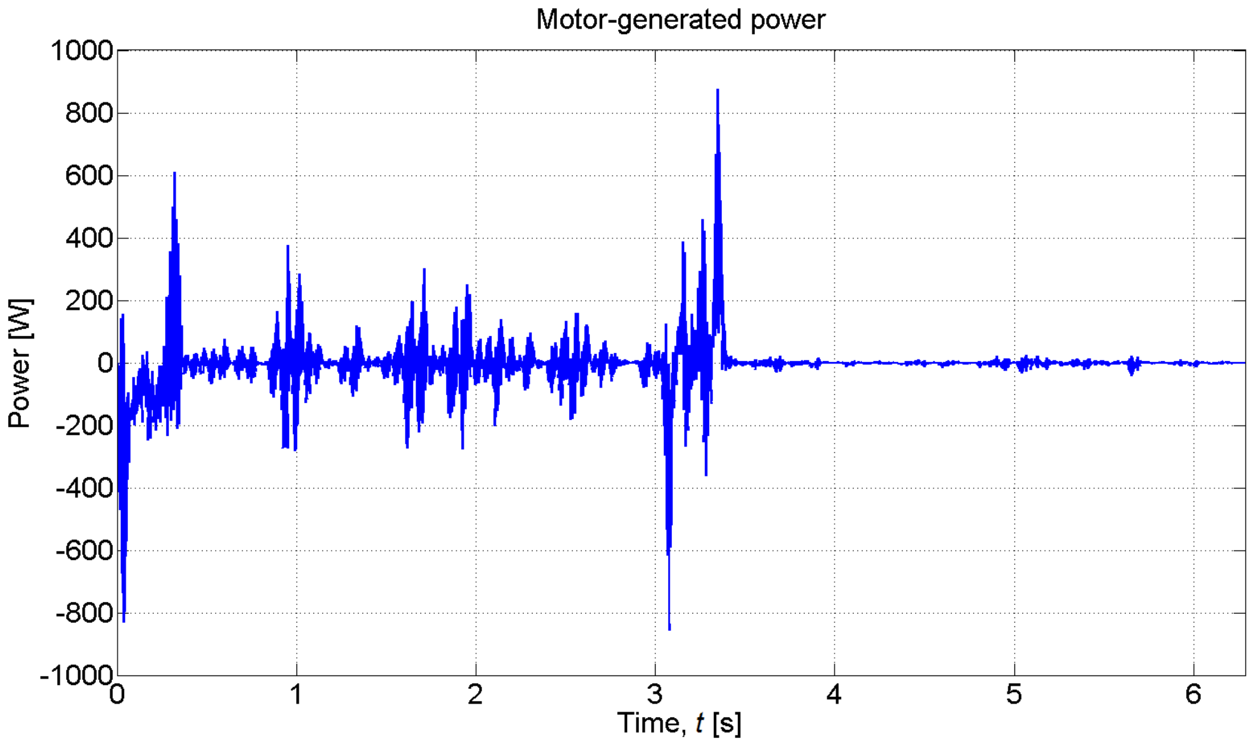

(d)

Figure 18. Motor powers showing (a) the total electrical power at the terminals of the motor, (b) the power loss in the windings, (c) the power stored in the magnetic fields, (d) and the mechanical power on the rotor.

The electrical power at the terminals is the power on the DC bus line. Note that sometimes this power is negative, meaning that the motor is actually sending power back to the source. The reason for this is that the wind load is actually driving the flight control surface, pushing against it as it yields to the wind pressure.

If the drive train is treated as a system, the powers into (positive) and out of (negative) this system are shown in Figure 19.

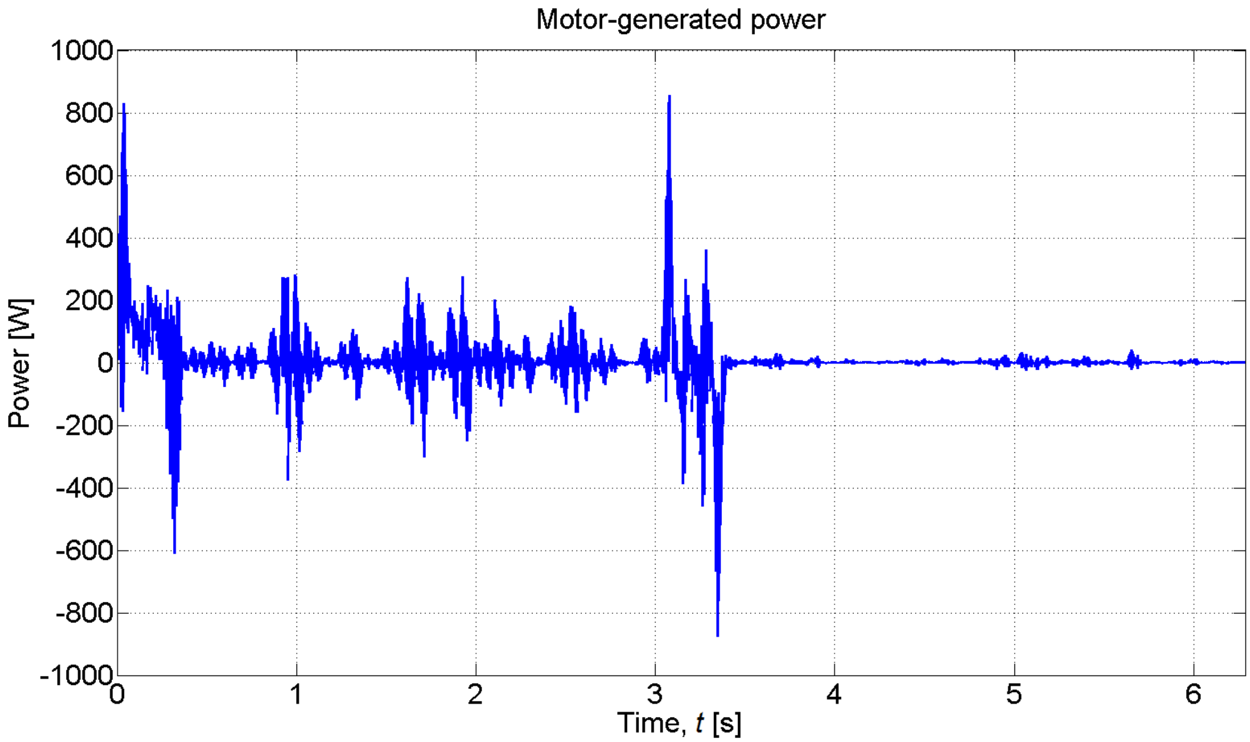
Motor-generated power
Power [W]
1000
800
600
400
200
0
-200
-400
-600
-800
-1000
0
1
2
3
4
5
6
Time, t [s]

(a)

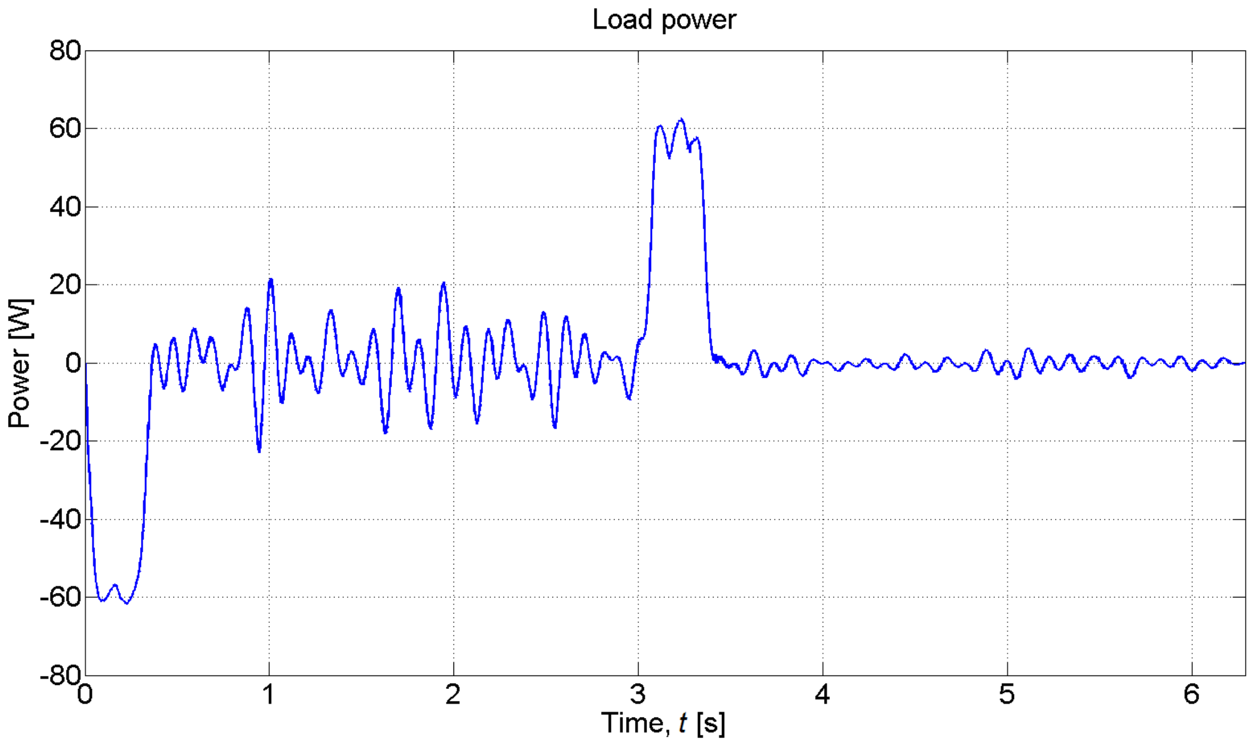

(b)

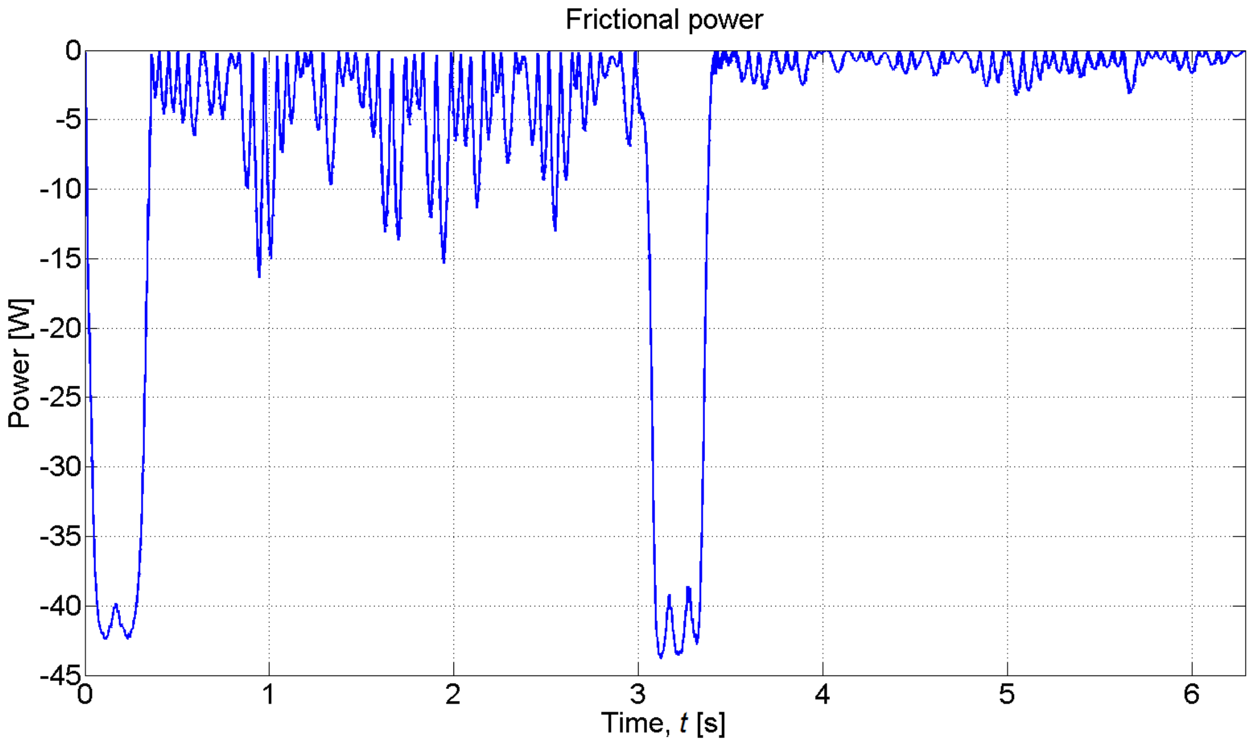
Frictional power
Power [W]
Time, t [s]
0
-5
-10
-15
-20
-25
-30
-35
-40
-45
0
1
2
3
4
5
6

(c)

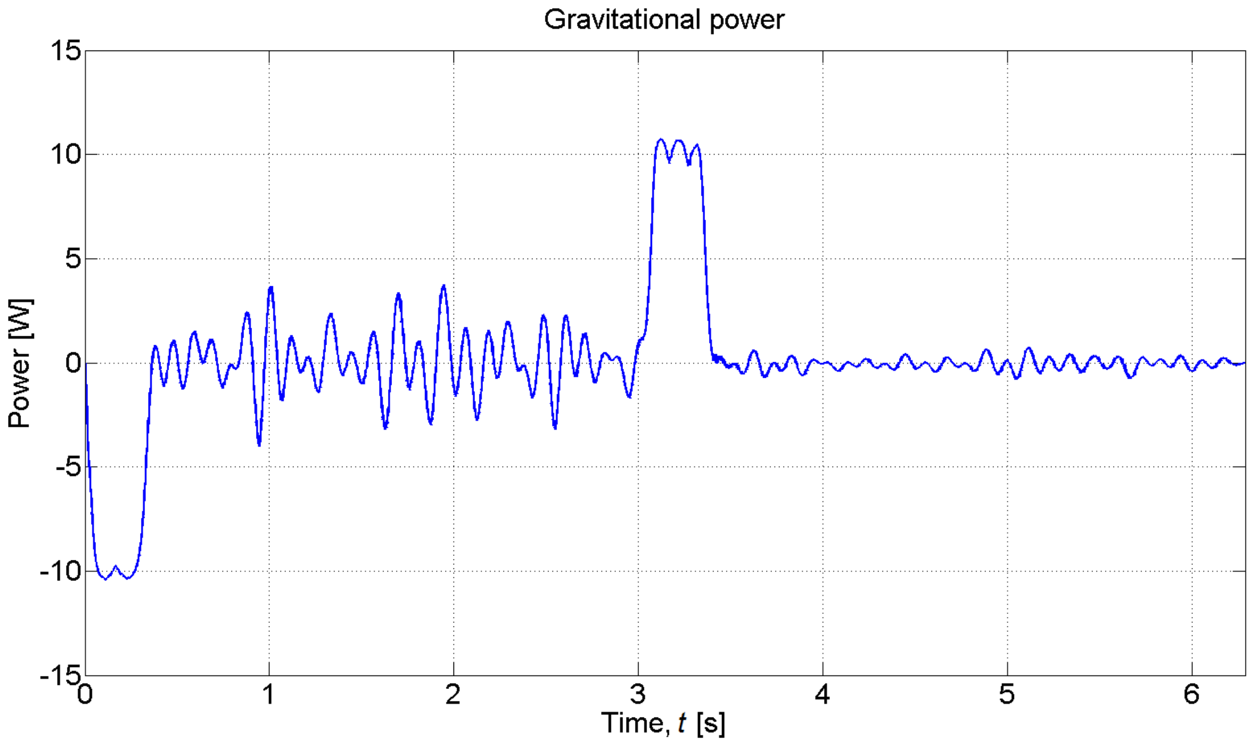

(d)

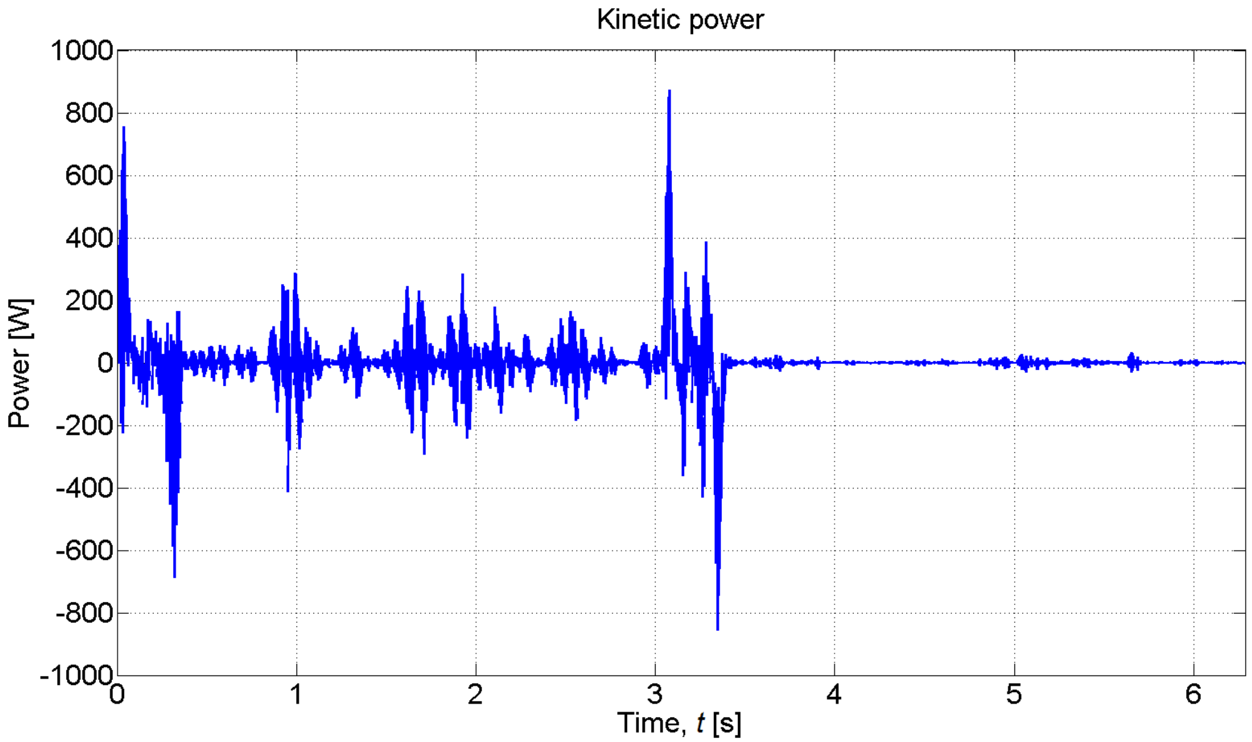

(e)

Figure 19. Drive train powers showing (a) the mechanical power on the rotor, (b) the load power, (c) the frictional power, (d) the gravitational power, (e) and the net kinetic power.

The comparison of the recorded temperatures and the simulated temperature of the stator is shown in Figure 20.

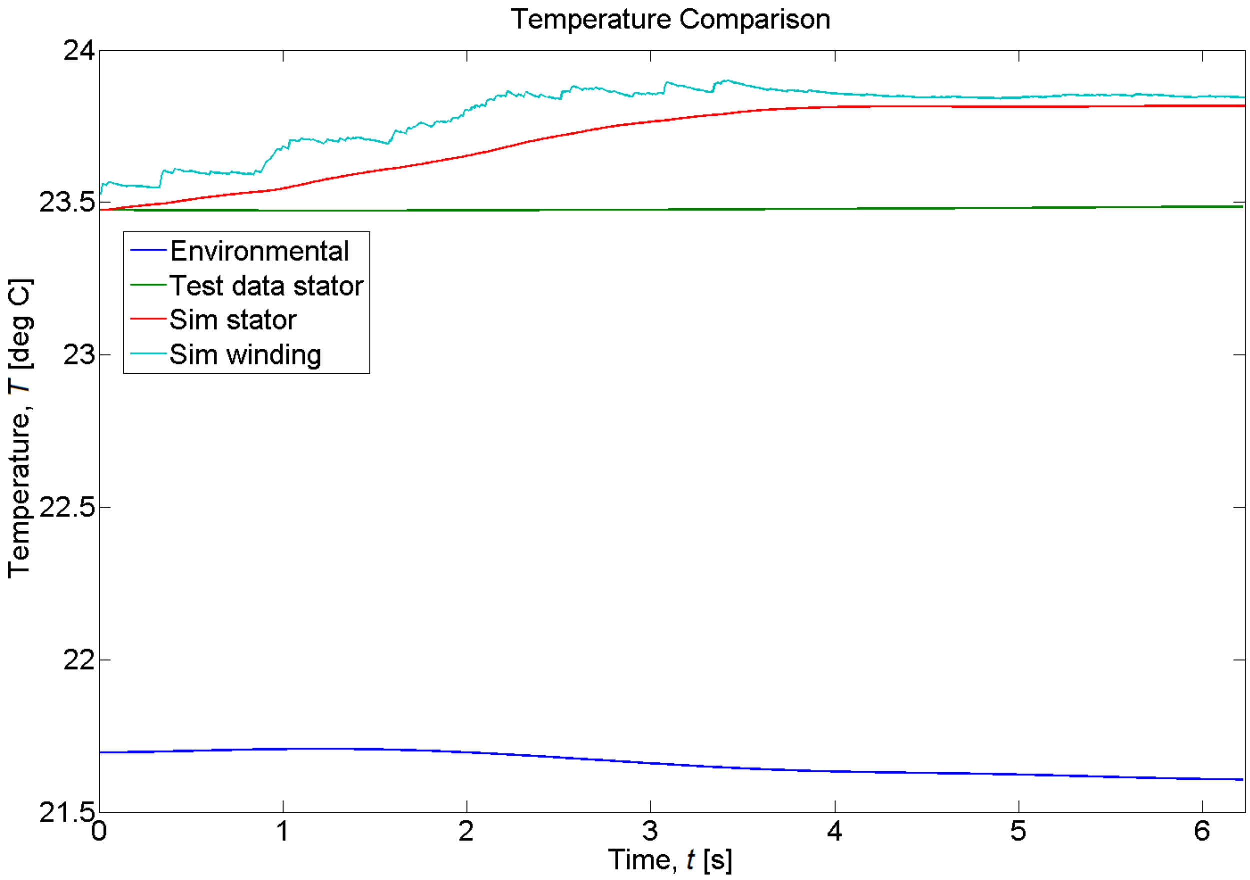
Temperature Comparison
Environmental
Test data stator
Sim stator
Sim winding
Temperature, T [deg C]
24
23.5
23
22.5
22
21.5
0
1
2
3
4
5
6
Time, t [s]

(a)

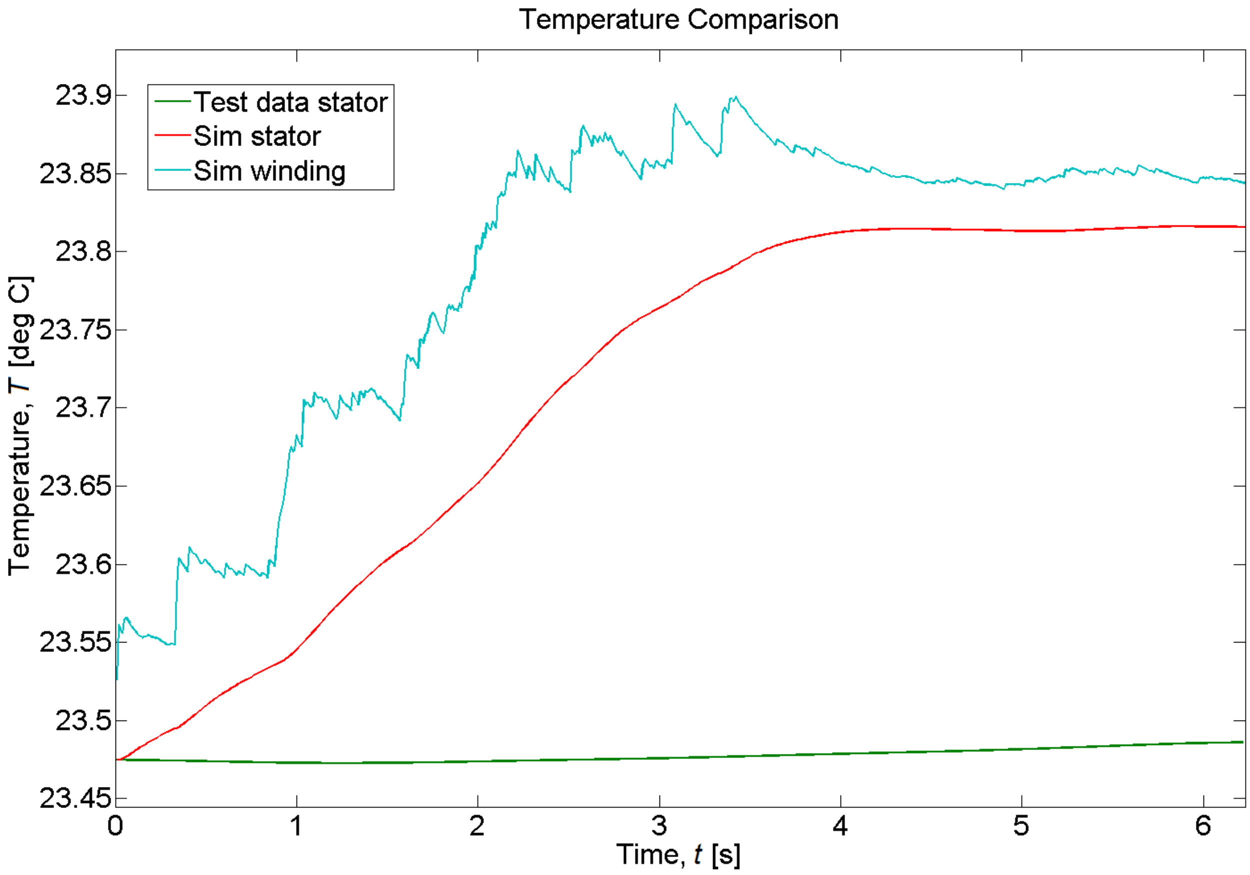

(b)

Figure 20. (a) Temperature comparison and (b) again zoomed in. These plots have environmental temperature (blue), experimentally measured temperature of stator (green), simulated temperature of stator (red), and the simulated temperature of the windings (cyan).

The difference here between simulated and measured stator temperatures is actually quite small, only about 0.34 °C, much less than the 1 °C sensitivity of the thermocouples used.

The accuracy of the temperature prediction is more readily observed for longer simulation profiles. Another test is shown in Figure 21 lasting a half-hour. The simulation of this test matches the stator temperature very well with a maximum error of 0.17 °C.

It is important to note that the power demand, power loss, and, therefore, temperatures are heavily dependent on the efficiency of control. Control tuning can significantly affect the results of the simulation even if the stroke following is practically identical.

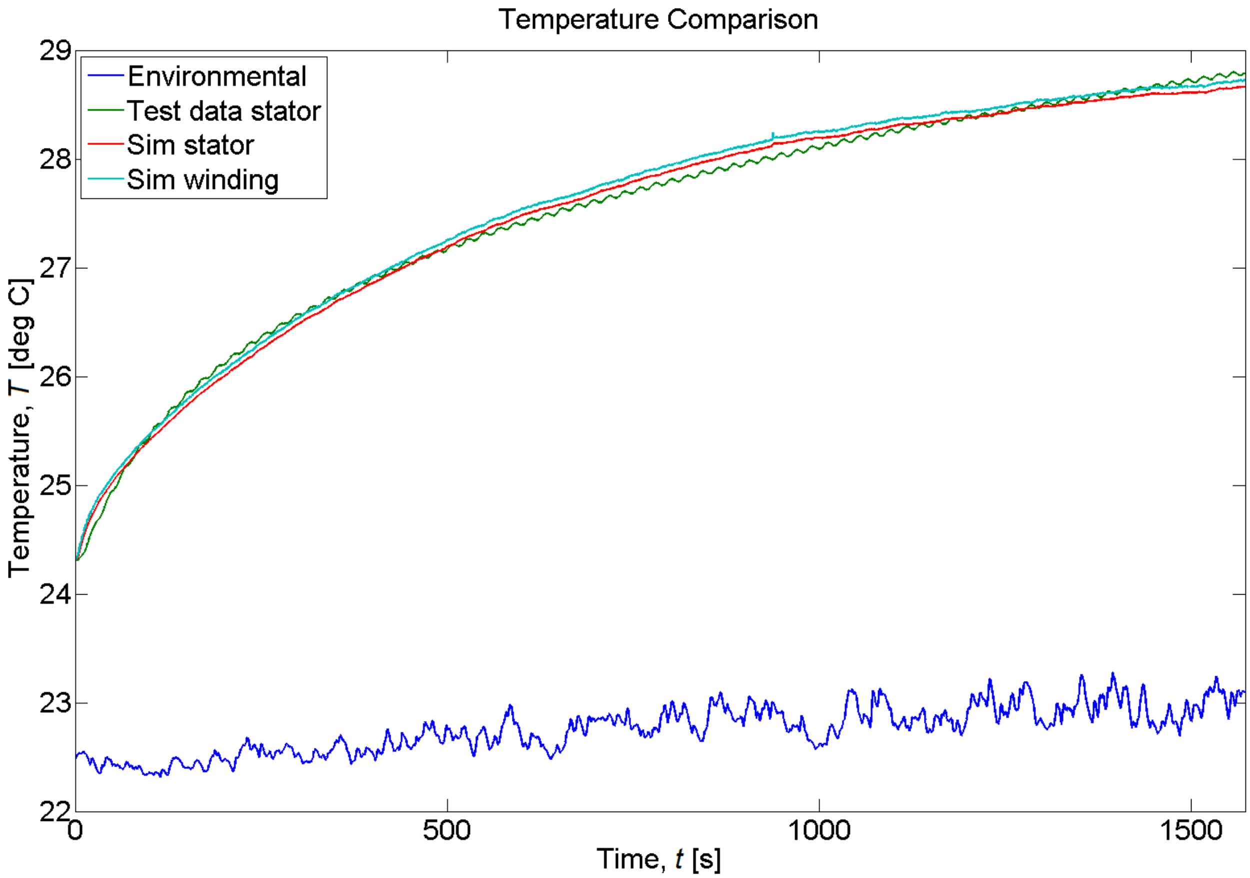

Figure 21. Temperature comparison for a half-hour run showing environmental temperature (blue), experimentally measured temperature of stator (green), simulated temperature of stator (red), and the simulated temperature of the windings (cyan). Note that the simulated temperatures of the windings and stator are about the same, indicating the low thermal resistance in the motor.

Conclusion

There is a strong motivation to move towards all-electric aircraft. However, the significant obstacles to full realization of all-electric aircraft are the thermal management of heat loads and power management. This paper shows the successful implementation of an EMA model with a control algorithm, a PWM component, an electromechanical component with nonlinear parameters, and a thermal component. The model takes a desired position profile, a load force profile, and an environmental temperature profile as inputs and predicts the thermal behavior of the motor and the transient power demands of the EMA. It is shown that control plays a powerful role in how much excess heat is generated and how much the power demand spikes. It is also shown that the temperatures within the motor of the EMA are all within a fairly narrow band. This approach of using finite element method and nonlinear, lumped-element, integrated modeling gives a complete picture of the dynamic behavior of an EMA, thereby helping to make all-electric aircraft a reality.

CHAPTER THREE: NOVEL NONLINEAR INDUCTANCE MODELING OF PERMANENT MAGNET MOTOR

Introduction

An all-electric aircraft is an ambitious, high-priority goal in the avionics community [14]. A typical mission profile for a flight control surface electromechanical actuator (EMA) can be highly dynamic, especially in military aircraft. Both increased reliability and efficiency are its promised implications [1]. EMAs are primary candidates for substitution of non-electric components on aircraft. However, there are thermal [16] and power management challenges due to dynamic mission profiles and the nonlinear behavior of the internal magnetics of such an actuator. These challenges, coupled with the highly flight-critical nature of EMAs, necessitate careful simulations run over a wide range of scenarios before EMAs can be heavily relied upon.

The typical permanent magnet (PM) electric motors in EMAs have fairly nonlinear magnetic behavior, especially as they are operated over non-steady-state mission profiles. If the duty cycle were steady-state or if the air gap between the rotor and stator were large, then linear inductance modeling would be adequate because the magnetic circuits would never get saturated. But, the duty cycle is highly variable and, for the sake of high power density, the air gap is small; therefore, dynamic, nonlinear modeling is necessary.

Finite element method (FEM) assists in developing the nonlinear inductance lookup tables that are important for fast and accurate lumped-element simulation of EMAs. Often, these tables are directly used in simulating an electric machine ([22], [23], and [24]). However, such lookup tables are rough, bounded, and slow. During simulation, it is important that the states of the model transition smoothly. Any roughness in a lookup table can cause perturbations with rippling effects throughout the model leading to reduced numerical stability. Derivatives of such surfaces are especially sensitive to sudden transitions. Furthermore, no matter how large a lookup table is, it has limits, and simply bounding the indices to the lookup table can lead to errors due to discontinuous gradient behavior. Finally, as the tables are made larger to accommodate higher bounds and provide smoother interpolation, the lookup routine becomes slower.

Formulas which can accurately fit the nonlinear surfaces of such lookup tables have the potential to be very smooth, to require far less data to define them, and to compute quickly. It is also desirable that they extrapolate well.

This paper demonstrates a nonlinear inductance formula that is a function of both direct and quadrature (DQ) currents, allowing cross-coupling effects to be included. The process of developing the formula and fitting it to the reference FEM inductance values as well as the results of the fitting and several comparisons to other methods are included. Finally, a comparison of a lumped element simulation using nonlinear inductance is compared with one using linear inductance.

Background

Table I lists several of the variables used in this paper.

Table 6. Simulation States

Symbol	Name	Units
t	Time	s
P	Number of magnetic poles	ND
ϕ	Torque angle	rad
θ_m	Rotor angle	rad
θ_{me}	Rotor angle θ_m times $P/2$	rad
u_d	Direct voltage	V
u_q	Quadrature voltage	V
i_d	Direct current	A
i_q	Quadrature current	A
R_s	Phase resistance	Ω
λ_{PM}	PM flux linkage	Wb
$L_d(i_d,i_q)$	Direct inductance	H
$L_q(i_d,i_q)$	Quadrature inductance	H

The dynamics of a PM electric motor, typical in an EMA, are modeled by four primary dynamical equations in the DQ0-reference frame [25]. Two of these equations model the electrical behavior of the motor:

$$\frac{di_d}{dt} = \frac{L_{qq}G_d - L_{dq}G_q}{L_{dd}L_{qq} - L_{dq}L_{qd}} \tag{28}$$

$$\frac{di_q}{dt} = \frac{L_{dd}G_q - L_{qd}G_d}{L_{dd}L_{qq} - L_{dq}L_{qd}}\,, \tag{29}$$

where

$$L_{dd} = L_d + i_d \frac{dL_d}{di_d} \tag{30}$$

$$L_{dq} = i_d \frac{dL_d}{di_q} \tag{31}$$

$$L_{qd} = i_q \frac{dL_q}{di_d} \tag{32}$$

$$L_{qq} = L_q + i_q \frac{dL_q}{di_q} \tag{33}$$

$$G_d = u_d - R_s i_d + \left(L_q i_q\right)\frac{d\theta_{me}}{dt} \tag{34}$$

$$G_q = u_q - R_s i_q - \left(L_d i_d + \lambda_{PM}\right)\frac{d\theta_{me}}{dt} . \tag{35}$$

The full derivation can be found in Appendix A: Permanent Magnet Machine Dynamics. The other two dynamical equations model the mechanical behavior of the motor. Equations (28) and (29) come from the voltage equations (36) and (37):

$$u_d = R_s i_d + L_{dd} \frac{di_d}{dt} + L_{dq} \frac{di_q}{dt} - L_q i_q \frac{d\theta_{me}}{dt} \tag{36}$$

$$u_q = R_s i_q + L_{qd} \frac{di_d}{dt} + L_{qq} \frac{di_q}{dt} + \left(L_d i_d + \lambda_{PM}\right)\frac{d\theta_{me}}{dt} . \tag{37}$$

These equations carry the assumption that the variations in inductances over rotor angle can be reasonably averaged out, that the flux linkage from the permanent magnets appears only in the direct axis, and that the motor is balanced.

Though phase resistance and PM flux linkage do vary with current magnitude, temperature, and frequency, the focus of this paper is the six inductance properties: L_d and L_q and their current derivatives dL_d/di_d, dL_d/di_q, dL_q/di_d, and dL_q/di_q.

Method of Analysis

Collecting the data

The process of creating a formula to fit inductance values begins with getting the inductance values. Using ANSYS Maxwell 2D, an FEM software package, a PM motor is simulated in high detail and the ABC-reference inductance values for each phase are stored as current magnitude, torque angle, and rotor angle are varied. The torque angle is the angle produced by the direct and quadrature current vectors. The rotor angle (θ_m) is the angle of the rotor with respect to the phase A axis. The inductance values are then translated to the DQ0-reference frame using the Park and Clarke transforms [30]. Averaging the inductances over rotor angle, the direct and quadrature inductances (L_d and L_q, respectively) are shown as functions of direct and quadrature currents in Figure 22 and Figure 23.

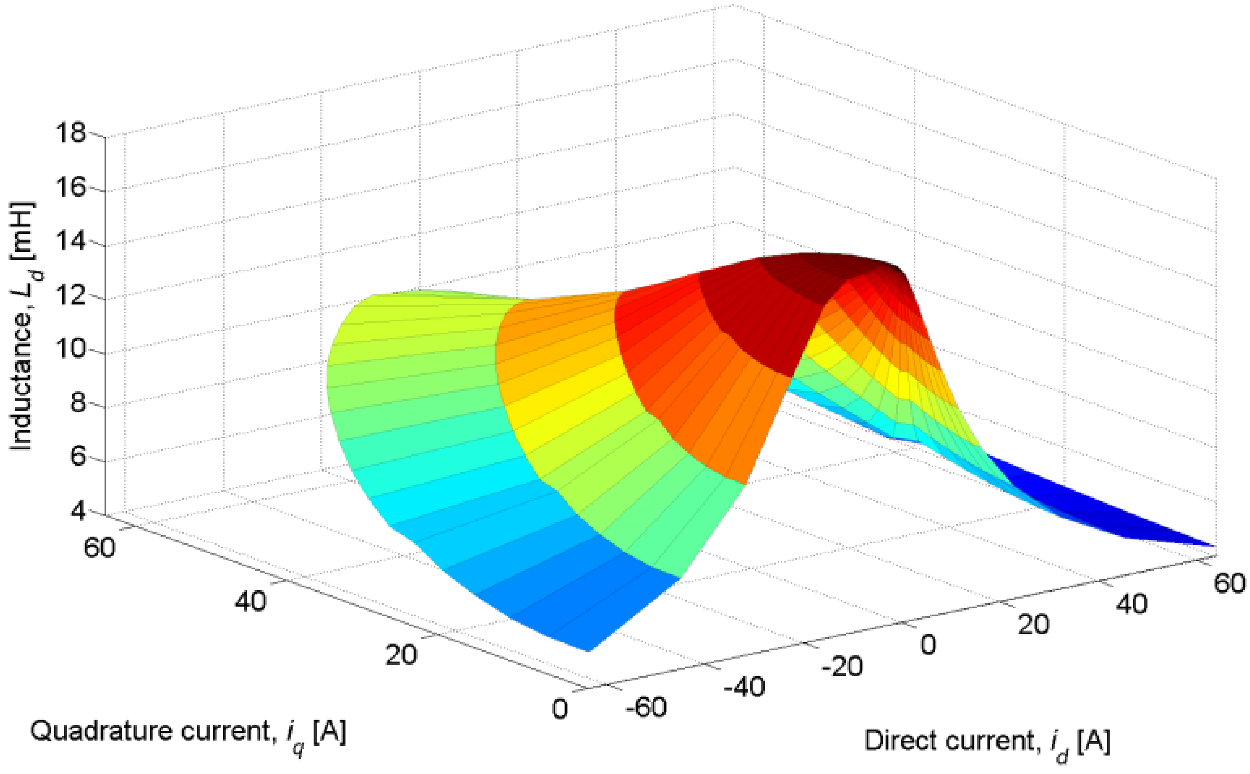

Figure 22. Direct inductance L_d as a function of i_d and i_q.

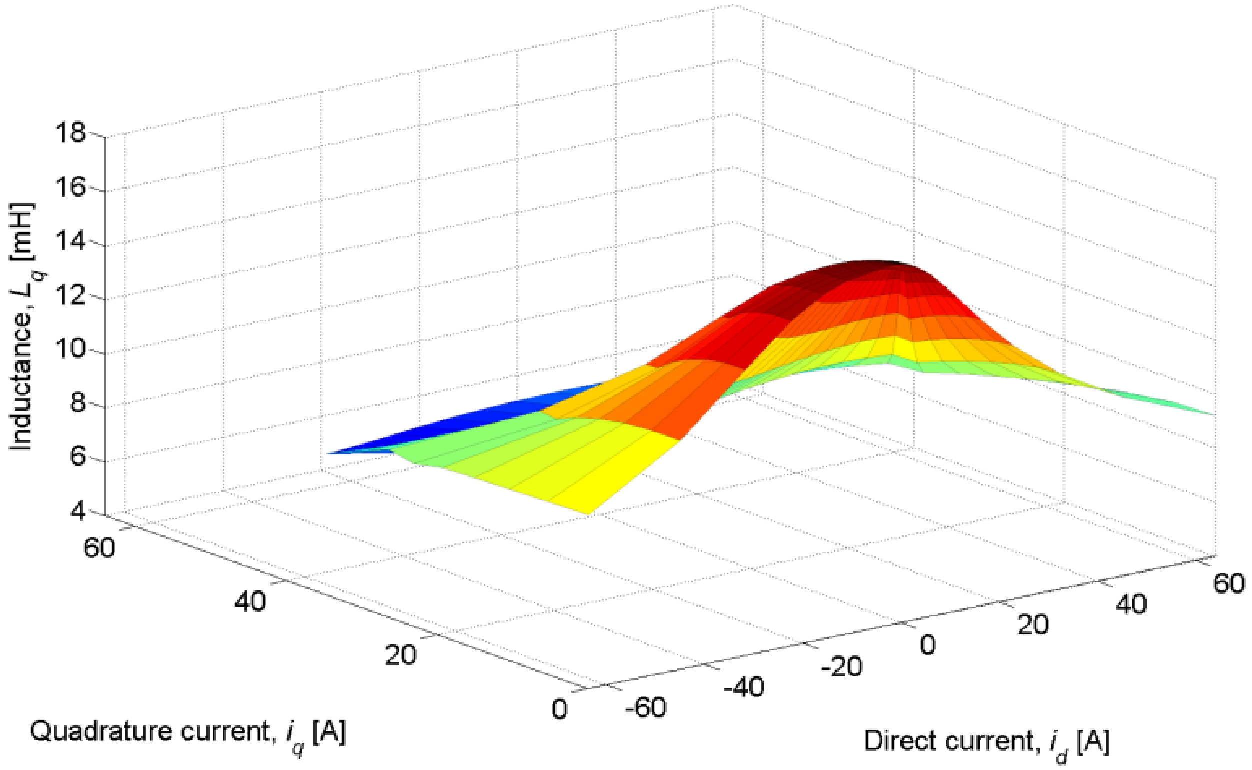

Figure 23. Quadrature inductance L_q as a function of i_d and i_q.

Depending on the maximum current of interest, averaging inductance over rotor angle can be considered reasonable. The variation in inductance magnitude over rotor angle increases with current magnitude. An example of this behavior is shown in Figure 24 and Figure 25. In this case, for a current magnitude less than 16 A, averaging over this variation is reasonable.

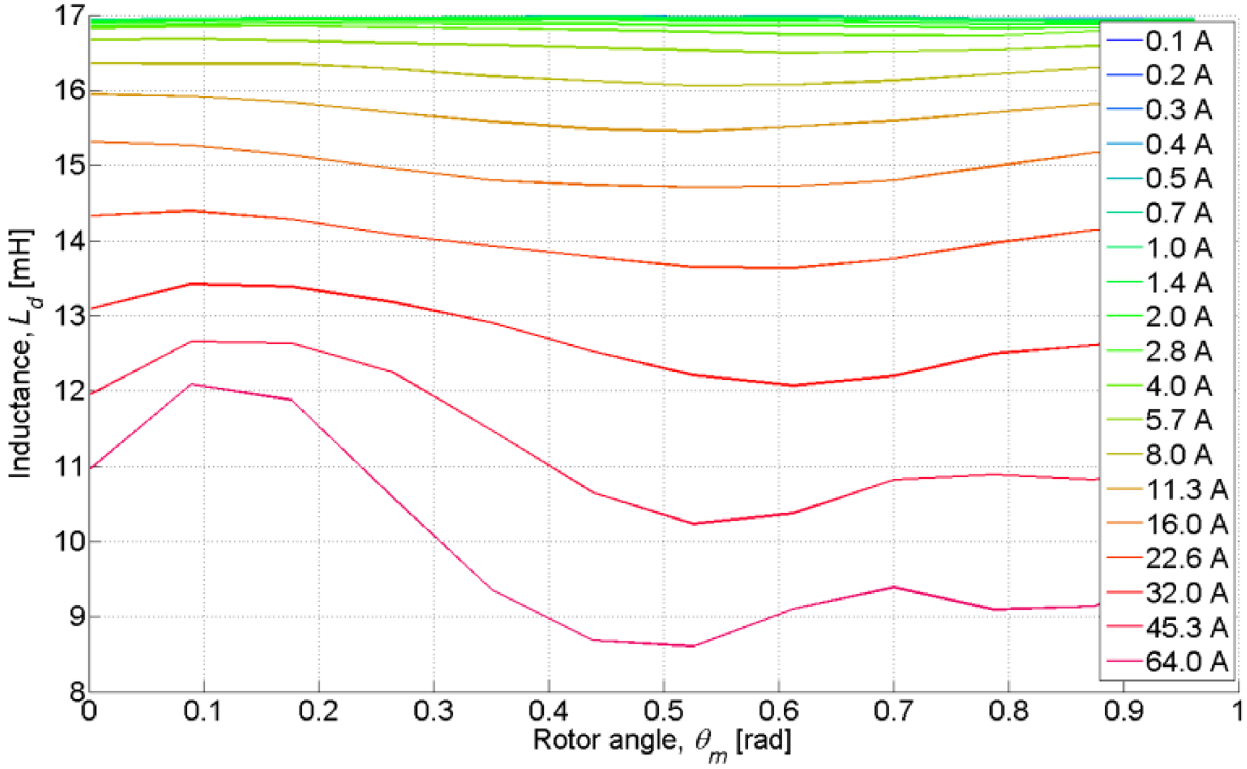

Figure 24. Direct inductance L_d as a function of rotor angle for a particular torque angle and for various values of current magnitude.

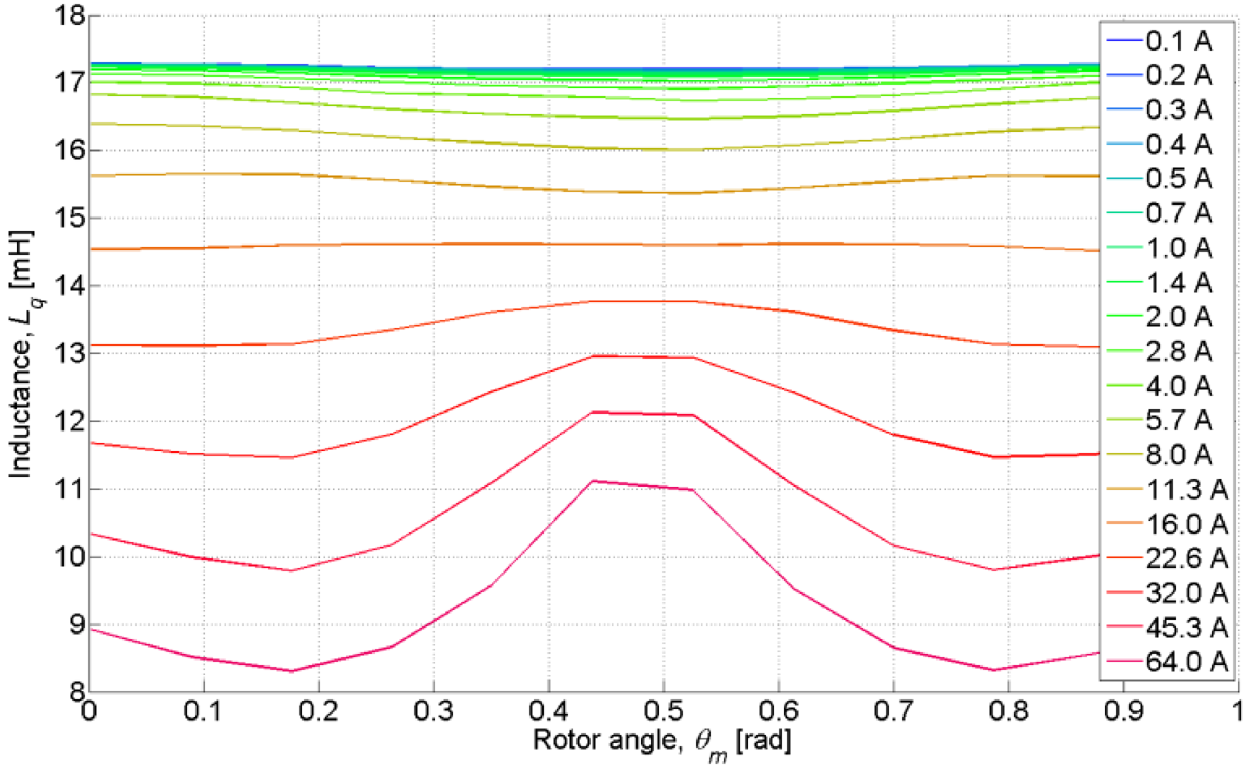

Figure 25. Quadrature inductance L_q as a function of rotor angle for a particular torque angle and for various values of current magnitude.

The inductances vary smoothly over currents and angles, but the resolution of the data shown is somewhat low because running FEM simulations is time-consuming. In order to make good fits to the data, it helps if the resolution is higher. Therefore, the data is smoothly interpolated.

Interpolating the data

The inductances are spline interpolated to help reduce the Runge effect during fitting later on. This also helps in analyzing the derivatives of the inductance tables with respect to current. The direct and quadrature inductances after interpolation are shown in Figure 26 and Figure 27, respectively.

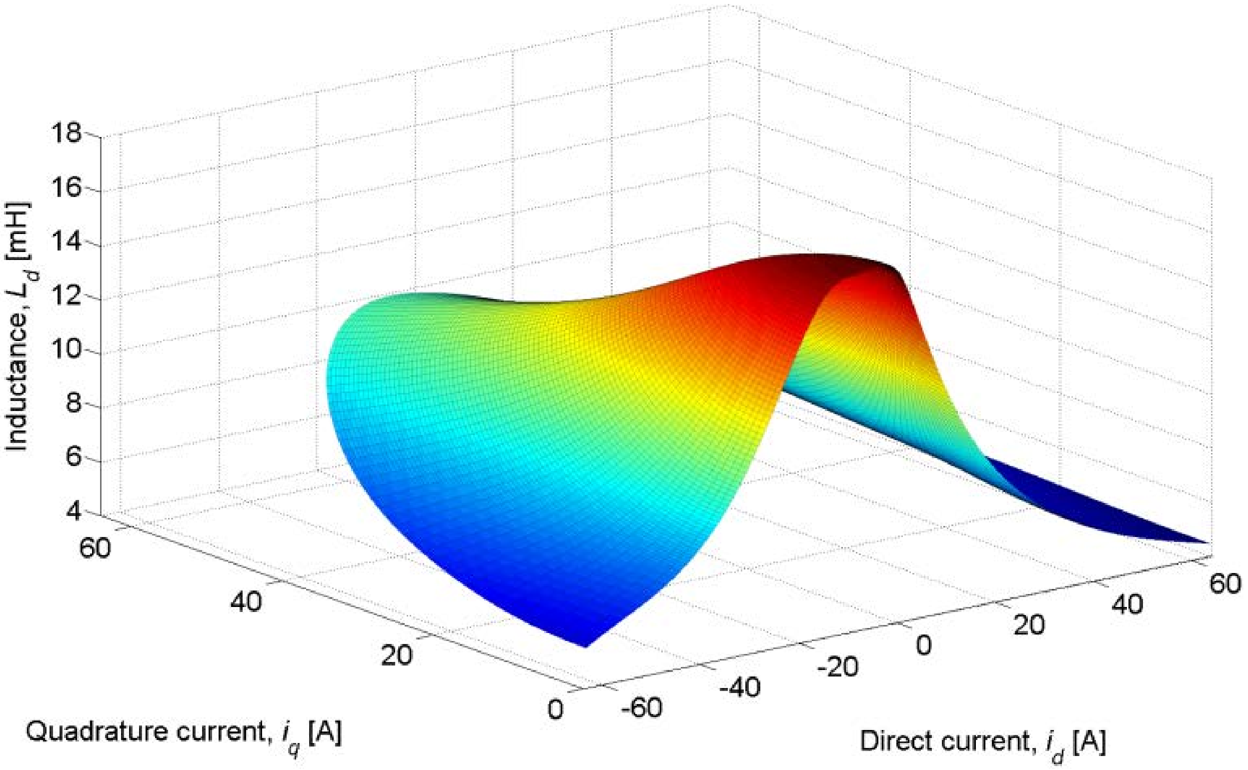

Figure 26. Direct inductance L_d after being interpolated.

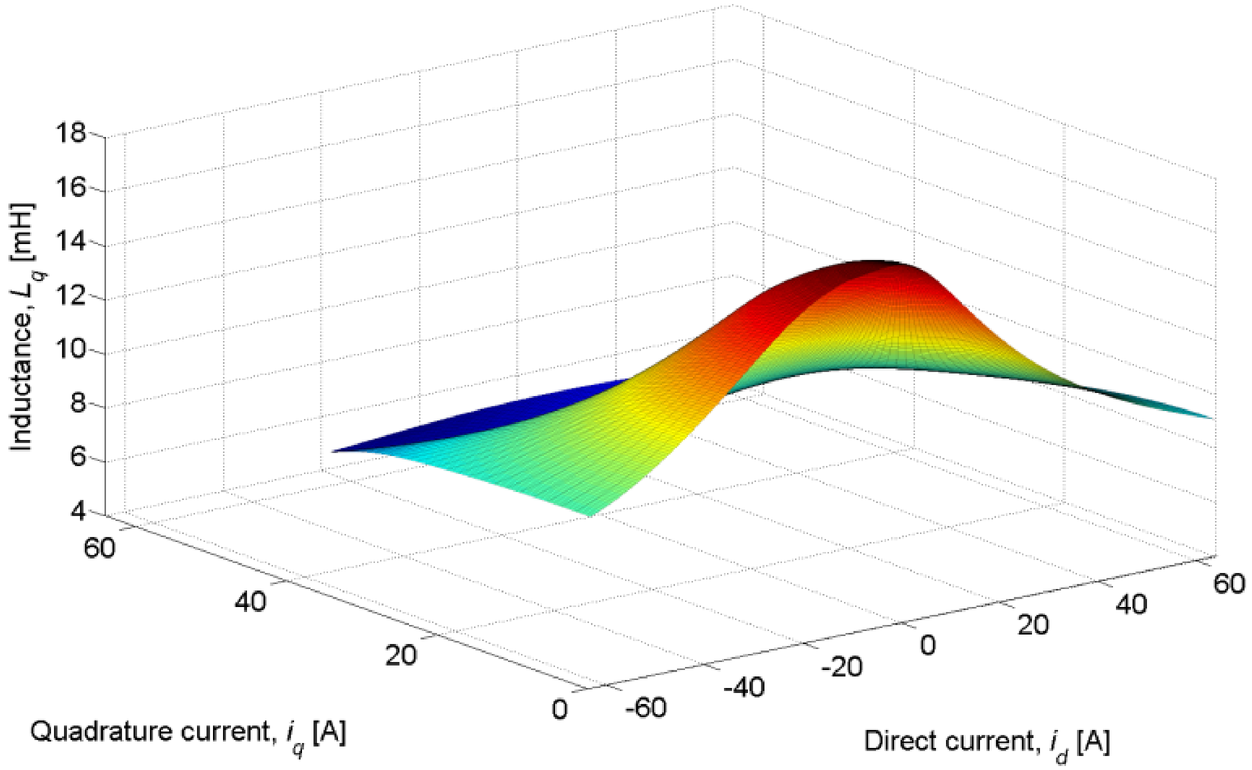

Figure 27. Quadrature inductance L_q after being interpolated.

With smoothly interpolated inductances, their derivatives with respect to current can be numerically calculated using very small steps in current. So, from the two inductance tables, L_d and L_q, four more tables are developed: dL_d/di_d, dL_d/di_q, dL_q/di_d, and dL_q/di_q. These are shown in Figure 28.

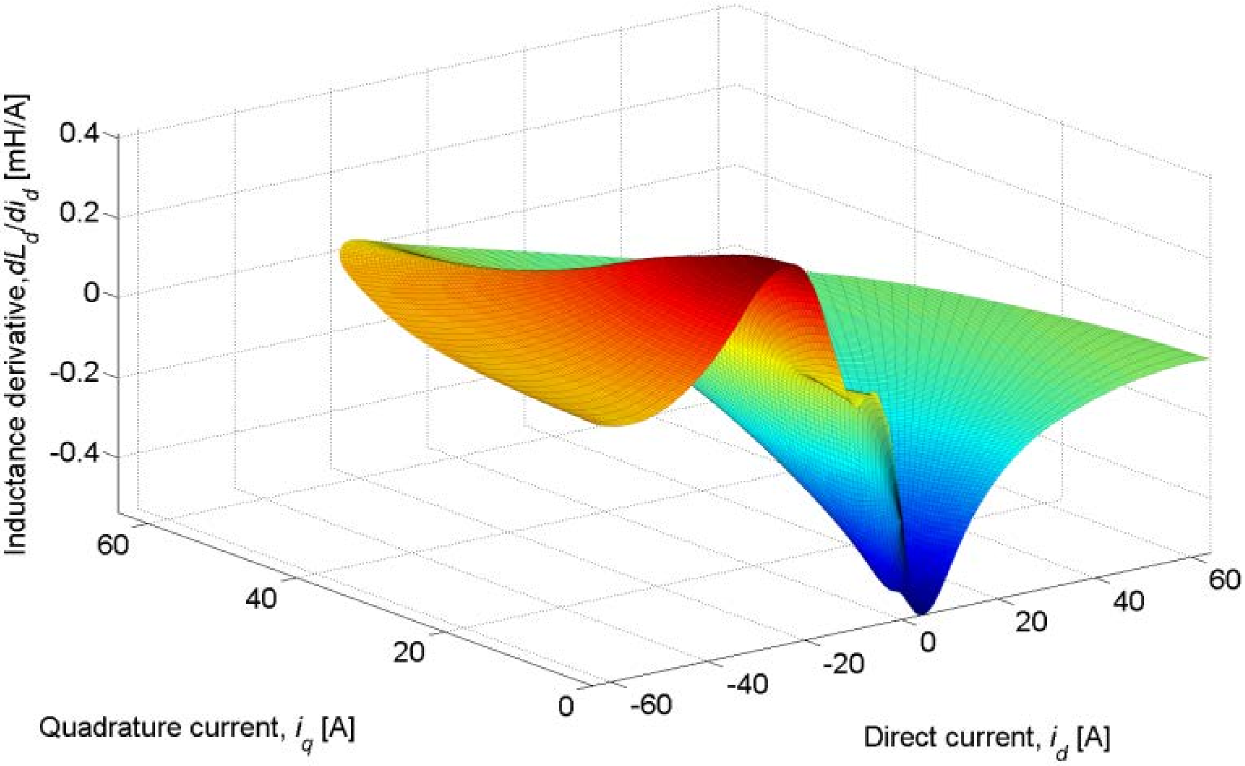
Inductance derivative, dL_d/di_d [mH/A]
0.4
0.2
0
-0.2
-0.4
60
40
20
0
Quadrature current, i_q [A]
-60
-40
-20
0
20
40
60
Direct current, i_d [A]

(a)

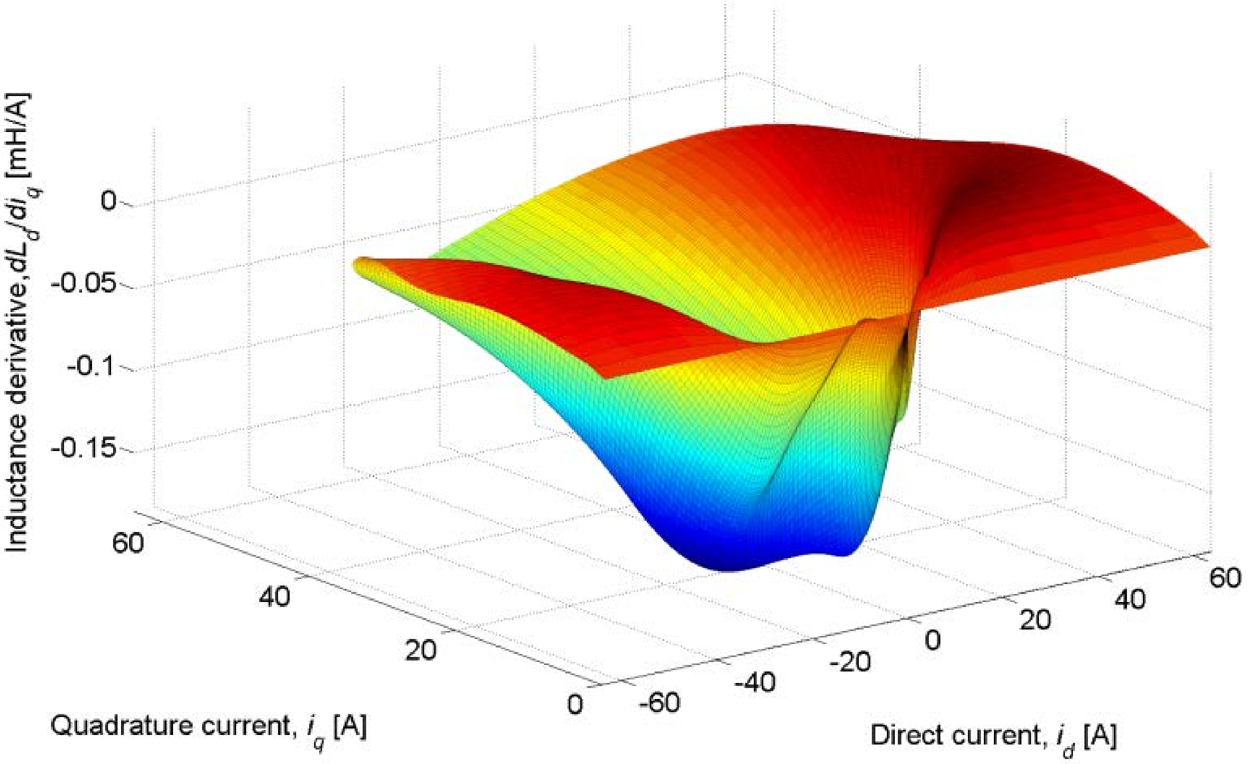
Inductance derivative, dL_d/di_q [mH/A]
0
-0.05
-0.1
-0.15
60
40
20
0
Quadrature current, i_q [A]
-60
-40
-20
0
20
40
60
Direct current, i_d [A]

(b)

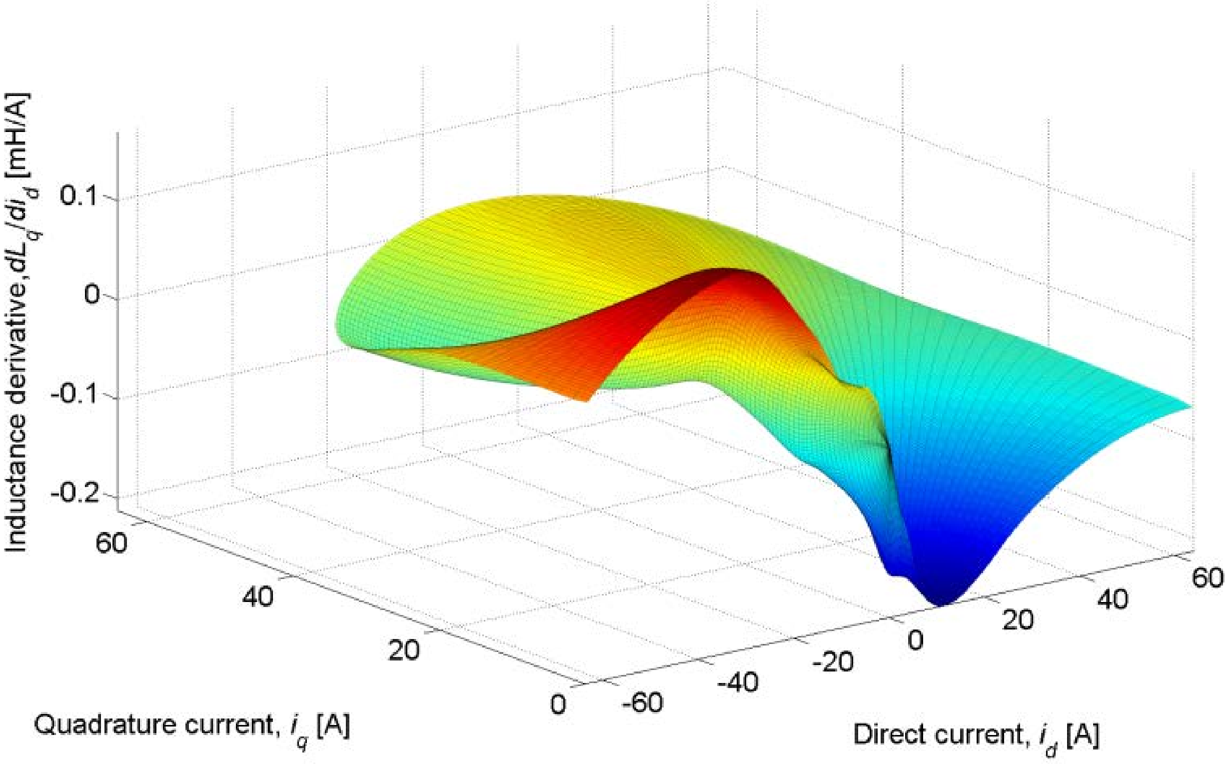
Inductance derivative, dL_q/di_d [mH/A]
0.1
0
-0.1
-0.2
60
40
20
0
Quadrature current, i_q [A]
-60
-40
-20
0
20
40
60
Direct current, i_d [A]

(c)

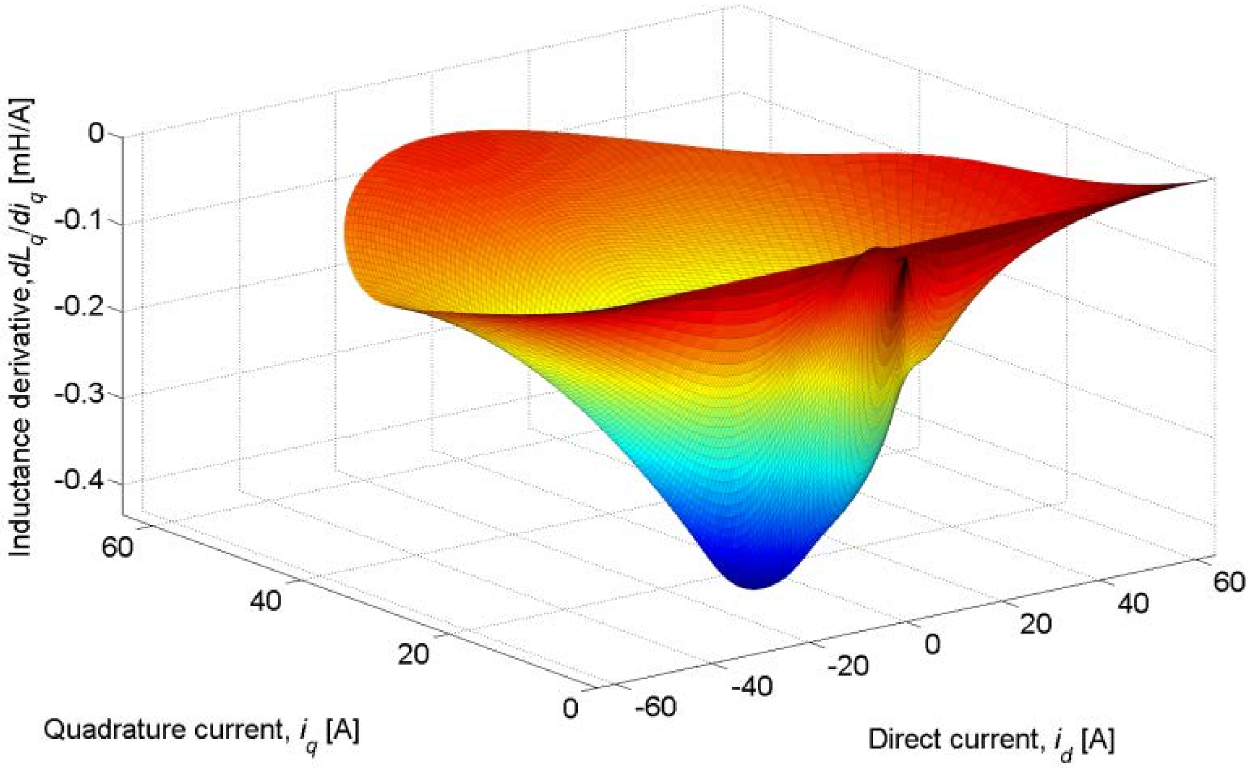

(d)

Figure 28. Inductance derivatives: (a) dL_d/di_d, (b) dL_d/di_q, (c) dL_q/di_d, and (d) dL_q/di_q.

These derivatives are made part of the verification of good fitting since they are used in the motor equations (28) and (29).

Shifting the data

It is interesting to note that the peaks of the inductances are not naturally at the origin. Direct inductance L_d versus direct current i_d is shown in Figure 29. The peak of this curve is at a somewhat negative current.

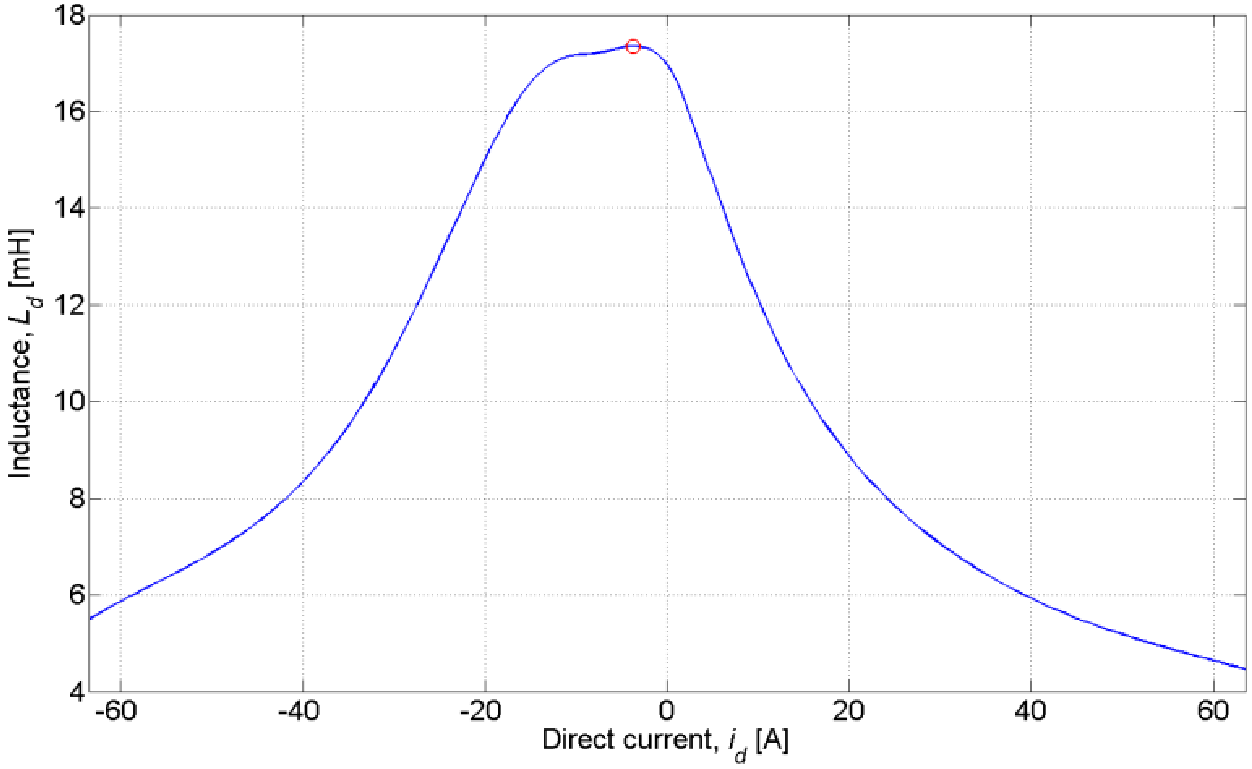

Figure 29. L_d as a function of direct current where quadrature current is zero. The peak is circled in red at -3.77 A.

Because of the nature of the particular fitting function demonstrated in this paper, the peaks of the inductance surfaces must be at the origin. Therefore, the inductance surfaces are shifted prior to fitting. A shift can be added later to get the correct values from the formula. Figure 30 shows the before and after of dL_d/di_d (from Figure 28 (a)).

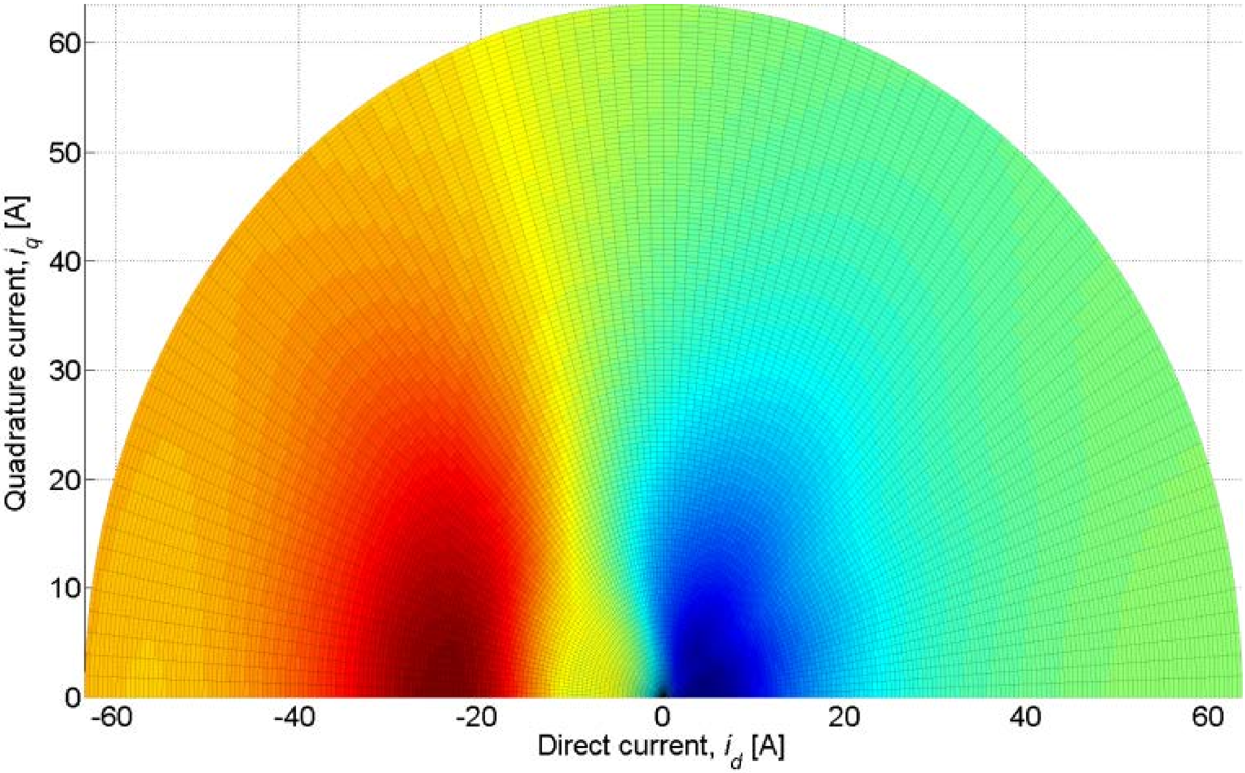
Quadrature current, i_q [A]
60
50
40
30
20
10
0
-60
-40
-20
0
20
40
60
Direct current, i_d [A]

(a)

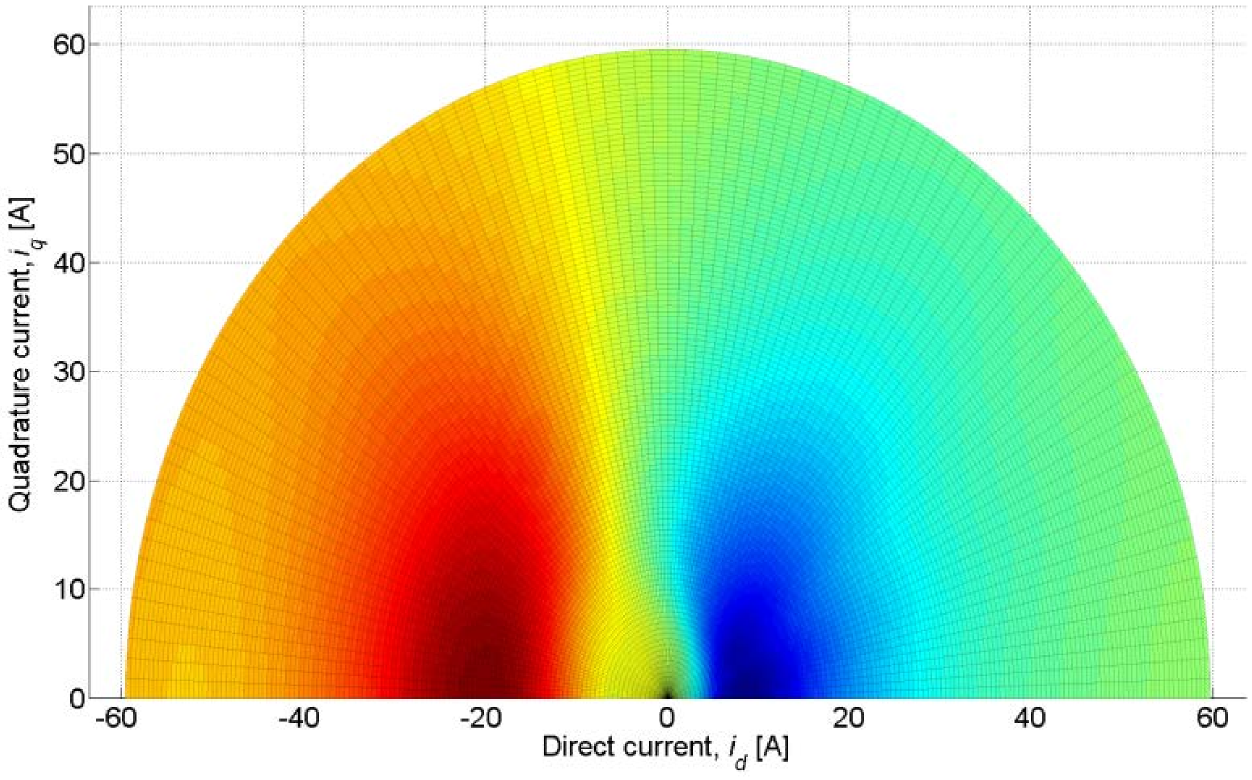

(b)

Figure 30. Inductance derivative dL_d/di_d (a) before being shifted and (b) after being shifted. Note that between the two versions, the red and blue regions are shifted to the right in (b). Also, note that the domain of the surface is cropped slightly to maintain symmetry.

Fitting along current

As seen in Figure 29, inductance generally decreases with current magnitude. And, this is definitely the case after the inductance surfaces have been shifted so that their peaks are at the origin. A rational function is used to fit inductance versus current using either 5 coefficients (38) or 7 coefficients (39):

$$L(i) = \frac{k_1}{(ik_2)^{k_3} + (ik_4)^{k_5} + 1} + (L_{peak} - k_1) \tag{38}$$

$$L(i)=\frac{k_1+(ik_2)^{k_3}}{(ik_4)^{k_5}+(ik_6)^{k_7}+1}+\left(L_{peak}-k_1\right), \tag{39}$$

where i is current magnitude, the k variables are the tuning coefficients, and L_{peak} is a constant. The reason for using a rational function is that it extrapolates well. Whereas polynomial functions tend to suffer from Runge's phenomenon [31], diverging wildly beyond the region of fitting, rational functions tend to demonstrate asymptotic behavior along the abscissa, which is very appropriate for saturating phenomena. Although a primary concern in using rational functions is the occurrence of singularities, as long as the k coefficients are positive all the poles will be in the negative. Since i is always positive, these poles will never be seen and no singularities will occur.

Both the (38) and (39) functions are fit to the inductance surfaces for each value of torque angle using an optimization algorithm. Upon testing, the Nelder-Mead algorithm *fminsearch* (from MATLAB) produces very erratic results. Though it tunes an individual case very well, it tends to over-tune, leading to k values which differ greatly from one torque angle to the next. Instead, the resilient backpropagation heuristic [32] is used. It is a gradient sign optimization. This results in very good fits with excellent continuity of k values over torque angle.

Using (38), the 5-k inductance fits for L_d and L_q are shown in Figure 31, and using (39), the 7-k inductance fits for L_d and L_q are shown in Figure 32. The 7-k function tends to fit the individual inductance curves better than the 5-k function. However, as is shown later, the 5-k function gives a better overall fit.

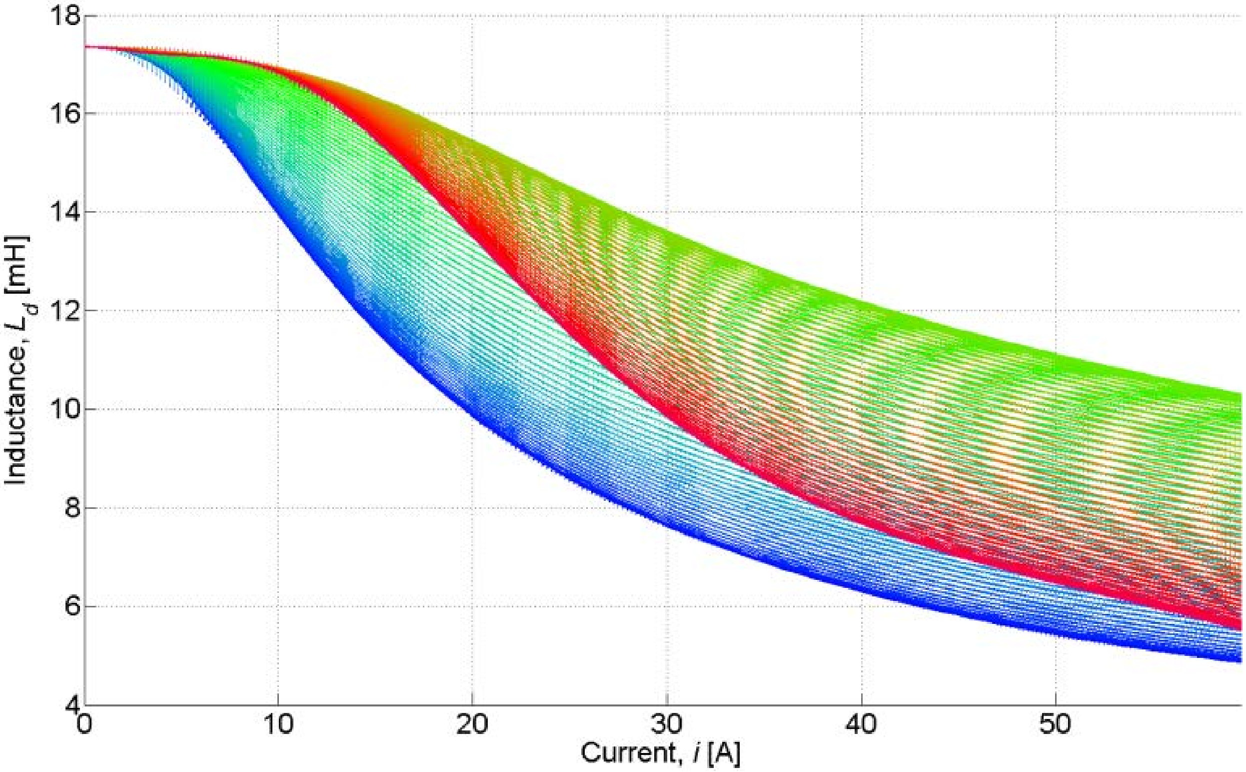

(a)

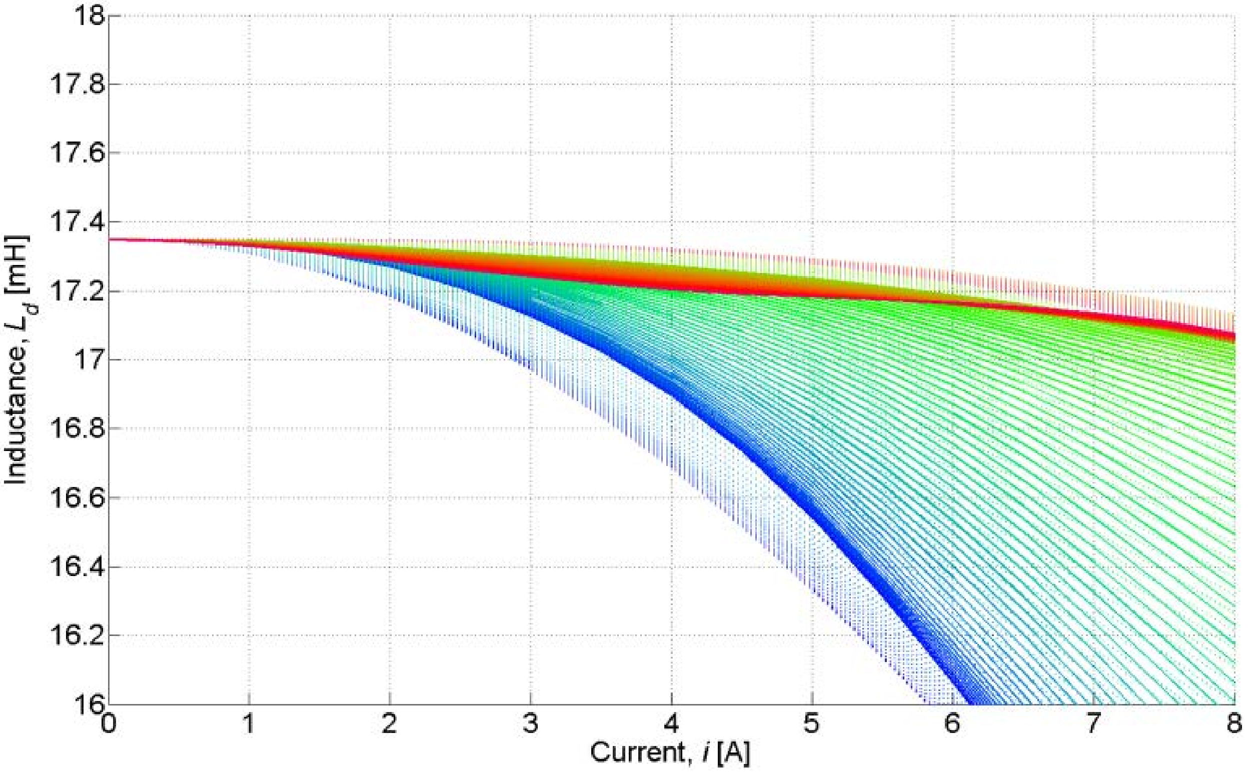
18
17.8
17.6
17.4
17.2
17
16.8
16.6
16.4
16.2
16
Inductance, L_d [mH]
0
1
2
3
4
5
6
7
8
Current, i [A]

(b)

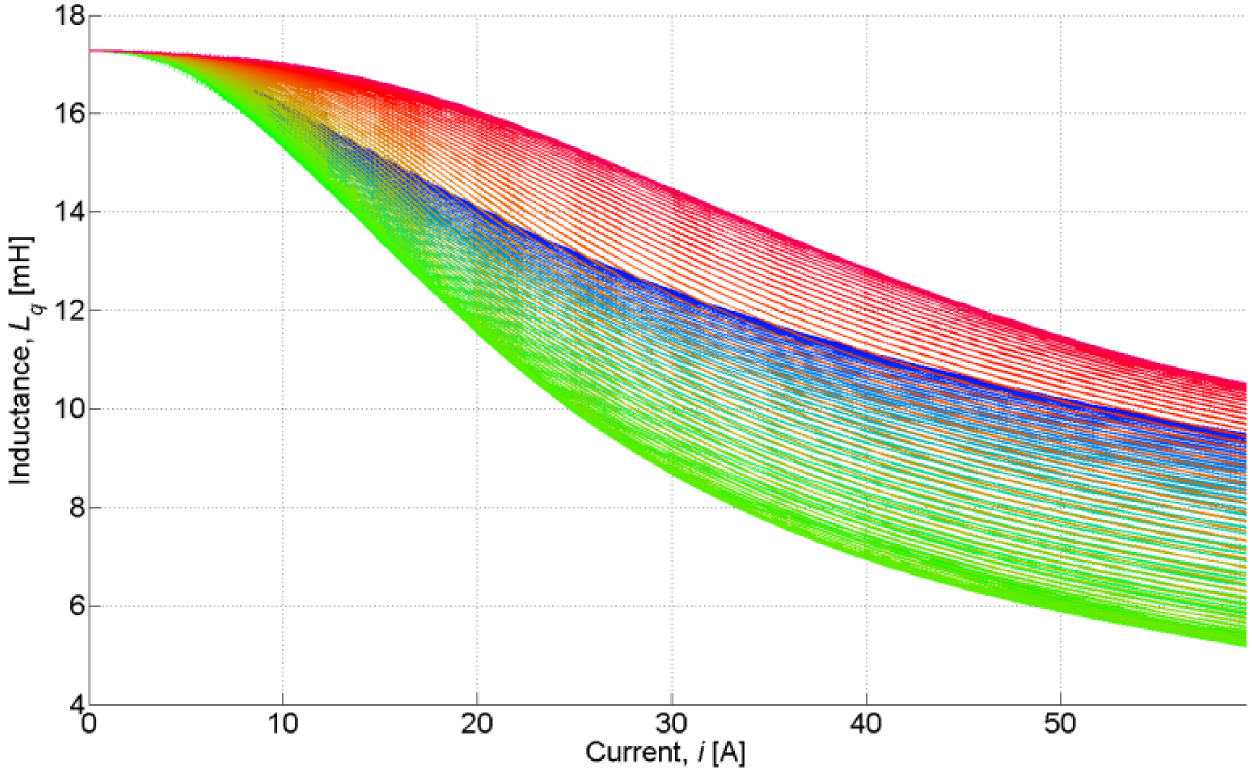

(c)

Figure 31. Fits with 5-k values for (a) L_d, (b) L_d zoomed in, and (c) L_q. The original data is shown with solid curves, and the fitted data is shown with dashed curves, where each color corresponds to a unique torque angle. Note the slight disparity near the peak of L_d as seen in (b).

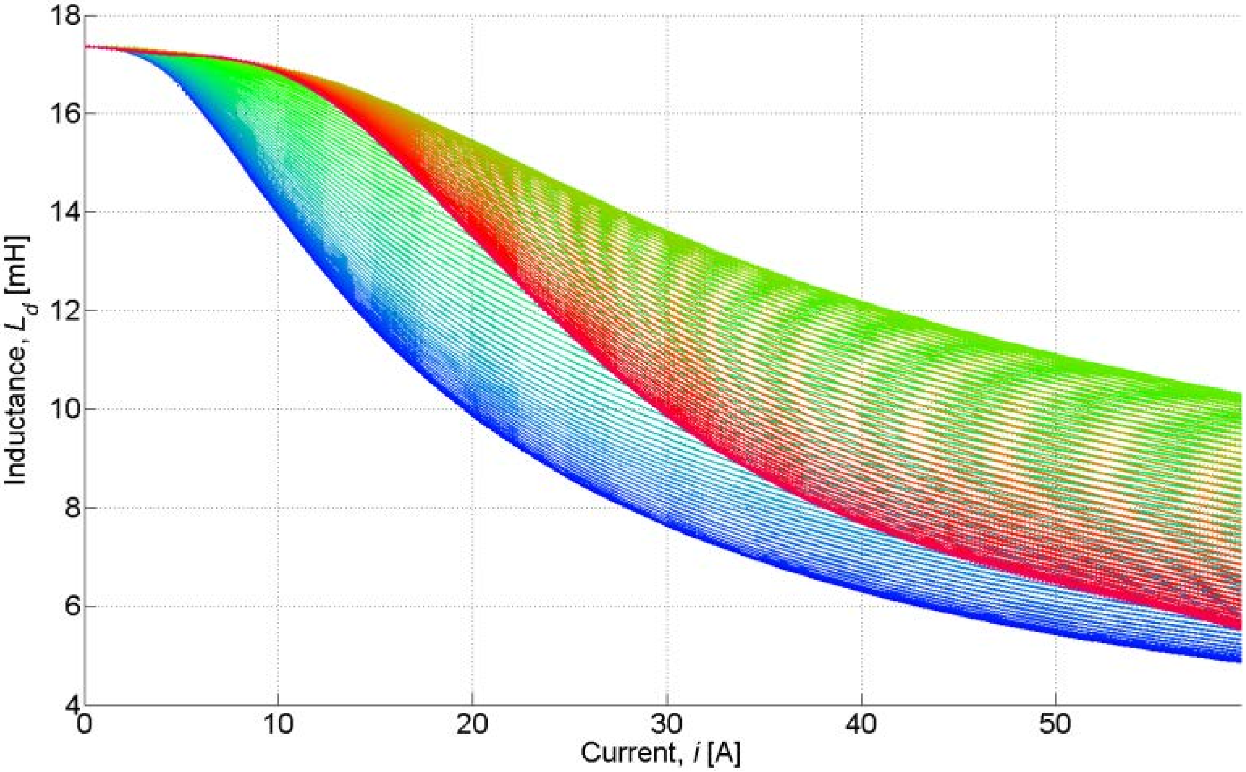

(a)

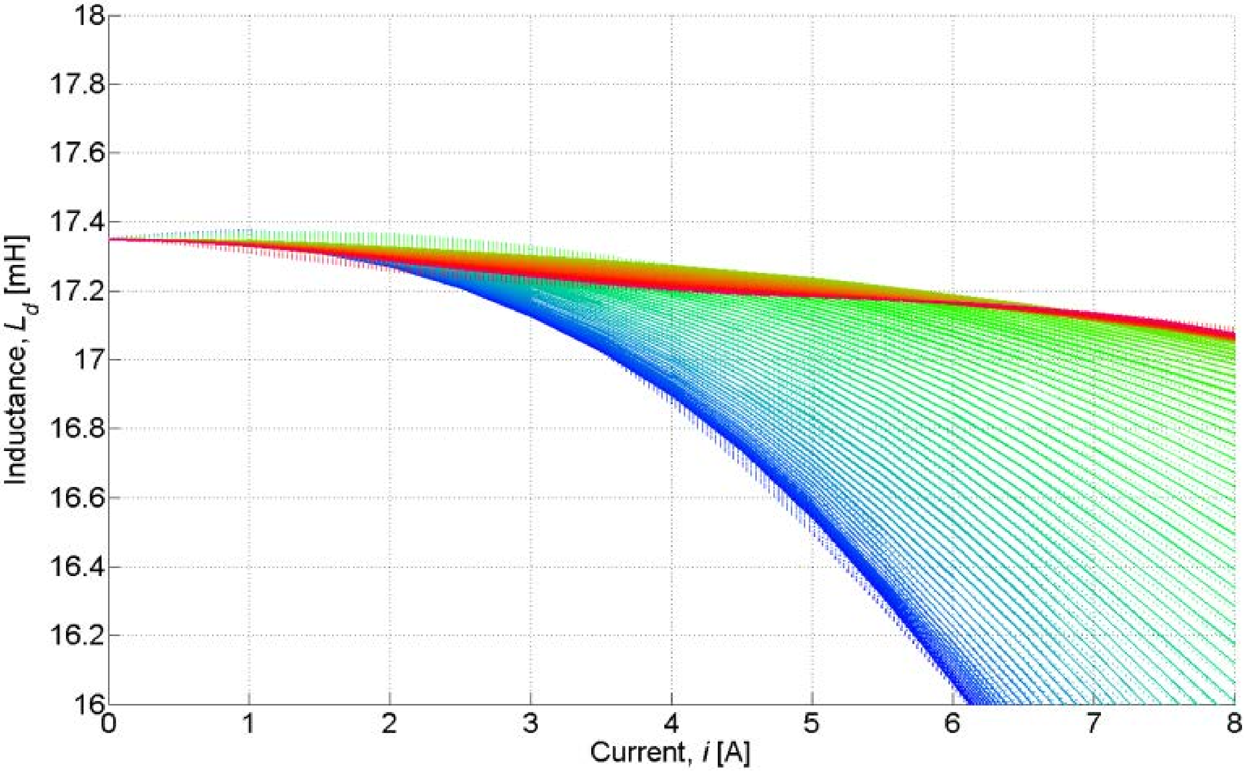

18
17.8
17.6
17.4
17.2
17
16.8
16.6
16.4
16.2
16
Inductance, L_d [mH]
0
1
2
3
4
5
6
7
8
Current, i [A]

(b)

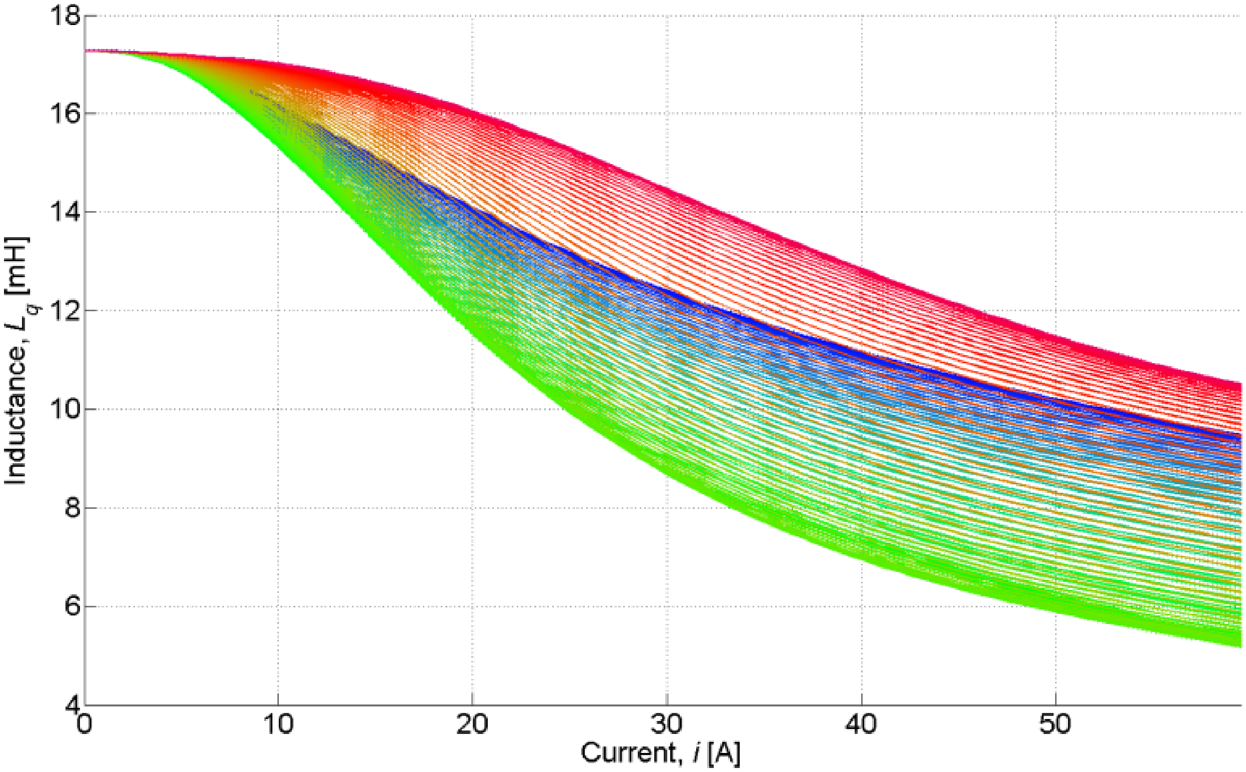

(c)

Figure 32. Fits with 7-k values for (a) L_d, (b) L_d zoomed in, and (c) L_q. The original data is shown with solid curves, and the fitted data is shown with dashed curves, where each color corresponds to a unique torque angle. Note that the slight disparity seen in Figure 31 near the peak of L_d is far less here.

Fitting along torque angle

With the direct and quadrature inductance curves along current fitted by both 5-k and 7-k rational functions, the varying k values must be correlated to the torque angle, ϕ. Because of the widely differing shapes of these k value curves over torque angle, polynomial functions are used:

$$k_n = \sum_{p=0}^{P-1} g_{p,n}\phi^p \,, \tag{40}$$

where n is the enumeration of the k value from 1 to N (5 or 7), $g_{p,n}$ is a polynomial coefficient, p is the degree of a monomial term, and P is the number of polynomials. It is appropriate to use polynomials here because ϕ is bounded by 0 and π (from π to 2π is a mirror image), so we need not be concerned about divergence beyond the region of fitting. In matrix form, (40) is

$$[k_1\, k_2 \cdots k_N] = [1\, \phi \cdots \phi^{P-1}] \times \underline{\underline{g}} \tag{41}$$

where $\underline{\underline{g}}$ is a matrix of $g_{p,n}$ values, P by N. Figure 33 and Figure 34 show two examples of the variation of k values over torque angle and their 12th-order polynomial fits.

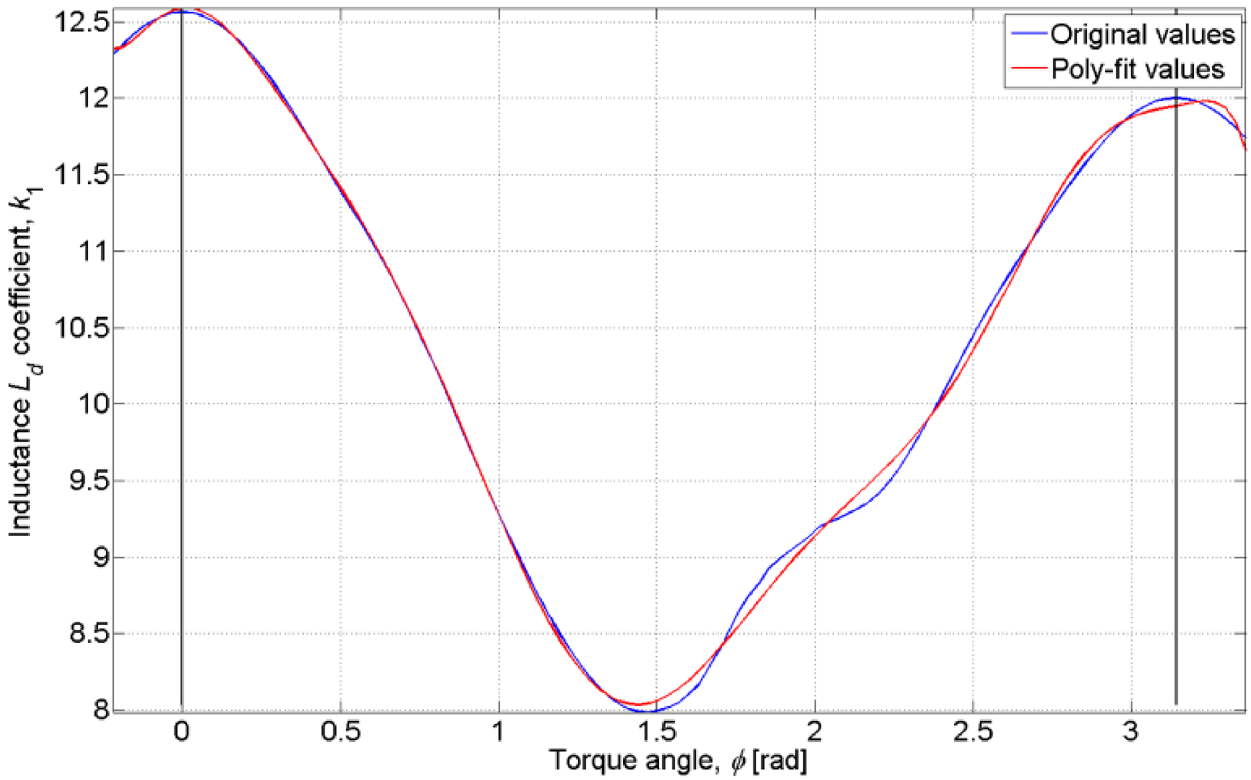

Figure 33. Original k_1 values over torque angle (blue) for 5-k rational function fit to L_d with 12th-order polynomial fit (red).

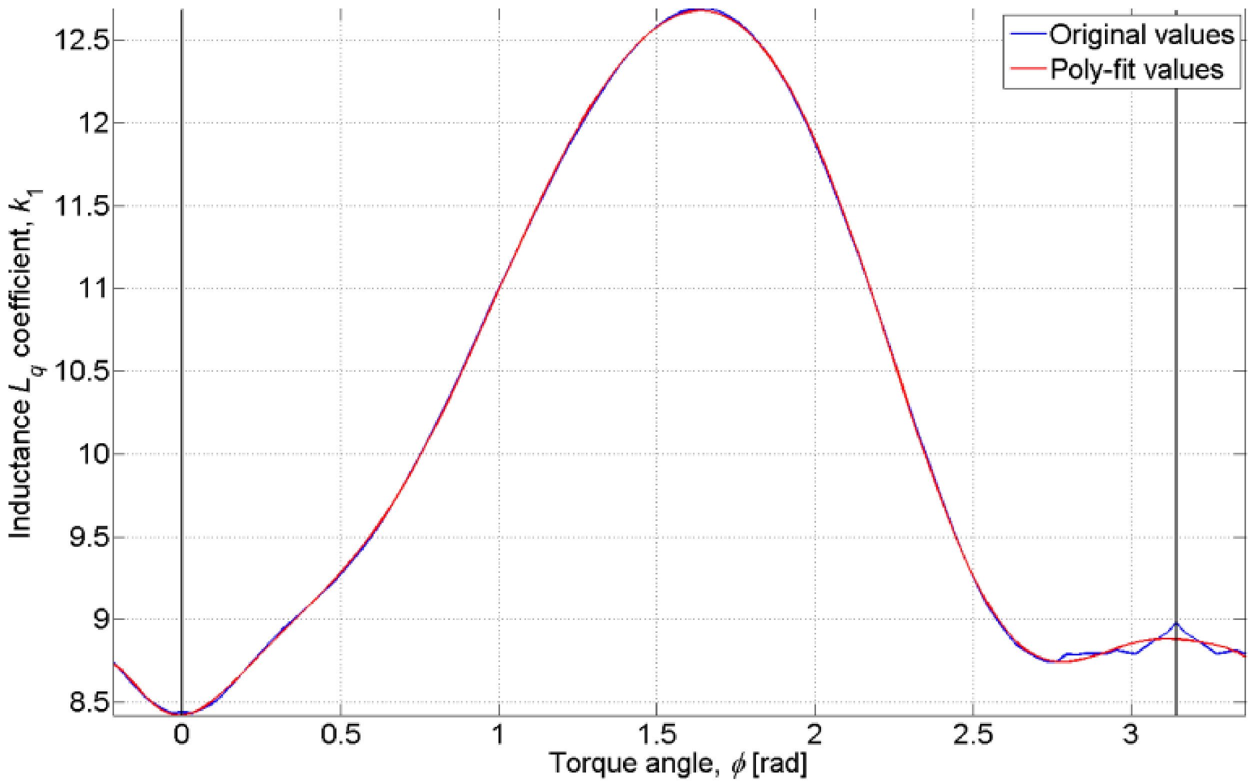

Figure 34. Original k_1 values over torque angle (blue) for 5-k rational function fit to L_q with 12th-order polynomial fit (red).

So, first, the k variables are fit to the inductance curves over current magnitude, for each torque angle. Then, each k variable is fitted by a polynomial function of torque angle. For this fitting, torque angle is bounded by 0 and π radians. In the polynomial fits, the bounds are marked by vertical black lines. Yet, there are k values and corresponding polynomial fit values extending beyond these bounds as seen in Figure 33 and Figure 34. Since inductance surfaces should be symmetrical about the direct axis, all fitting coefficients should be symmetrical about the direct axis, which corresponds to torque angles of 0 and π radians. This requires that the k curves as functions of torque angle have zero slopes at these bounds (a Neumann boundary). One method of encouraging this behavior in polynomial fitting is to mirror the tail ends of the curves. Hence, the curves shown above extend slightly beyond the stated bounds by using this mirroring technique.

A range of polynomial fitting is done for the *k* values of both 5-*k* and 7-*k* rational functions using from 6 to 22 polynomial terms (5 to 21 degree polynomials). For each *k* value fit, the normalized mean absolute difference (NMAD) is used as the error metric. The NMAD metric is here defined as

$$\begin{aligned} \mathrm{NMAD} &= \frac{1}{MR_y}\sum_{m=1}^{M}\left|y_m - \hat{y}_m\right| \\ R_y &= \max\{y, \hat{y}\} - \min\{y, \hat{y}\} \end{aligned}, \tag{42}$$

where *M* is the number of points, *m* is the index of each point, y_m is the m^{th} point reference value, $\hat{y}_m$ is the m^{th} point fitted value, and R_y is the range of the y and $\hat{y}$ sets. The net and maximum NMAD values for each set of *k* fits is calculated (Figure 35). The net NMAD is the mean of the NMADs for all the *k* values.

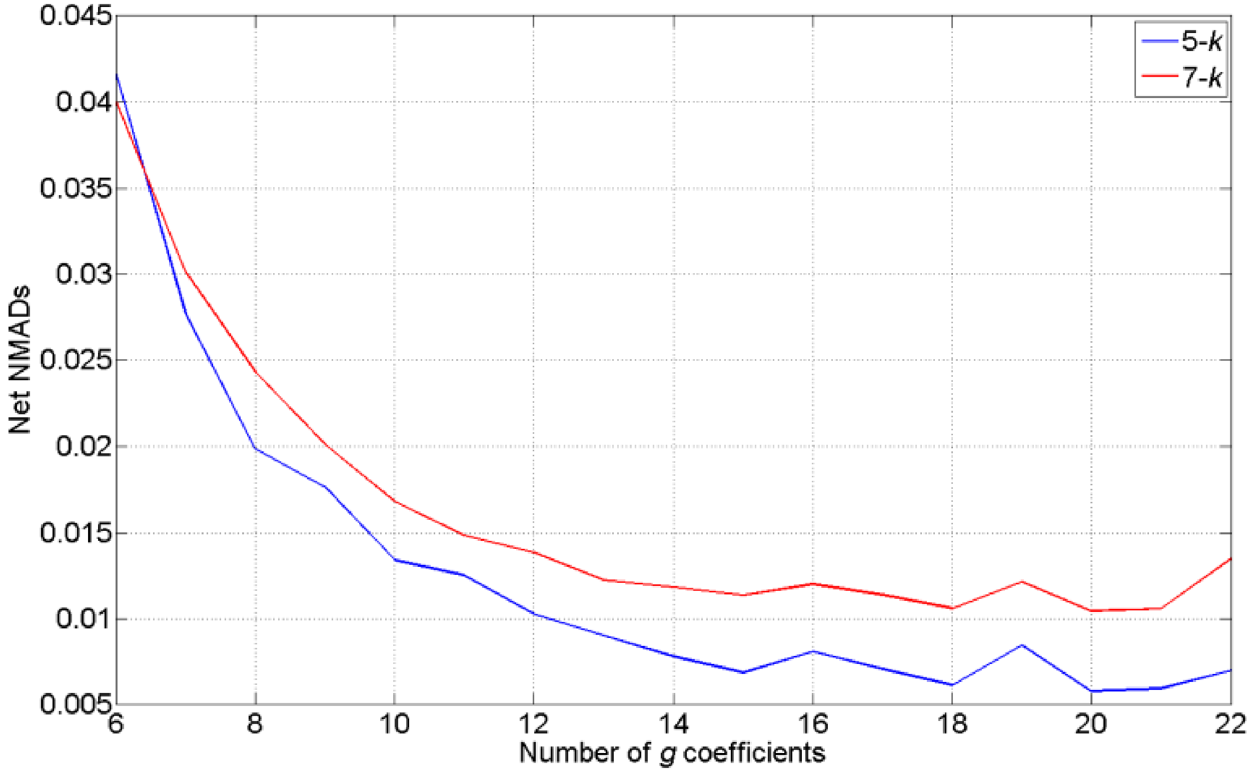
0.045
0.04
0.035
0.03
0.025
0.02
0.015
0.01
0.005
Net NMADs
6
8
10
12
14
16
18
20
22
Number of *g* coefficients
5-*k*
7-*k*

(a)

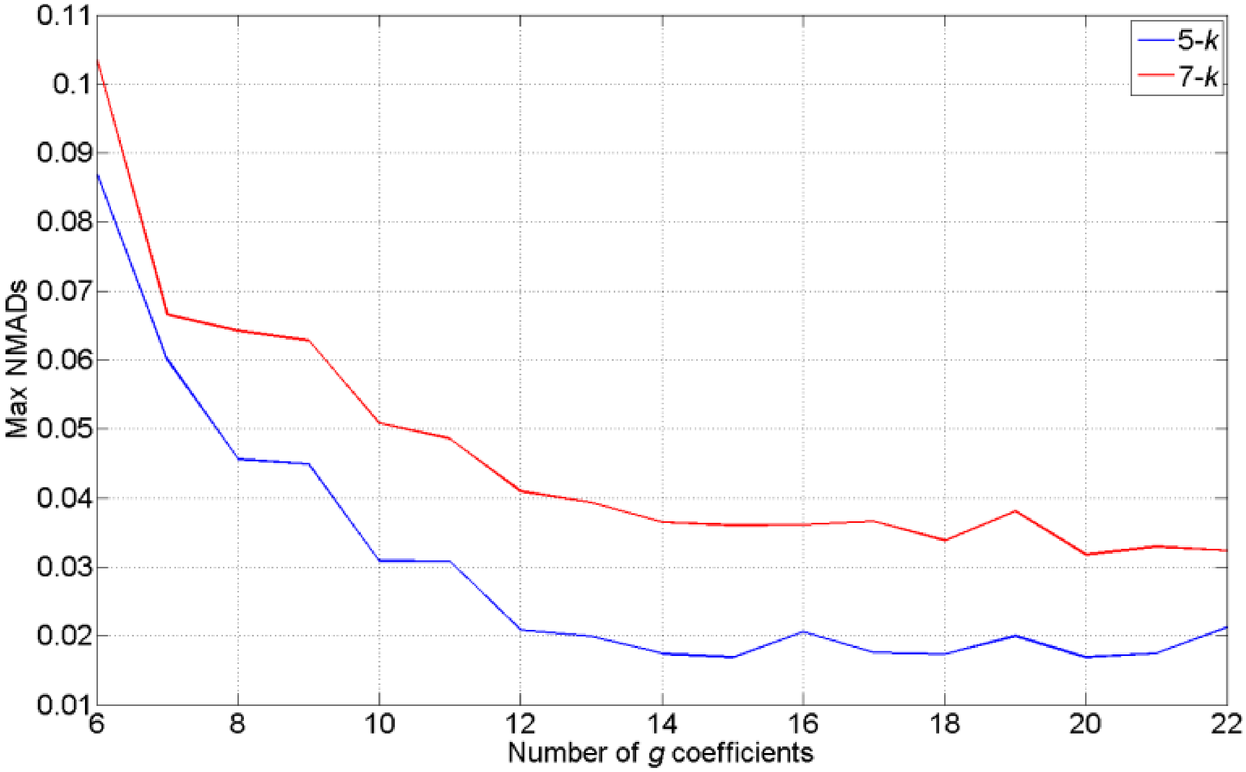

(b)

Figure 35. The (a) net and (b) max NMAD values for whole sets of *k* value fits (e.g. k_1 through k_5 for 5-*k* rational function). The 5-*k* results are shown in blue and the 7-*k* results are shown in red.

As expected, the more polynomial terms that are used the better the fit to the *k* values. This is true up to a point, past which the functions become over-defined. From Figure 35, the optimum number of *g* coefficients for the polynomial fits seems to be around 10 to 16 (9 to 15 degree polynomials) for both 5-*k* and 7-*k* rational functions.

At this point, the inductance fitting as a whole must be compared to the real inductance surfaces and their current derivatives.

Evaluating the fitting

In applying a fitting formula, not only do the inductances need to match, but so do the current derivatives. This means the inductance surfaces must match very well. To test the fitting, current magnitudes and torque angles are randomly chosen. At each corresponding point (i_d,i_q), the smoothed inductance tables are linearly interpolated to provide the reference values. This is an accurate but slow table lookup method. On a particular machine running MATLAB 2012a, this takes about 1.1721 s to process a large matrix of arbitrarily chosen points. A simplified lookup is also tested whereby the nearest neighbor is used and no interpolation is done. This rounding method takes about 0.776 s for the whole matrix of points. The optimum fitting (12th-degree polynomials for the 5-*k* rational function) with the technique demonstrated in this paper takes only 0.467 s. This is 66% faster than the nearest-neighbor table lookup method and 2.5 times faster than the linear interpolation method (Figure 36).

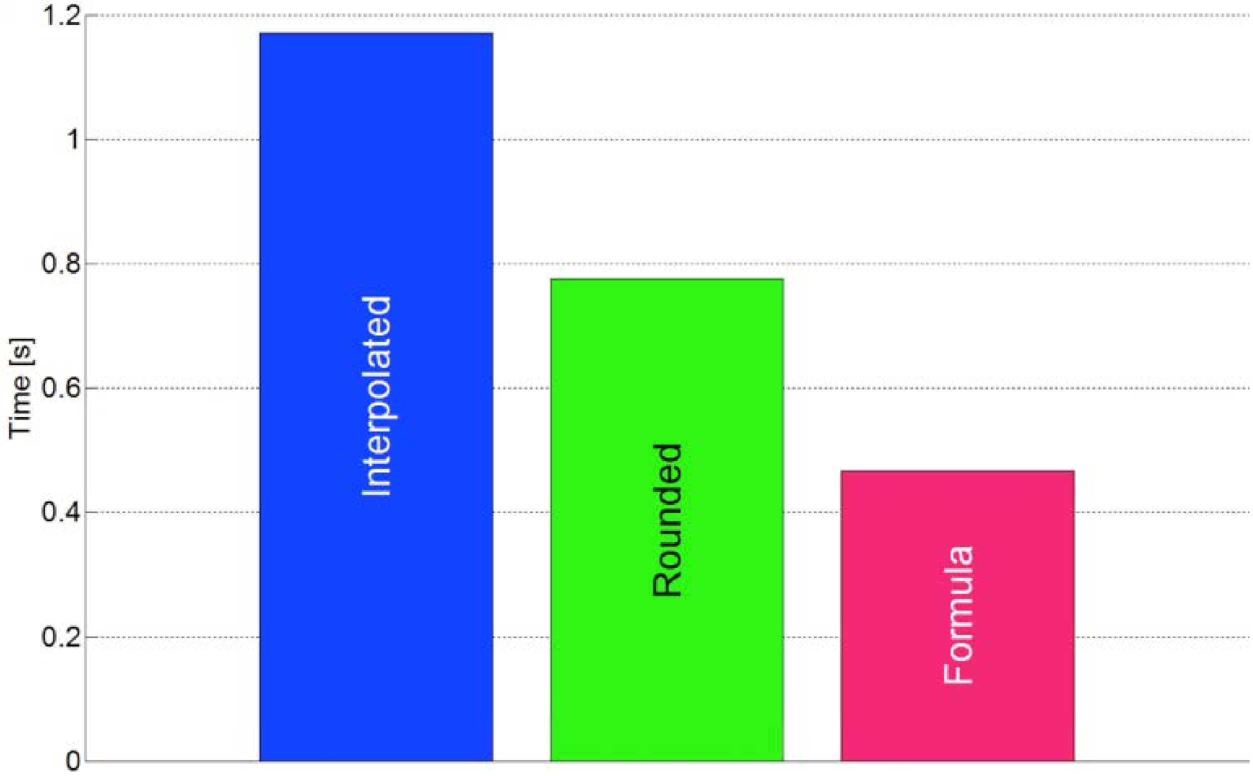

Figure 36. The time required for the three methods to calculate inductances and their current derivatives. The formula method is faster.

Besides being fast, the formula is quite accurate. In some cases the average error from the formula is less than the error induced by rounding a 0.5 A variation in current during nearest-neighbor table lookup. A comparison of the NMADs of the overall formula fits versus the rounding lookup is shown in Figure 37. The inductances L_d and L_q match the original profiles quite well. Their derivatives differ a bit more but their errors are still quite small.

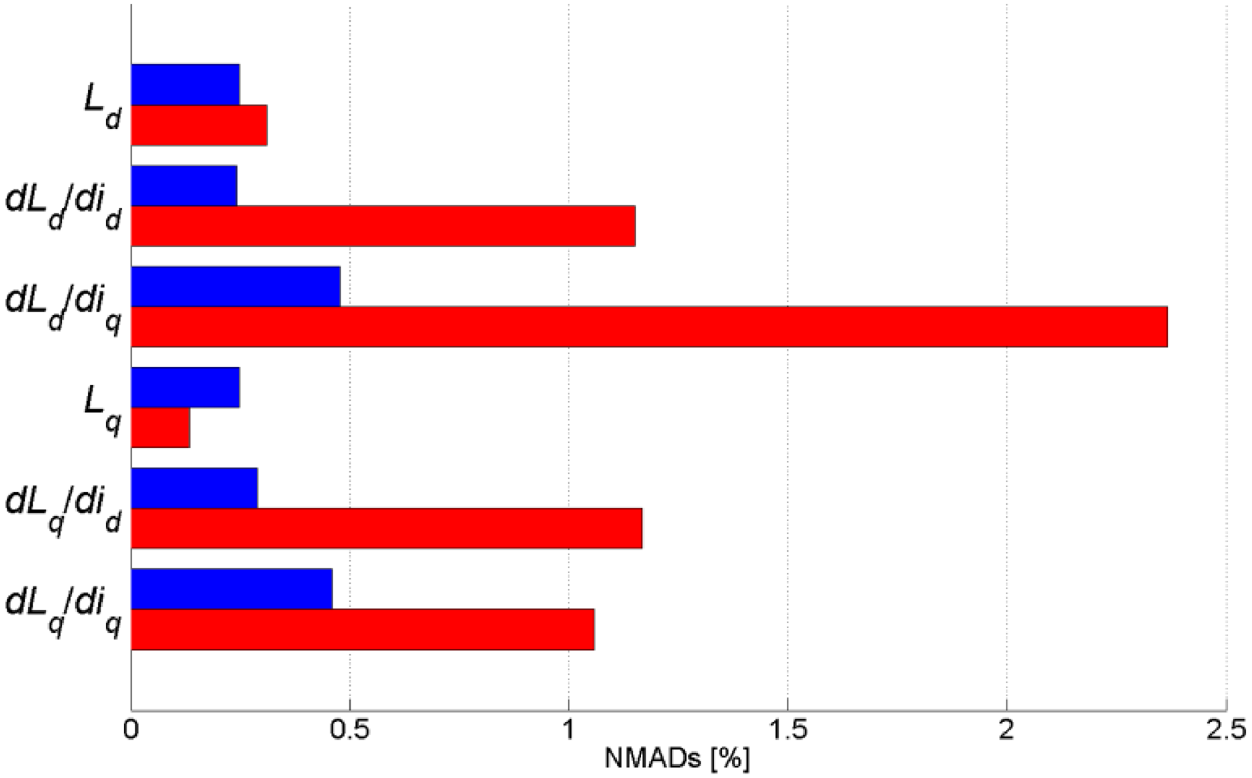

Figure 37. Comparison of NMADs for rounding lookup (blue) and formula fit (red). The percentages were obtained by simply multiplying the NMAD values by 100%. Note the lower error for the formula fit to L_q.

These results are for a 12th-order polynomial fit for the 5-*k* rational function. This uses (40) to get the *k* values and (38) to get the inductance values from the *k* values. A comparison of some of the results is shown in Figure 38 and Figure 39.

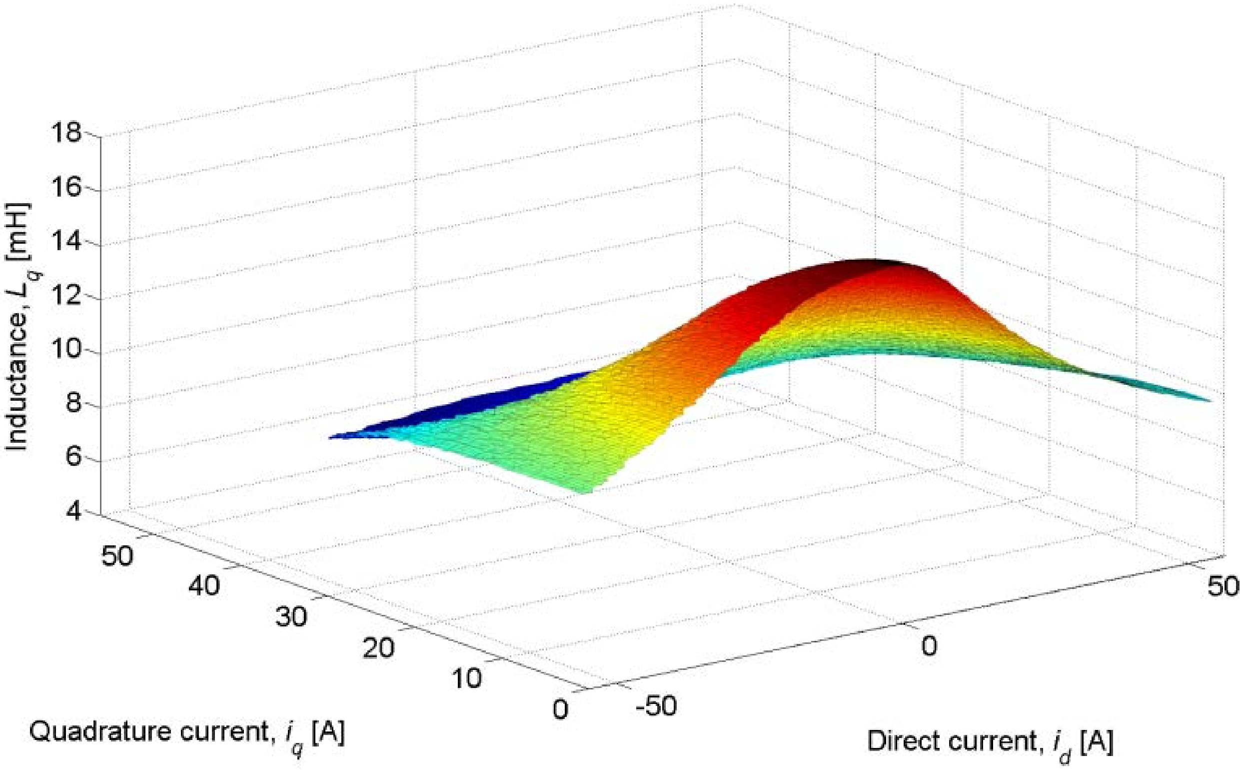

Inductance, L_q [mH]
18
16
14
12
10
8
6
4
Quadrature current, i_q [A]
50
40
30
20
10
0
Direct current, i_d [A]
-50
0
50

(a)

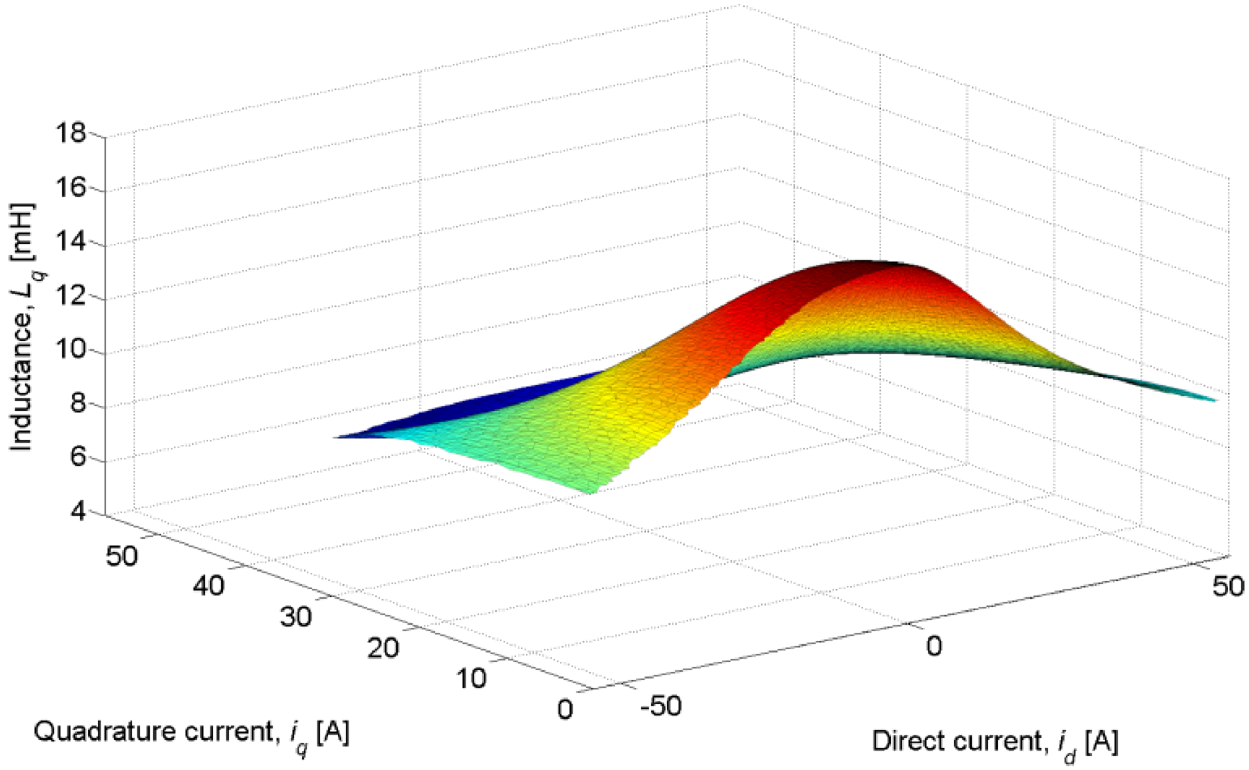

(b)

Figure 38. Inductance L_q by (a) rounding lookup and by (b) formula fit.

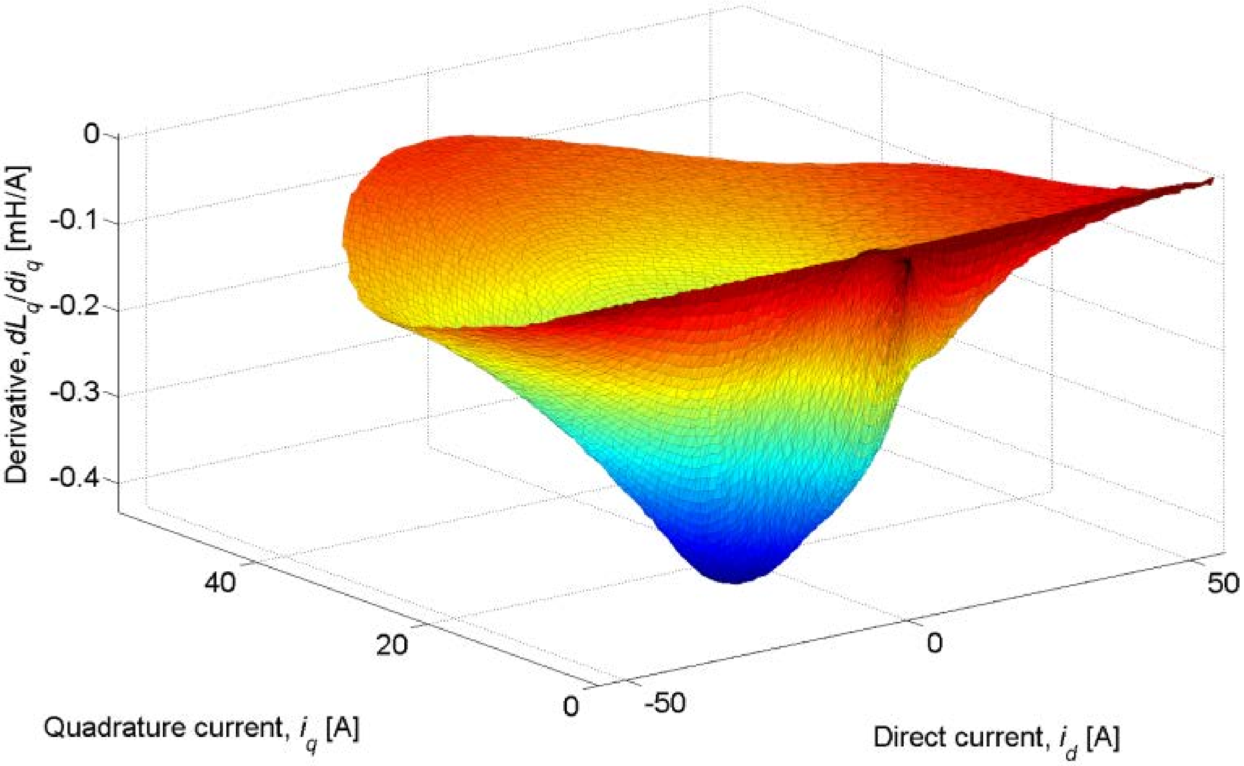
0
-0.1
-0.2
-0.3
-0.4
Derivative, dL_q/di_q [mH/A]
40
20
0
Quadrature current, i_q [A]
-50
0
50
Direct current, i_d [A]

(a)

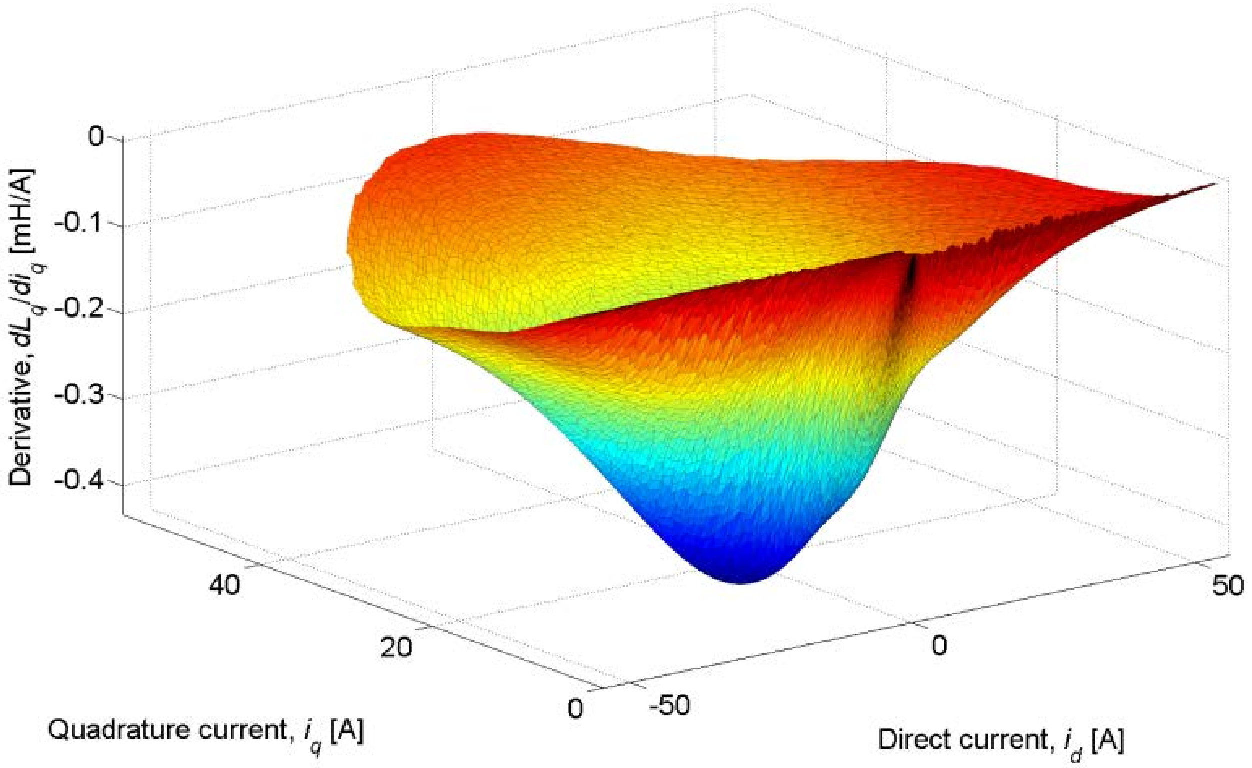

(b)

Figure 39. Inductance derivative dL_q/di_q by (a) rounding lookup and by (b) formula fit.

But to show the inherent smoothness from using a formula rather than a lookup table, a comparison is shown in Figure 40 of the absolute differences relative to interpolation lookup of rounding lookup and formula fitting.

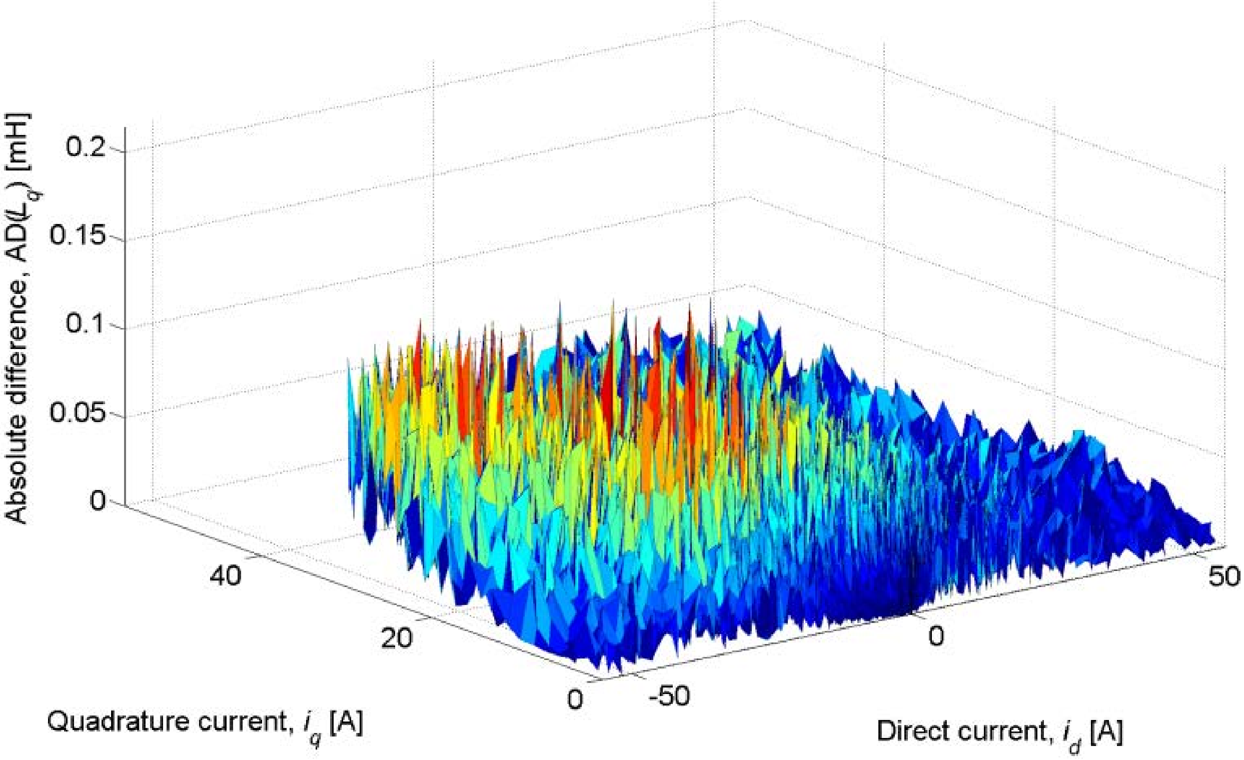
Absolute difference, AD(L_q) [mH]
0.2
0.15
0.1
0.05
0
40
20
0
-50
0
50
Quadrature current, i_q [A]
Direct current, i_d [A]

(a)

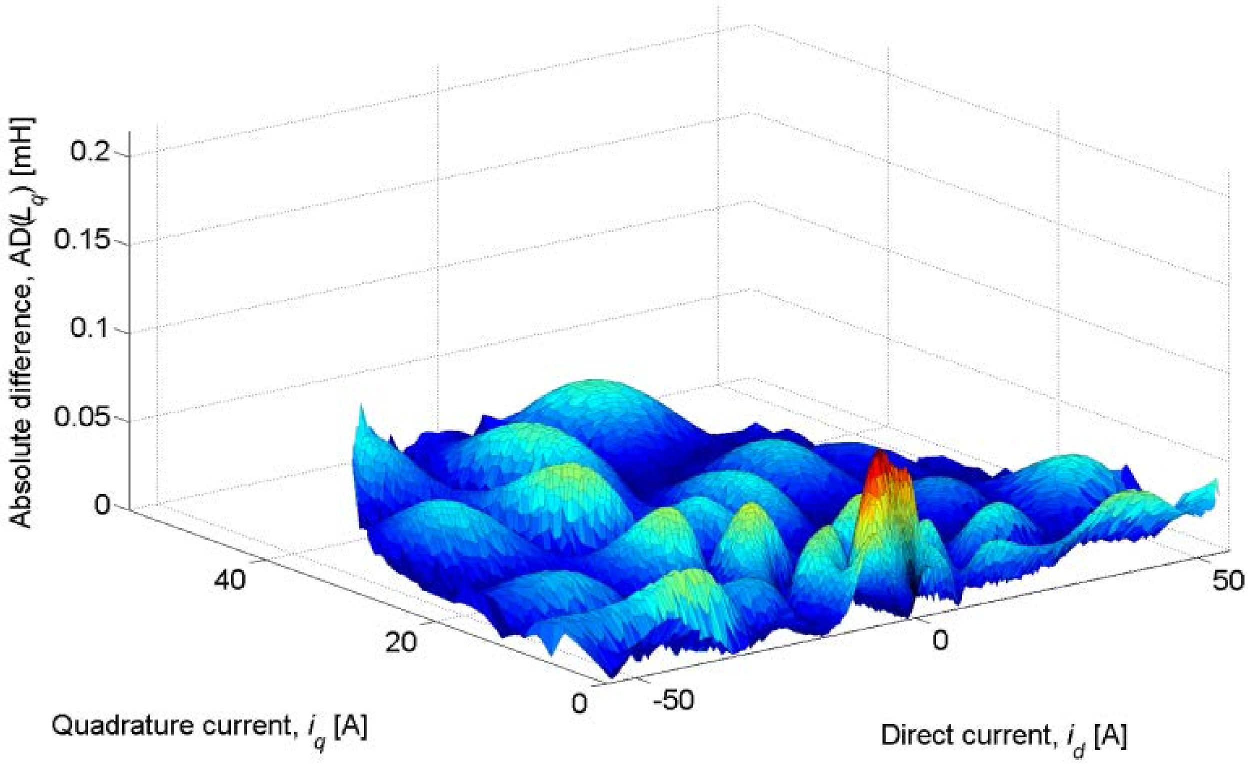

(b)

Figure 40. Absolute difference relative to interpolation lookup of (a) rounding lookup and (b) formula fitting for L_q.

A consequence of using a formula rather than a lookup table is the smoothness of the results, which can be of concern in numerical stability.

To choose the 12th-degree polynomial fit and 5-*k* rational function, a suite of tests is run for various degrees of polynomials for both the 5-*k* and the 7-*k* rational functions. In each case, the mean of the NMADs (Figure 37) of all six properties together is calculated (the net NMAD). Figure 41 shows the results.

Clearly, the 13-coefficient (12th-degree polynomial), 5-*k* fit is a very reasonable choice. Past 22 coefficients, the errors for both fits begin to skyrocket or become numerically unstable.

The 7-*k* fit does not ever show better overall performance; and past 13 coefficients, the 5-*k* fit does not show much improvement. The validity of weighting the six properties equally in calculating the net NMADs could be argued, but it is difficult to say whether the inductance or its derivatives have a greater effect on the behavior of an electric motor since this depends on how the motor is run.

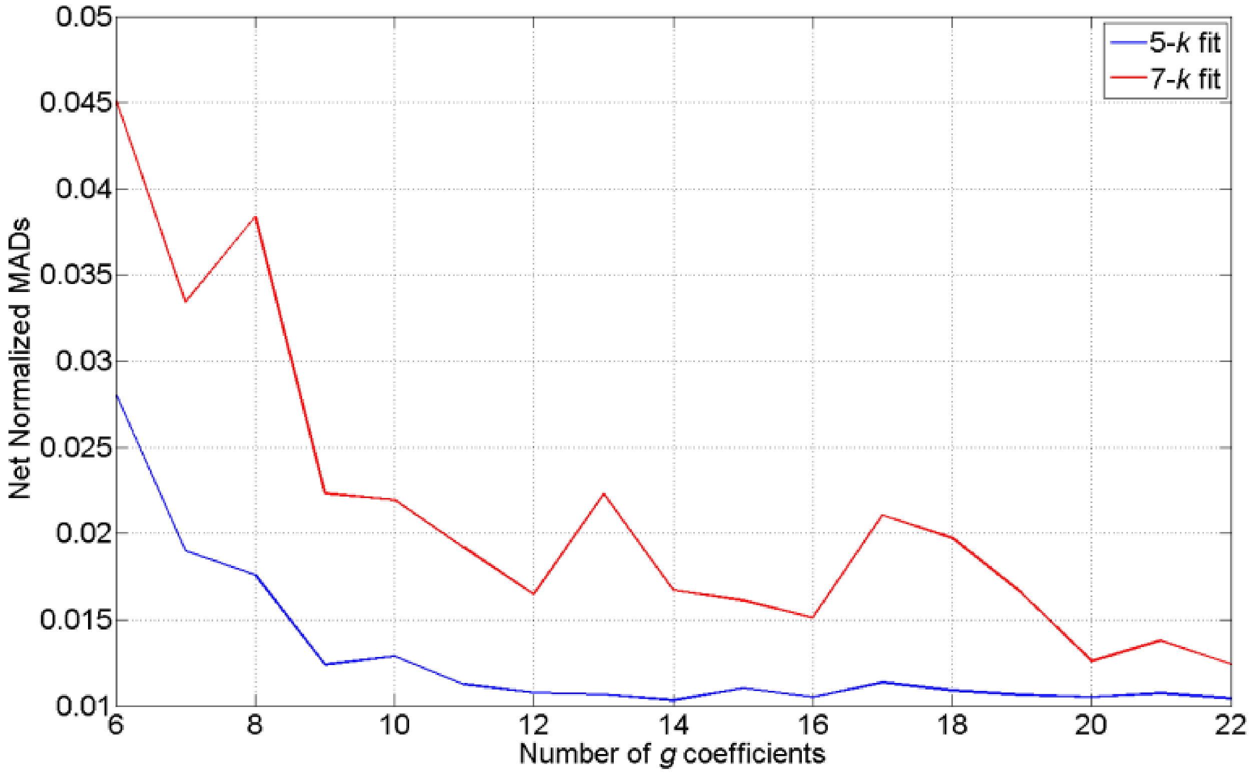

Figure 41. The mean over the six properties of the six normalized mean absolute differences for the 5-*k* fit (blue) and the 7-*k* fit (red).

The simulation times for these tests are also shown (Figure 42). Using a 7-*k* fit takes about as long as a 5-*k* fit with two additional polynomial coefficients.

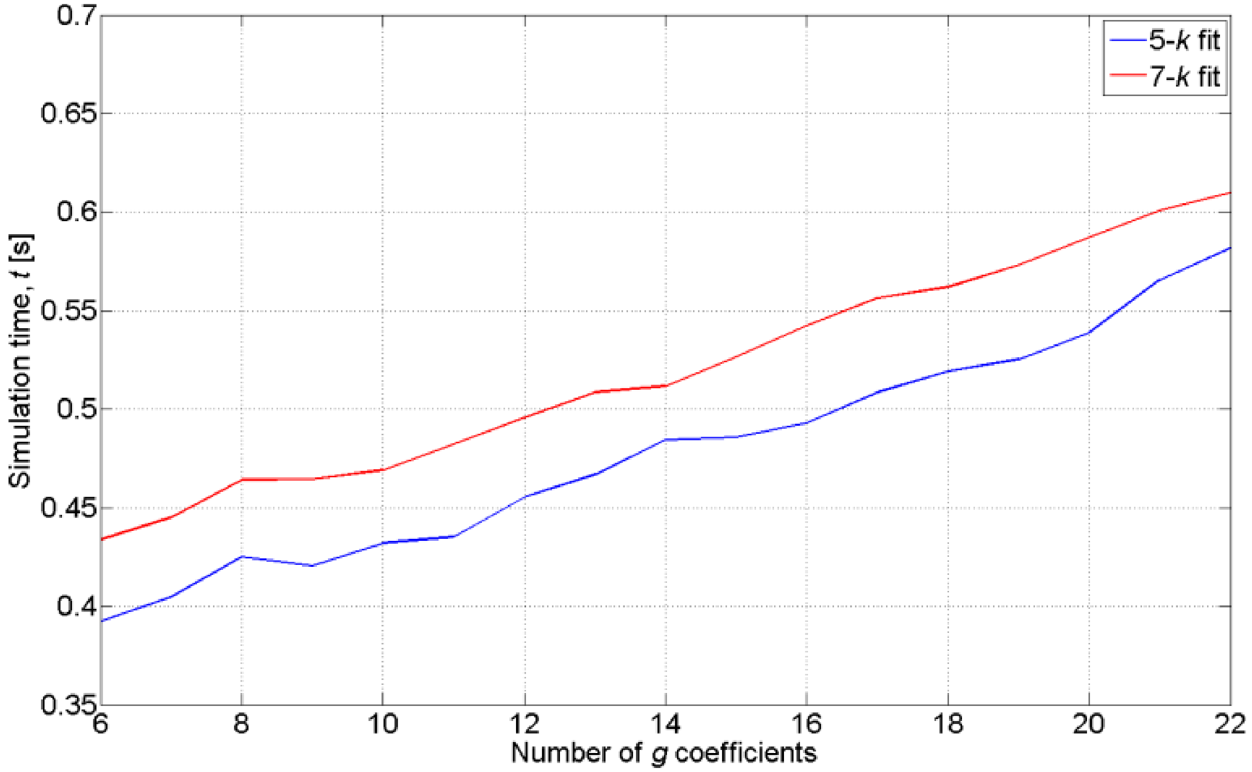

Figure 42. Simulation time for 5-*k* (blue) and 7-*k* (red) tests. These results are for single test runs at each setting. Averaging over many test runs, these curves would straighten.

Comparison with Other Methods

The formula used in this paper is similar to a rational function used in [33]; however, there the degree is lower and the coefficients are not parameterized. Also, that formula is a function of only one current and, therefore, cannot include cross-coupling effects. Some modeling, such as in [34], focuses purely on the rotor angle effects on inductance. In [35], a model is proposed where the stator phase inductances are modeled as functions of only the corresponding phase current and a Fourier series of the rotor angle. The paper does suggest measurements being taken to get inductances as functions of current magnitude, rotor angle, and torque angle; however, no model for this is presented. In [36], a similar model is developed. It uses a single cosine function with current polynomials for the coefficient and bias. The polynomials are functions of only the corresponding phase current. In [37], a model that focuses on modeling the inductances in their ABC-reference frame is shown. The downsides to this approach are that control code is often already in the DQ0 reference frame and that this type of formula is based on Fourier series compositions, which are computationally slow.

These models may be especially helpful where the rotor angle is of interest, such as in rotor angle estimation. However, the cross-coupling effects of the phase currents are of much greater relevance to full, PM motor simulation models, such as found in [38]. The model shown in (38) and (39) captures these cross-coupling effects.

In [39], another formula is proposed to model the DQ flux linkages, λ_d and λ_q, as functions of the DQ currents, thereby including cross-coupling effects. For both λ_d and λ_q, the formula has the form

$$\begin{aligned}\lambda(i_d, i_q) = {} & \left(C_1 e^{-A_1 i_q} + C_2 e^{-A_2 i_q}\right) e^{-\left(C_3 e^{-A_3 i_q} + C_4 e^{-A_4 i_q}\right) i_d} + \\ & \left(C_5 e^{-A_5 i_q} + C_6 e^{-A_6 i_q}\right) e^{-\left(C_7 e^{-A_7 i_q} + C_8 e^{-A_8 i_q}\right) i_d}\end{aligned}, \tag{43}$$

where the C and A coefficients are tuning parameters. Though the flux linkages used for the research in our paper are undoubtedly different than those used in [39], the characteristic shapes should be the same. That paper demonstrates fits over current magnitudes up to 2 amperes; and for that range, the fits to the inductances presented here are indeed very good with NMAD values less than 0.5%. However, at higher current values, (43) does not seem to be able to capture the saturation of the flux linkages as well as (38) does when used to calculate flux linkages. In Figure 43 the reference λ_d is shown; and, in Figure 44, a comparison of these two methods is shown.

No other published work has been found to use a technique similar to the one presented in this paper.

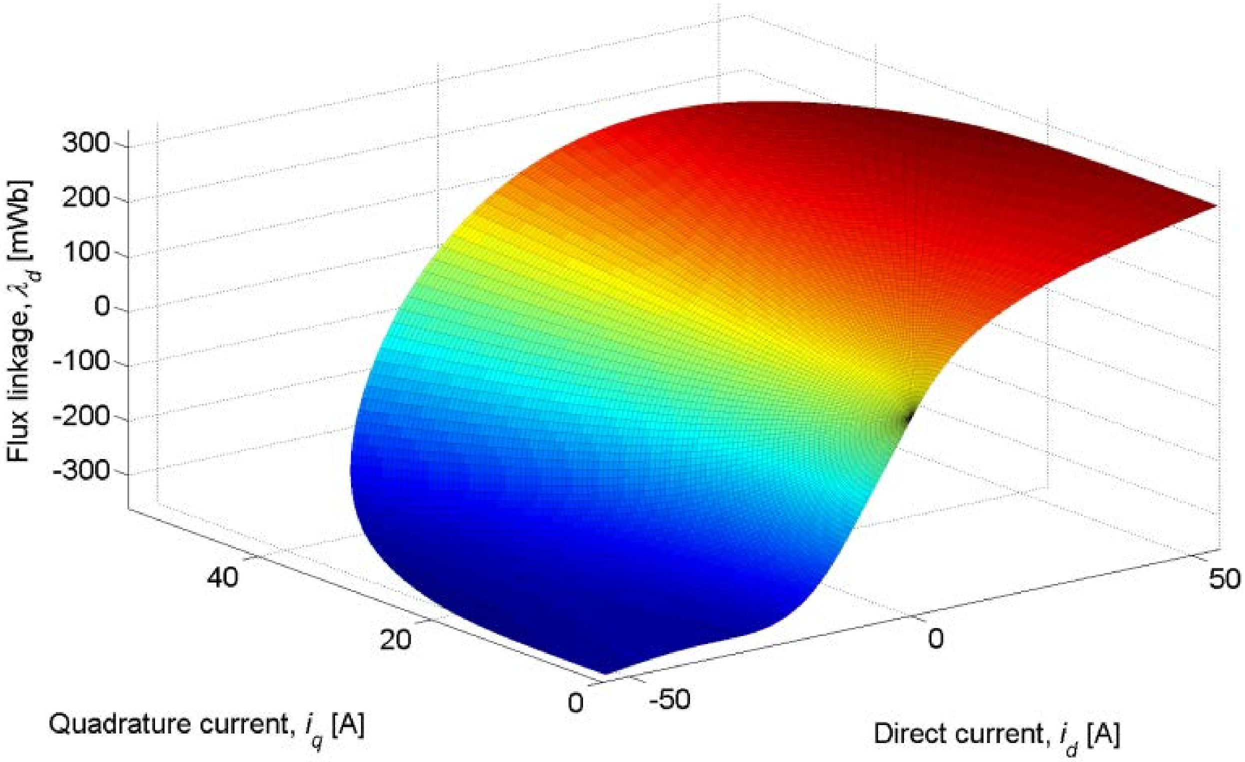

Figure 43. For current magnitudes up to 55 A, the reference λ_d flux linkage.

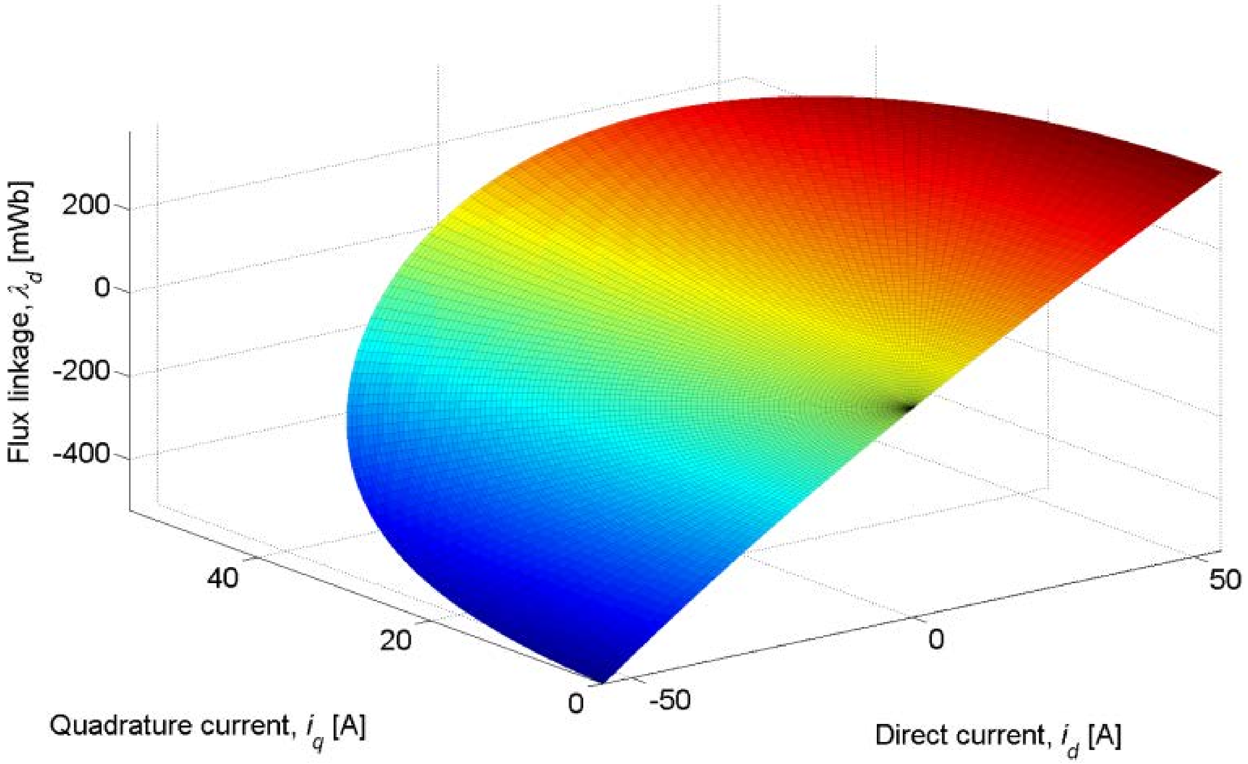

Flux linkage, λ_d [mWb]
200
0
-200
-400
Quadrature current, i_q [A]
40
20
0
-50
0
50
Direct current, i_d [A]

(a)

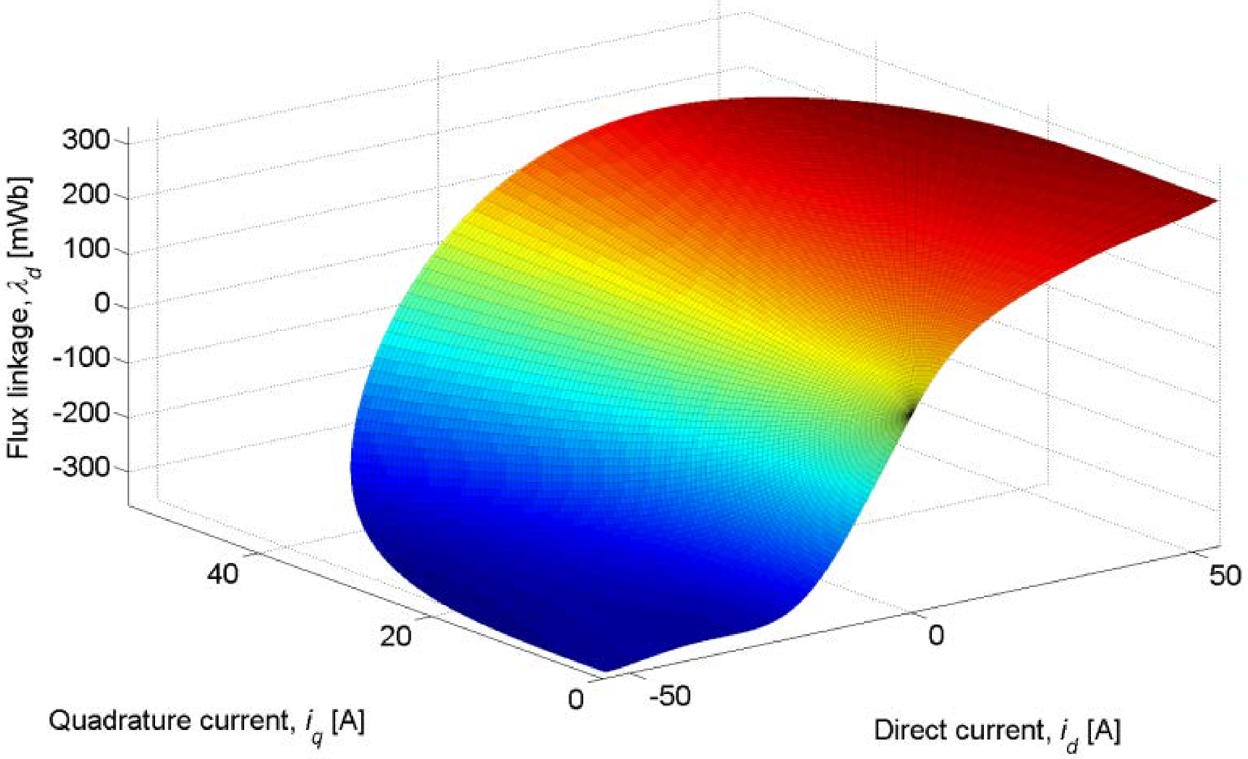

(b)

Figure 44. For current magnitudes up to 55 A, the direct flux linkage λ_d (top) using (43) and (bottom) using (38).

Simplified Model

It is possible to significantly simplify the model presented in this work, at a slight cost to accuracy. The same form of rational function shown in (38) can be used but with the current magnitude replaced by the D and Q currents. The formula for both L_d and L_q becomes

$$L(i_d, i_q) = \frac{k_1}{1 + k_2 \left| i_d - k_3 \right|^{k_4} + k_5 \left| i_q \right|^{k_6}} + k_7 \tag{44}$$

where these k values are scalars. The k_3 value provides the i_d current shift. So, to completely describe the inductances for a PM machine, only 14 coefficients would be required. The NMAD values for L_d and L_q using this formula are 2.3% and 2.8%, respectively. Figure 45 shows the inductances from using this formula, and Figure 46 shows the absolute differences from the reference inductances.

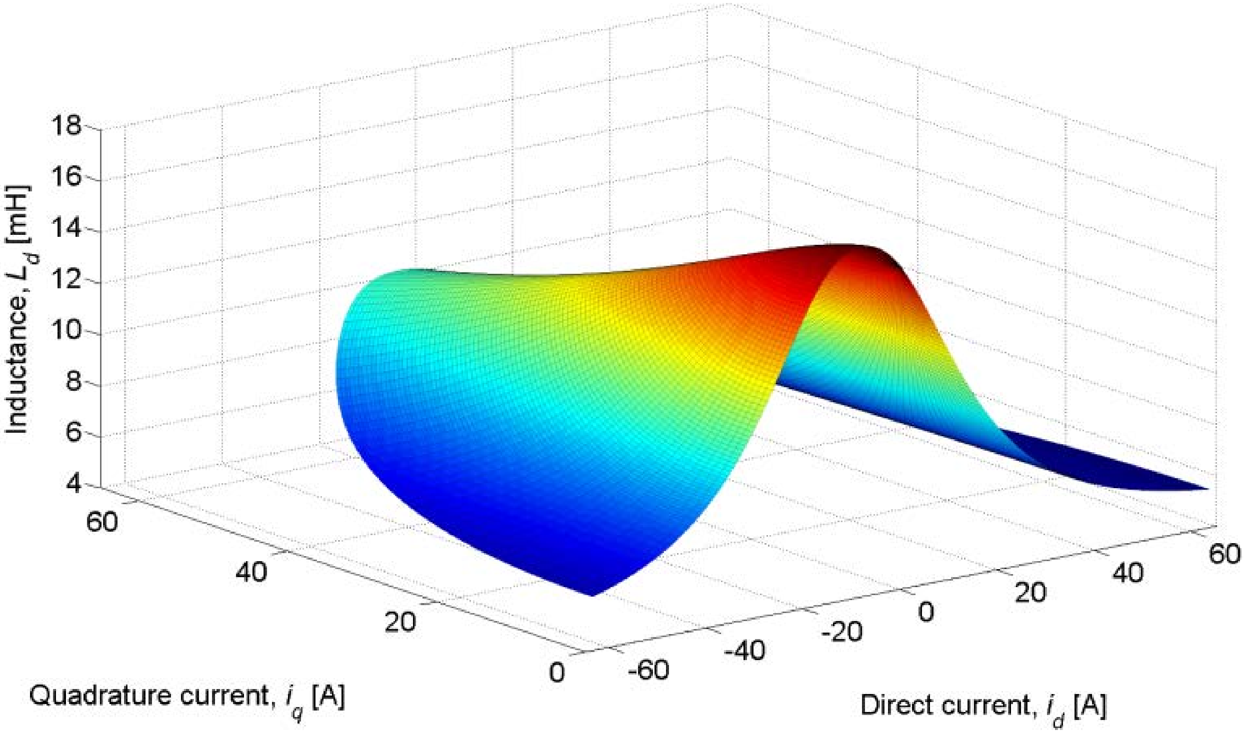

(a)

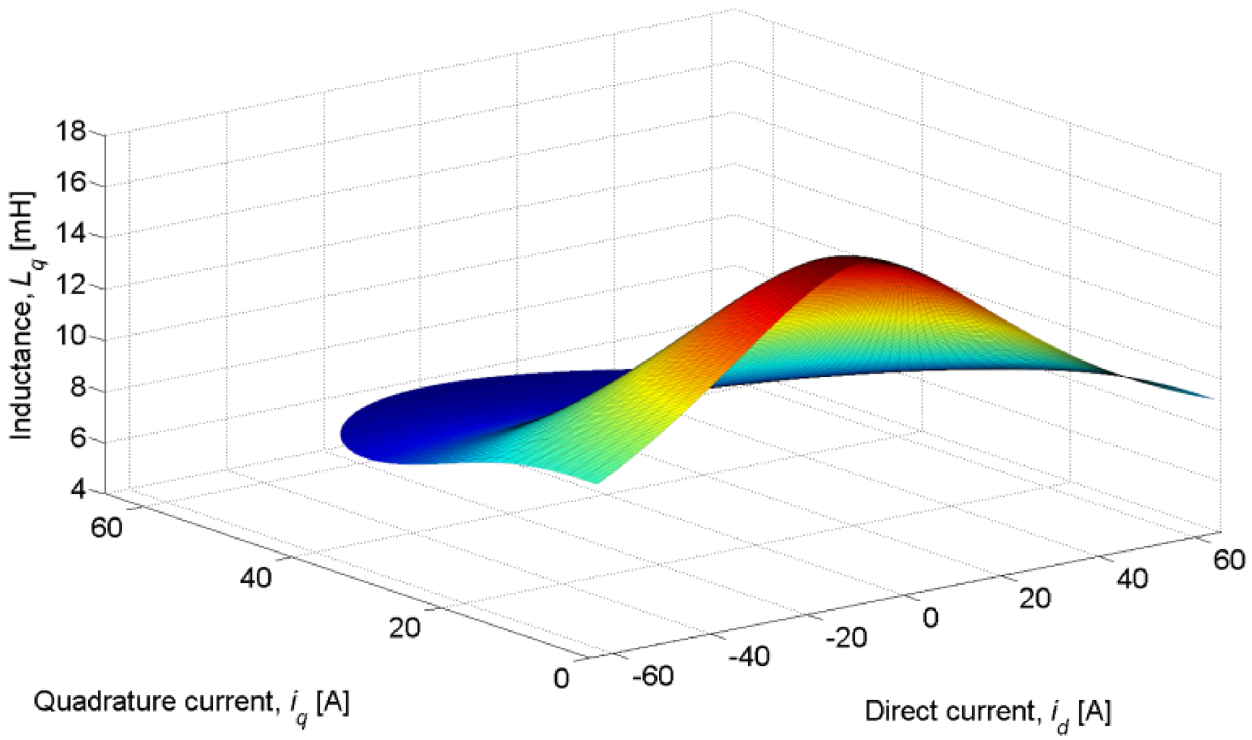

(b)

Figure 45. The (a) D and (b) Q inductances using the simplified rational function (44).

As before, as long as the coefficients are positive, singularities will never be observed. The k_3 value is excluded from this restriction. It should also be noted that the power coefficients k_4 and k_6 should be greater than 1. This will ensure that the peaks of the inductances are flat and do not show saturation even at infinitesimal currents.

This model forces the inductances to be symmetrical about the peak, so there is not as much flexibility with (44) as with (38) and (39). However, depending on the need, the greatly reduced complexity and increased computational speed may be worthwhile. For embedded systems, the real number exponents might be highly undesirable, but each real number power can be replaced with multiple whole number powers to achieve nearly the same effect at a reduced computational burden.

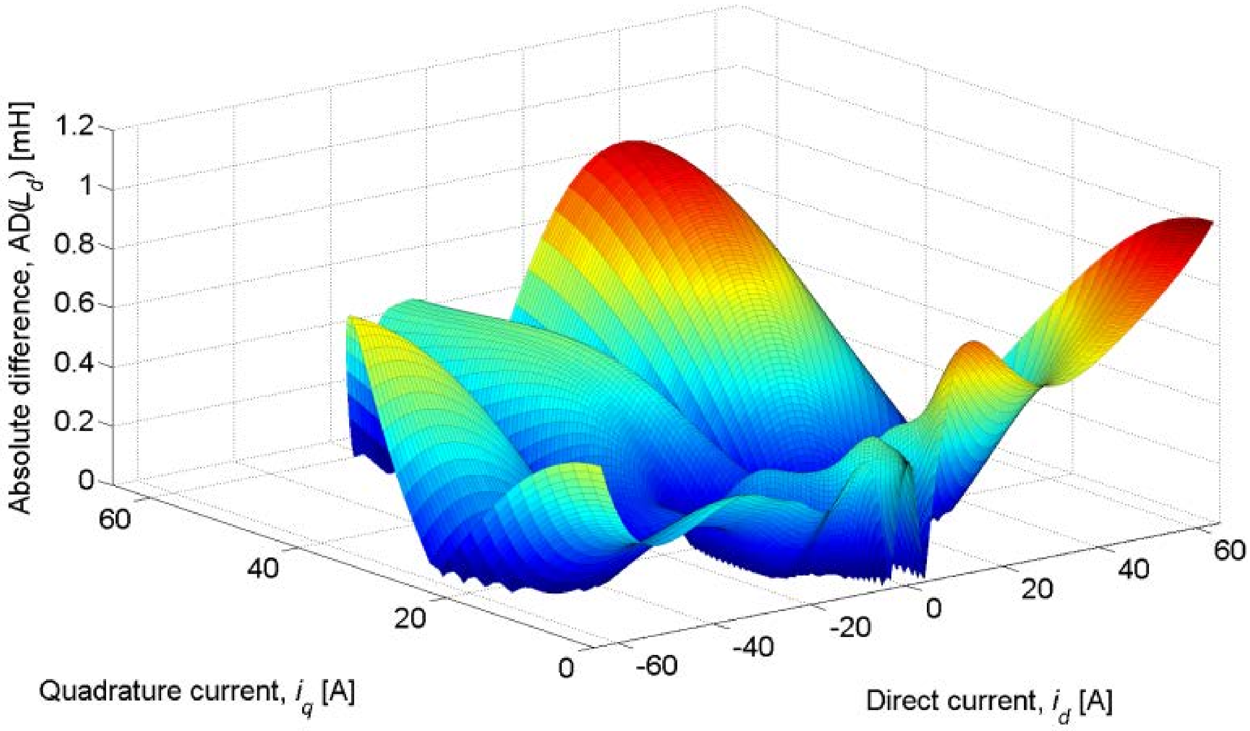

(a)

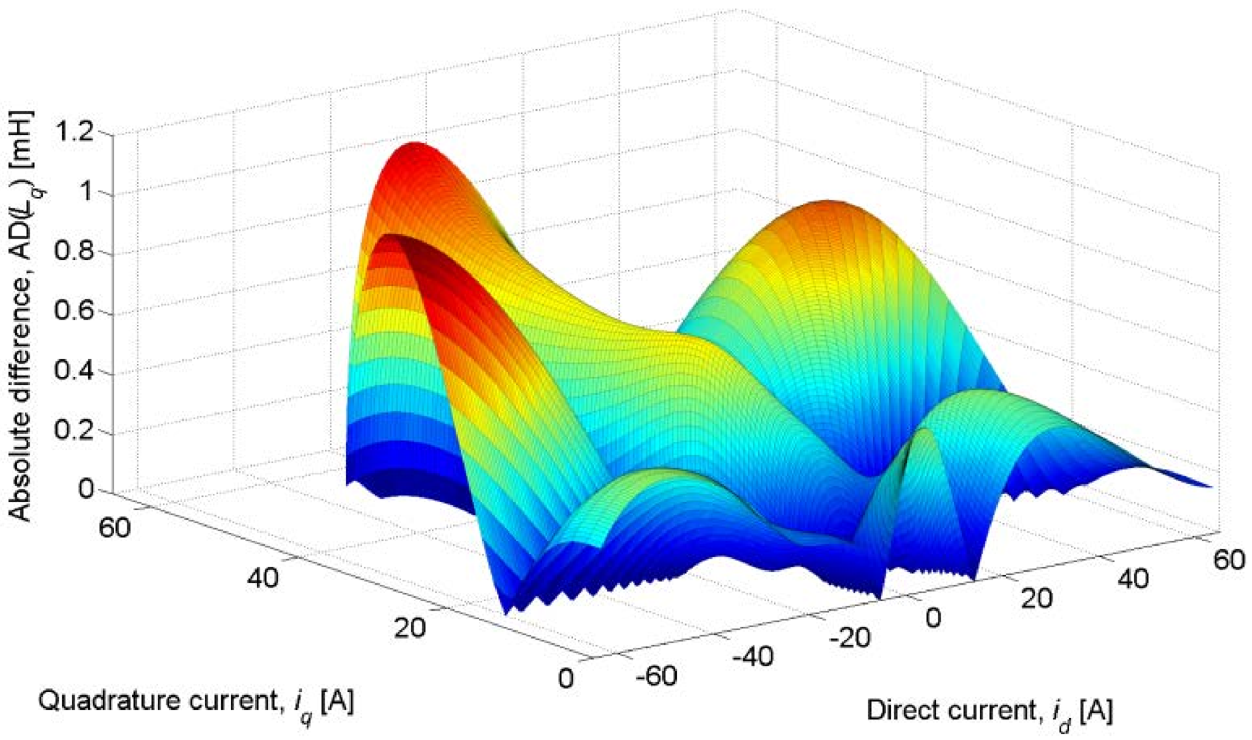

(b)

Figure 46. Absolute differences between reference and formula inductances for (a) L_d and (b) L_q.

Experimental Application and Comparison with Linear Modeling

In [38], the inductances discussed in this paper are used in the simulation of a full EMA model which was evaluated using physical experiments on an EMA under active loading. This model was also used to compare linear (constant-valued) inductances and nonlinear (formula-based) inductances.

Because of the simulated control algorithm used, the desired stroke is followed the same regardless of which type of inductances are used (Figure 47).

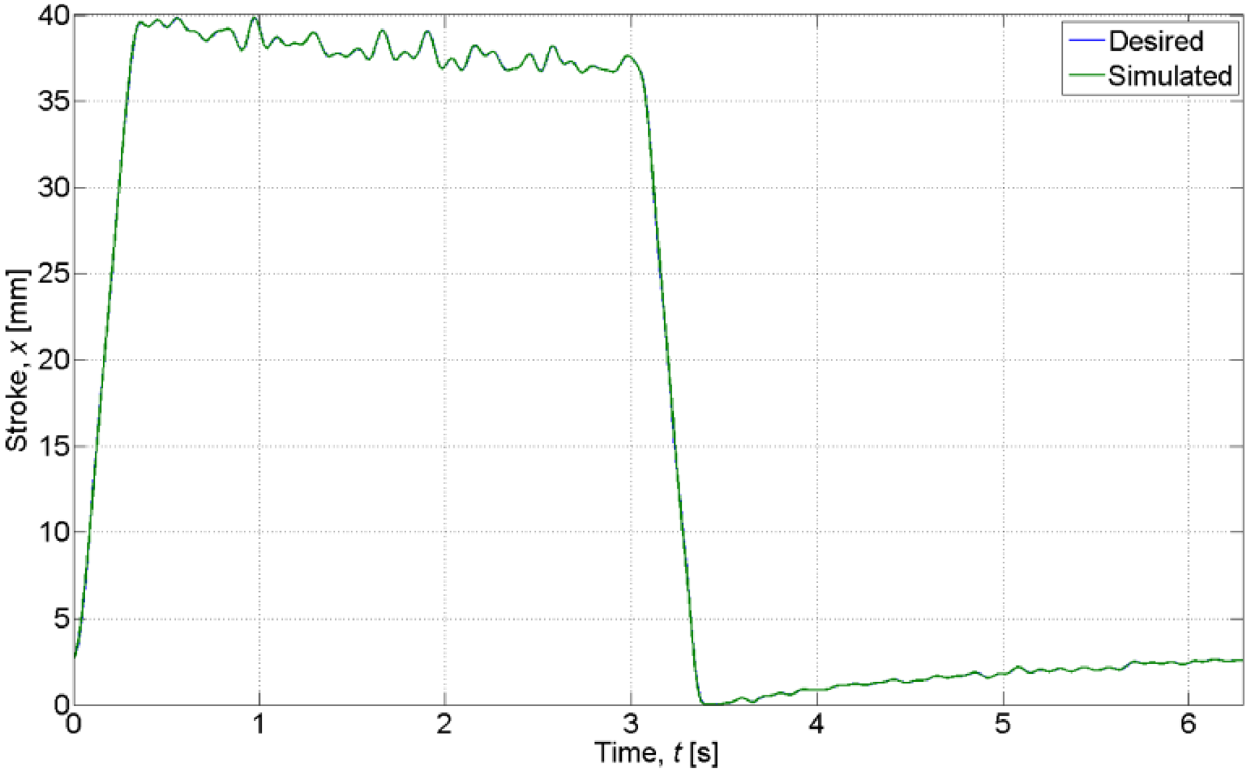

Figure 47. Desired stroke profile (blue) and simulated stroke profile (green). Note that the desired stroke profile was followed fairly well by the control algorithm. The desired stroke profile was taken from a physical experiment with an EMA under active loading.

The power loss, P_{Cu}, in the windings due to the electrical resistance of the copper is calculated for both cases, linear and nonlinear (Figure 48). This power is integrated to get the cumulative energy, E_{Cu}, dissipated as heat in the windings (Figure 49). And, this heat manifested itself as temperature rises in the machine Figure 21.

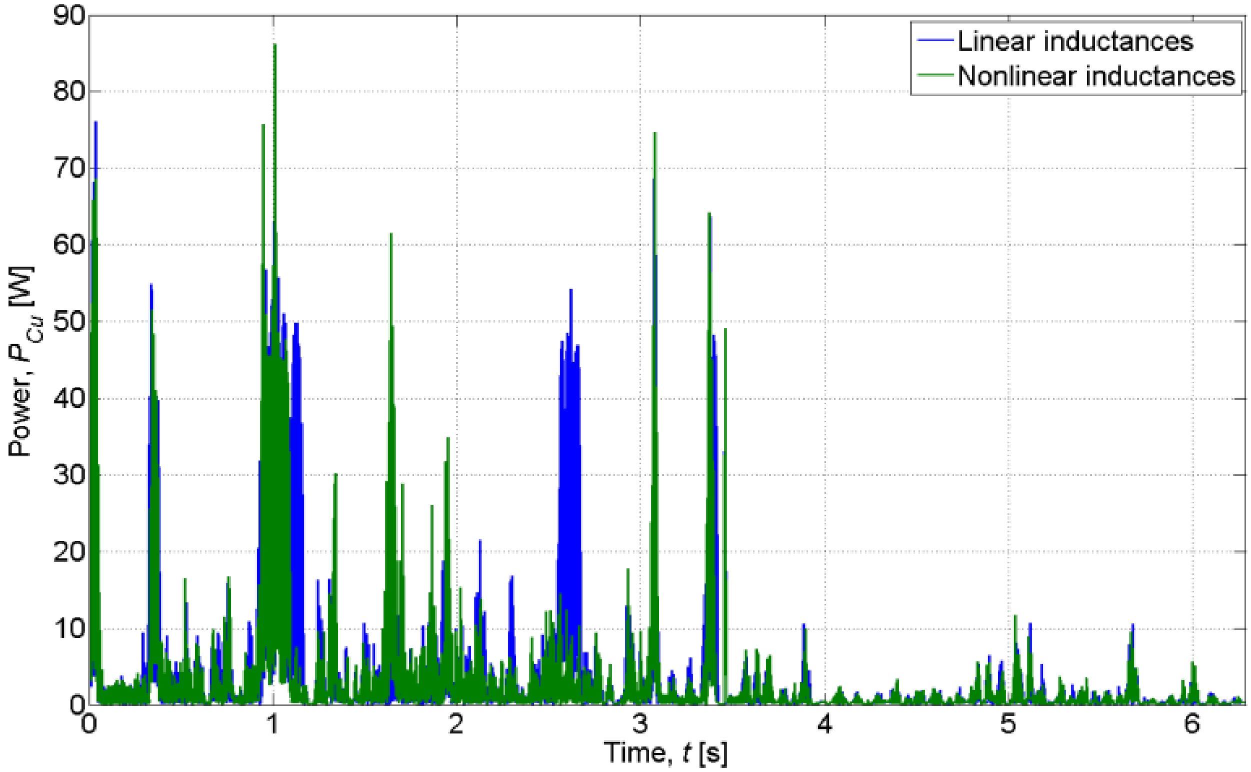

Figure 48. Simulated power losses in copper windings using linear inductances (blue) and nonlinear inductances (green).

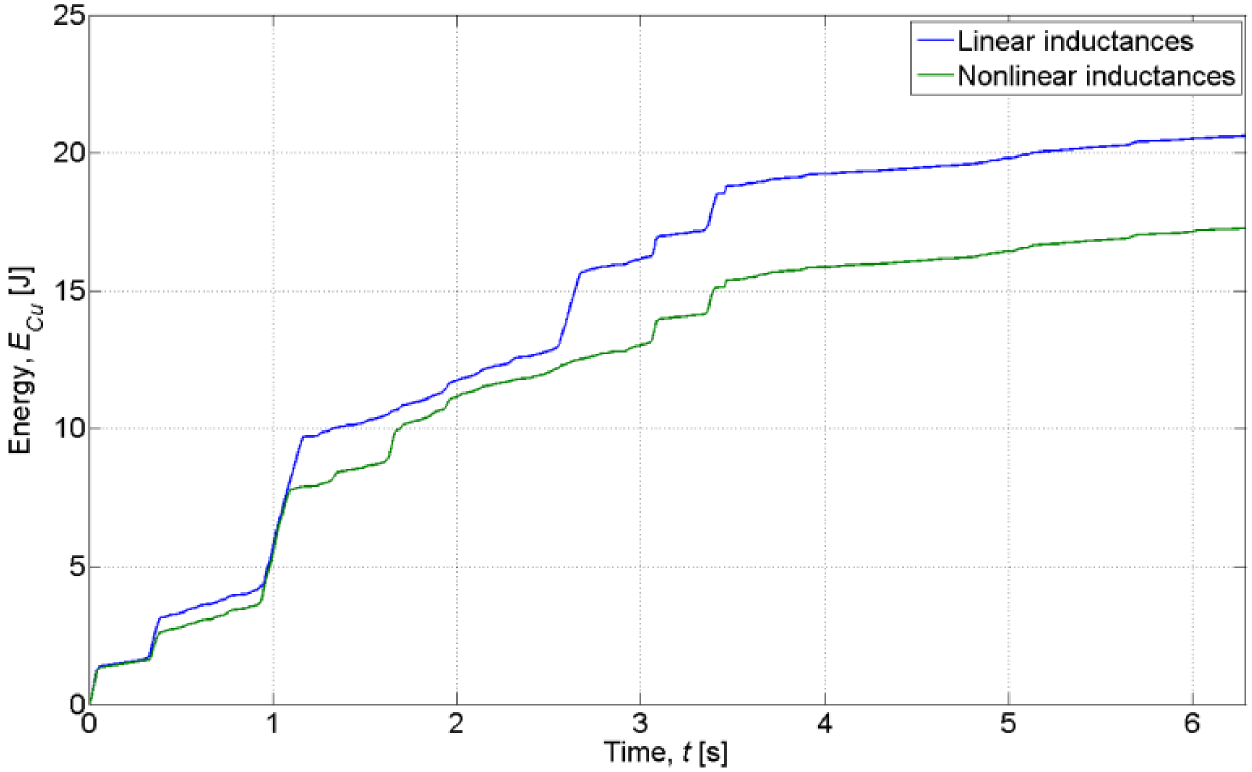

Figure 49. Simulated energy losses in copper windings using linear inductances (blue) and nonlinear inductances (green).

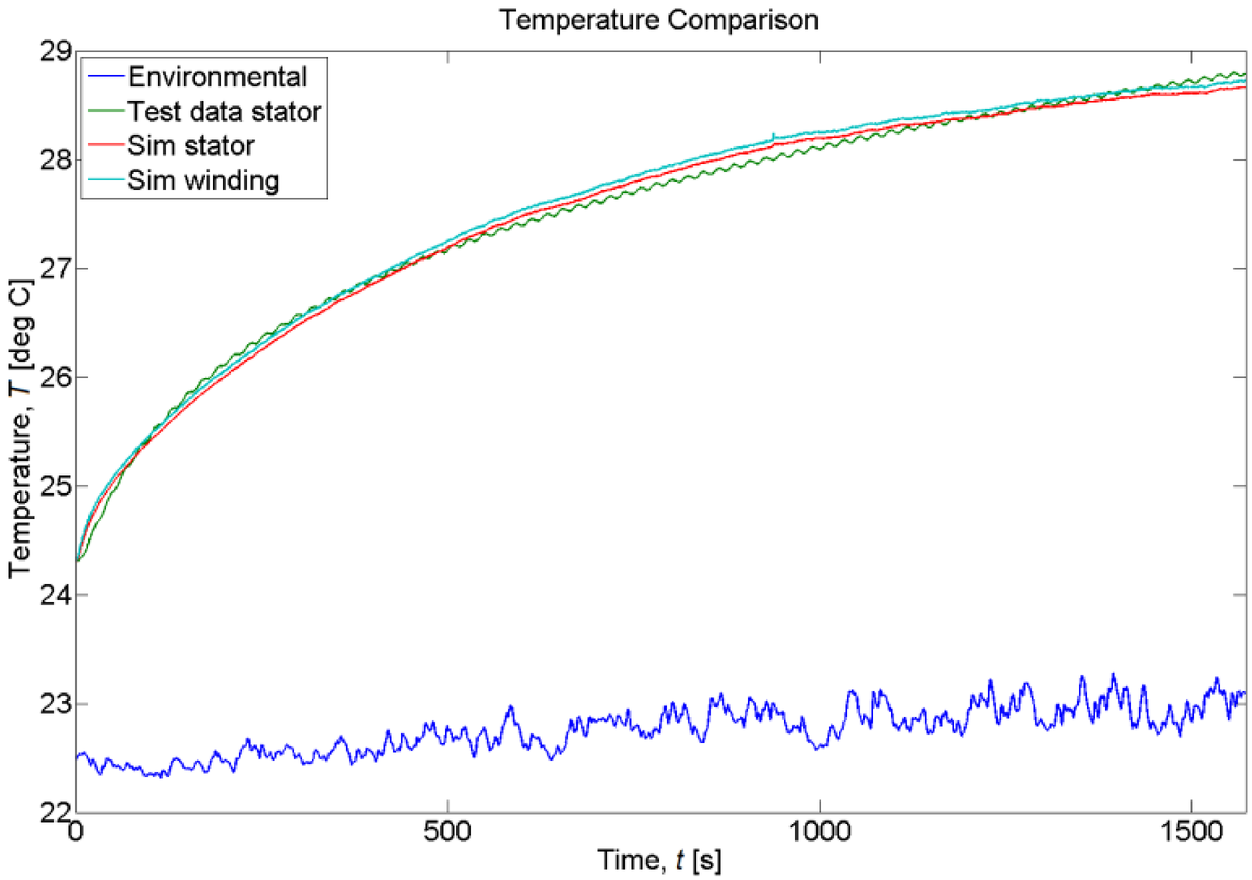

Figure 50. Temperature comparison for a half-hour run showing environmental temperature (blue), experimentally measured temperature of stator (green), simulated temperature of stator (red), and the simulated temperature of the windings (cyan). The nodal temperatures in the EMA's electric motor are simulated using the nonlinear inductances. These temperatures, which are functions of the energy losses, match very well.

Looking at the final values of cumulative energy losses, there is a 19% difference after only 6 seconds. So, by using linear inductances, the energy dissipation is significantly overestimated. Note that these cumulative energy loss curves diverge somewhat unpredictably over time. Though their reasons for differing are hidden in the complexities of motor control and other dynamics, it is likely that their difference will grow with time. This comparison highlights the dramatically significant difference that using nonlinear inductances can make.

Conclusion

Nonlinear, lumped-element modeling of PM motors in EMAs has value in moving towards all-electric aircraft. At the core of this modeling are the nonlinear inductances. This paper shows an approach to fitting the nonlinear inductances with a rational function because it extrapolates well and captures the overall characteristics of the inductances. The variations in the coefficients of the rational function are modeled by polynomial functions because of their flexibility and computational efficiency.

Depending on the machine, the formula performs faster than even simple nearest-neighbor table lookup and gives fairly accurate results. And this formula includes the cross-coupling effects that many other methods do not.

Finally, using nonlinear inductances instead of linear inductances can result in a noticeable difference in energy dissipation in the motor. So, while nonlinear inductances are somewhat more complex to use, they can give dramatically different results.

CHAPTER FOUR: NONLINEAR, TRANSIENT MODEL OF SYNCHRONOUS GENERATOR

Introduction

Up to this point, the nonlinear inductances of the PM motor have been carefully modeled and the EMA as a whole has also been modeled. The seminal concern is the successful integration of the EMA into the aircraft electrical system and its thermal performance. In this chapter, a generator is modeled by itself, which is the other major component in the total system.

The operation of the generator is similar in basic concept to the motor. However, some key features distinguish it. First, the generator is not a permanent magnet machine. The field flux is supplied by a field current. The primary purpose of the field current is simply to create a link for the mechanical power flowing into the generator to create electrical power on the armature windings. Second, the generator is multi-stage: it is multiple synchronous machine (SM) generators in series. The generator presented here has two stages: a 6-pole exciter and a 10-pole main. Its basic layout is shown in Figure 51.

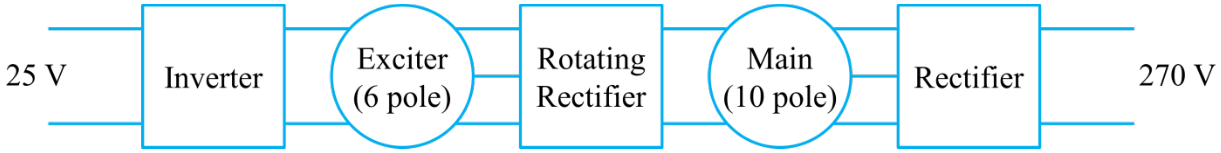

Figure 51. Overall layout of generator. The exciter is a 6-pole SM without dampers and the main is a 10-pole SM with dampers.

This work details the methods used in modeling the flux linkages of the generator, the modeling of the rectifiers, the method taking the full derivative of flux linkages, and the results of the simulation. Because speed of simulation is so important, circuit models such as Simulink's

SimPower Systems were avoided in favor of explicit mathematical models, which do tend to run significantly faster. The symbols used throughout this work are listed in Table 7.

Table 7. Simulation States and Parameters

Symbol	Name	Units
t	Time	s
θ_m	Rotor angle	rad
ω_m	Rotor speed	rad/s
θ_s	Synchronous flux angle	rad
ω_s	Synchronous flux speed	rad/s
τ	Torque	N m
u	Voltage	V
i	Current	A
λ	Flux linkage	Wb
L	Inductance	H
u_{DC}	Inverter DC bus voltage	V
i_{net}	Rectifier net current	A
p_e	Electrical power	W
p_m	Mechanical power	W
p_Q	Thermal power	W
p_H	Magnetic field power	W
p_C	Electric field power	W
P	Magnetic poles	ND
N_{sr}	Stator-to-rotor turns ratio	ND
R	Resistance	Ω
U_{fw}	Diode forward voltage	V
$[]_d$	D-axis quantity	
$[]_q$	Q-axis quantity	
$[]_f$	Field quantity	
$[]_{kd}$	D-axis damper quantity	
$[]_{kq}$	Q-axis damper quantity	
$[]_l$	Leakage quantity	
$[]_m$	Magnetizing quantity	
$[]_N$	Quantity scaled by N_{sr}	

DQ0 Transform

Because there are several versions of the direct-quadrature-zero (DQ0) transform [25] and the choice of transform can affect the form of some of the equations discussed, it is pertinent to describe the particular form of DQ0 transform used in this work. The power-invariant, right-handed, ABC-sequenced DQ0-transform matrix has the form

$$\sqrt{\frac{2}{3}}\cdot\begin{bmatrix} \cos(\theta_s) & \cos\left(\theta_s-\frac{2\pi}{3}\right) & \cos\left(\theta_s+\frac{2\pi}{3}\right) \\ -\sin(\theta_s) & -\sin\left(\theta_s-\frac{2\pi}{3}\right) & -\sin\left(\theta_s+\frac{2\pi}{3}\right) \\ \frac{1}{\sqrt{2}} & \frac{1}{\sqrt{2}} & \frac{1}{\sqrt{2}} \end{bmatrix}, \tag{45}$$

where θ_s is the angle of the flux field (the rotor angle scaled by the pole pairs, *P*/2). The power-invariant DQ0 transform does not scale the vector magnitude, so the rotor values do not need to be scaled to be properly referenced to the DQ0 values. By contrast, using the power-variant transform, the rotor values must be scaled by a factor of $\sqrt{2/3}$ to correctly reference them to the stator side. The form shown in (45) was chosen, among other reasons, because it is simply an axial rotation and incurs no scaling of any kind. It is also convenient that its inverse equals its transpose.

Using the power-invariant transform, the electromagnetically generated torque of a synchronous machine is

$$\tau=\frac{P}{2}\cdot\left(\lambda_q\cdot i_d-\lambda_d\cdot i_q\right). \tag{46}$$

The sign of this torque is such that the product of positive torque and positive shaft speed is positive mechanical power into the machine. If the power-variant DQ0 transform were used, then torque would be

$$\tau = \frac{3}{2}\frac{P}{2} \cdot \left(\lambda_q \cdot i_d - \lambda_d \cdot i_q\right). \tag{47}$$

Clearly, the form of the DQ0 transform has an effect on the form of other equations.

Dynamical Equations

To provide context and to clarify the choice of signs, the dynamical equations for a synchronous machine with damper windings and no exposed neutral are

$$\frac{d}{dt}\begin{bmatrix} \lambda_d \\ \lambda_q \\ \lambda_{fN} \\ \lambda_{kdN} \\ \lambda_{kqN} \end{bmatrix} = \begin{bmatrix} u_d - R_s i_d + \lambda_q \omega_s \\ u_q - R_s i_q - \lambda_d \omega_s \\ u_{fN} - R_{fN} i_{fN} \\ -R_{kdN} i_{kdN} \\ -R_{kqN} i_{kqN} \end{bmatrix}, \tag{48}$$

where the variables subscripted with N have been multiplied by N_{sr}, the effective stator-to-rotor turns ratio. Although this form is often used in the context of motors, it is consistent with the choice of defining all powers as being pointed into the system. The full derivation for the dynamical equations can be found in Appendix B: Synchronous Machine Dynamics.

Inductance Modeling

In [38], the design of a permanent magnet (PM) motor is detailed and the use of nonlinear modeling of its inductances is mentioned. In [40], this nonlinear modeling method is explained. The fitting is very good with normalized mean absolute differences (NMADs [40]) below 0.5%. It uses a rational function to fit the direct (D) and quadrature (Q) inductances over the D and Q currents: 2 states. The technique is somewhat complicated, yet this modeling task is relatively simple compared to that of modeling the magnetics of a synchronous machine (SM) generator with damper windings: at least 5 states.

Collecting the data

The main generator is modeled in Maxwell 2D, a finite element method (FEM) software. The established relationship between flux linkage and inductance [41] in an SM is

$$\begin{bmatrix} \lambda_d \\ \lambda_q \\ \lambda_{fN} \\ \lambda_{kdN} \\ \lambda_{kqN} \end{bmatrix} = \underline{\underline{L}} \times \begin{bmatrix} i_d \\ i_q \\ i_{fN} \\ i_{kdN} \\ i_{kqN} \end{bmatrix}, \tag{49}$$

$$\underline{\underline{L}} = \begin{bmatrix} L_{sl} + L_{md} & 0 & L_{md} & L_{md} & 0 \\ 0 & L_{sl} + L_{mq} & 0 & 0 & L_{mq} \\ L_{md} & 0 & L_{flN} + L_{md} & L_{md} & 0 \\ L_{md} & 0 & L_{md} & L_{kldN} + L_{md} & 0 \\ 0 & L_{mq} & 0 & 0 & L_{klqN} + L_{mq} \end{bmatrix} \tag{50}$$

Note that the inductance matrix is sparse. Yet, the inductance matrix that the FEM software develops is full. This is partly numerical error and perhaps partly a reality of cross-saturation. However, it would be immensely simplifying to force the matrix to be sparse and to do so without too much loss of data. To accomplish this, the FEM inductance values are neglected in favor of the flux linkages, which are then used to build the sparse inductance matrix.

The flux linkages are functions of each of the five currents (i_d, i_q, i_f, i_{kd}, and i_{kq}) and of the rotor angle, θ_m. At first glance, it would appear that all of these parameters should be varied during FEM sweeps, which would take a very long time. However, some simplifying steps can be taken. The basis of (49) is that the effects of all the currents can be grouped into just two axes: D and Q. (For the unbalanced case, the zero axis can be treated separately.) This leads to the development of the magnetizing currents:

$$\begin{aligned} i_{md} &= i_d + i_{fN} + i_{kdN} \\ i_{mq} &= i_q + i_{kqN} \end{aligned} . \tag{51}$$

The magnetizing inductances (L_{md} and L_{mq}) are functions of just these magnetizing currents. At this point, the problem is reduced to fitting over just two currents and the rotor angle.

In many cases, the effects of rotor angle can be neglected. Rather than run many FEM simulations varying rotor angle in order to get good average values, rotor angles can be found where the flux linkage values pass through their own averages. This means that for a given set of current values, only one simulation needs to be run. The variation in flux linkage is most evident at high saturation. Figure 52 shows an example of flux linkage variation over rotor angle with the points where it crosses its own average marked. These points do not vary with current since they are determined mostly by the machine’s geometry. Therefore, by locking the rotor at one of these points, the FEM simulation sweeps can be made without any concern for variations in rotor angle. This can significantly reduce the number of simulations required to properly analyze a machine’s magnetics.

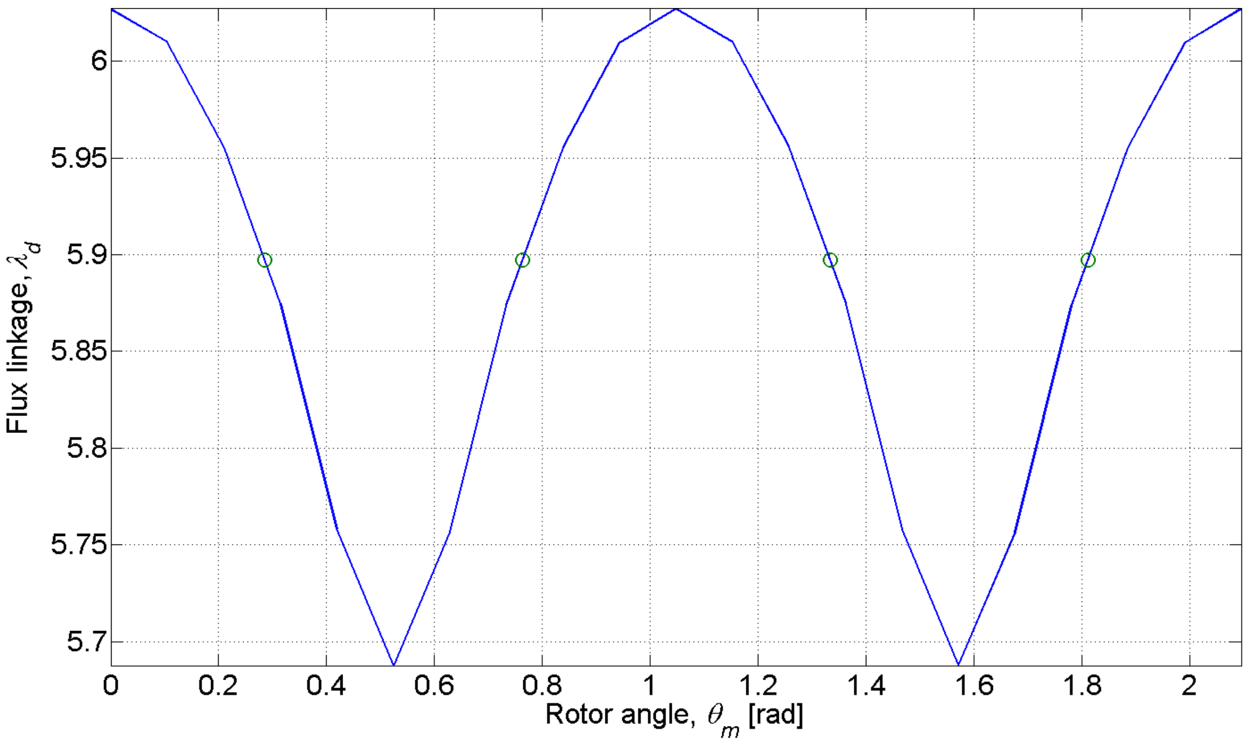

Figure 52. D-axis flux linkage values over rotor angle for the PM motor of [38]. The flux linkages are normalized per unit length. The points where the flux linkage crosses through its average are marked with circles.

In determining the magnetizing inductances, it would be superfluous to vary the damper currents in addition to varying the rotor's field current. So, the FEM simulations are run, varying only i_d, i_q, and i_f. Figure 53 shows a side view of some of the rotor flux linkages. Each layer corresponds to a specific value of i_f. Finally, three sets of flux linkage values are used to determine the inductances: λ_d, λ_q, and λ_f.

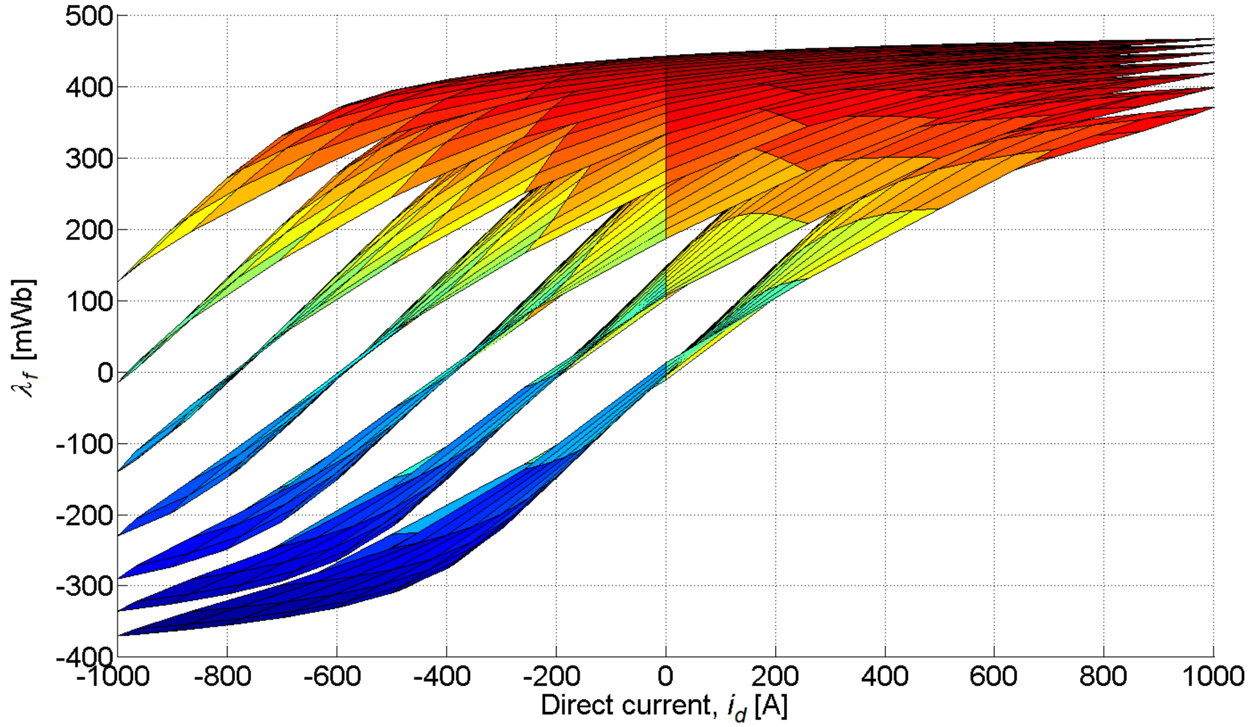

Figure 53. Side view of the rotor's field flux linkage in mWb with three currents varied: i_d, i_q, and i_f. This shape was characteristic of the direct and field flux linkages on both the exciter and the main.

Modeling with polynomials

One approach to fitting the flux linkages of the generator involves polynomials. Although (51) indicates that the currents can be combined into just two magnetizing currents, the effective stator-to-rotor turns ratio, N_{sr}, is necessary but not obvious. Without knowing this, a model of the flux linkages or inductances would need to include all currents, without combination. So, the following polynomial model is used for each of the three primary flux linkages (λ_d, λ_q, and λ_f):

$$\lambda(i_d, i_q, i_f) = \sum_{n=1}^{N} \left(\sum_{m=1}^{M} G_{m,n} i_f^{\ c_m} \right) i_d^{\ a_n} i_q^{\ b_n} \ , \qquad (52)$$

where n, m, N, and M are integers, G is a matrix of constants, and a, b, and c are arrays of integer exponents. The complexity of the polynomial equation is determined primarily by the size of the G matrix. In the case of the generator modeled in this work, some flux linkages require a G matrix as large as 7 by 14. While these are fairly large matrices, they do lead to very low flux linkage fitting NMADs: all less than 0.6%.

Figure 54 shows smooth flux linkage values calculated for the main's field. Up to the current values shown the fit is very good and well behaved. However, moving beyond the limits of the original tables by just 20%, the formula quickly deviates from reasonable (Figure 55).

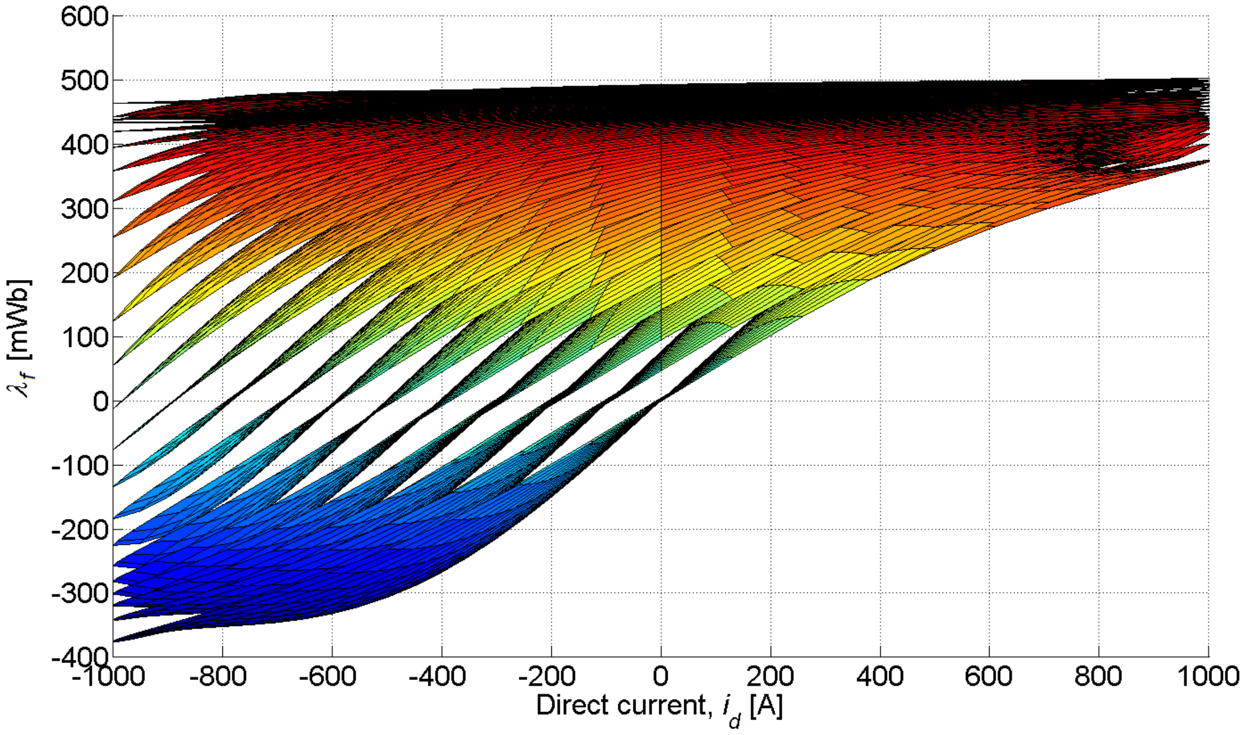

Figure 54. The field flux linkage for the main generator as calculated by formula. The points chosen include points in between those used to tune the formula.

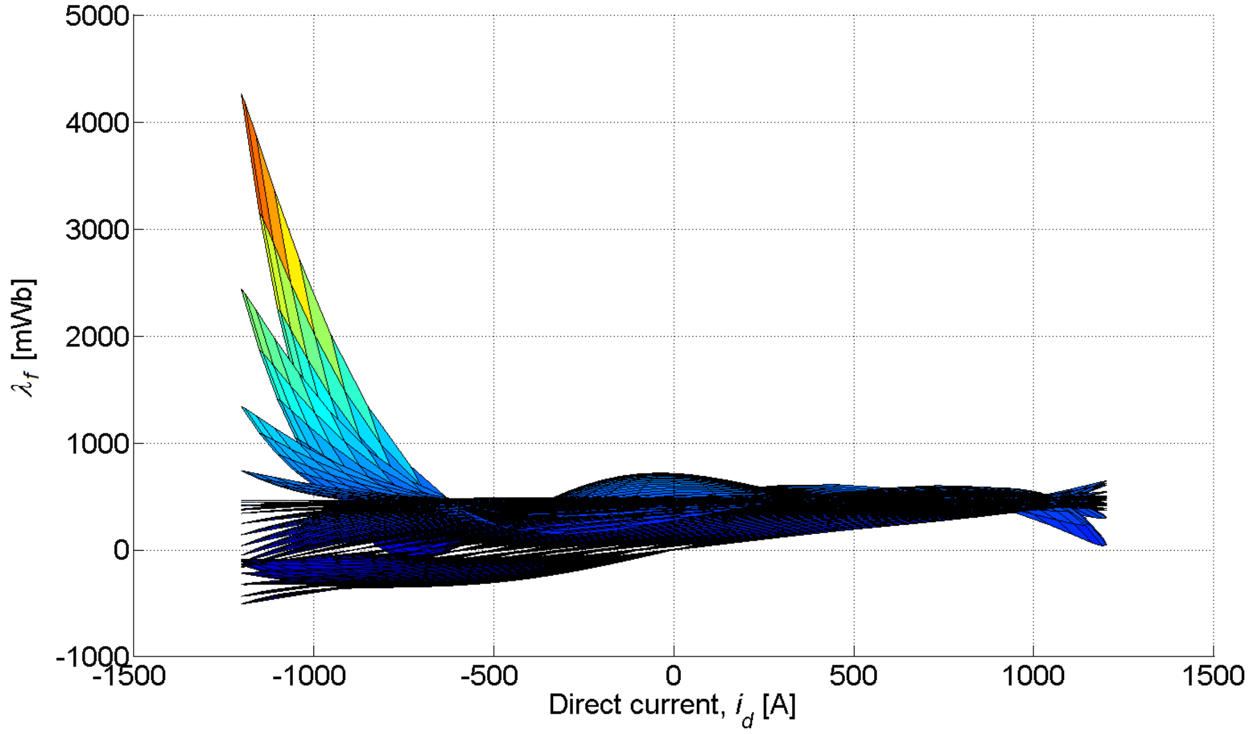

Figure 55. The field flux linkage for the main generator as calculated by formula with all three currents extended 20% beyond the original tables.

These excursions cause the generator simulation to become unstable. Therefore, it is necessary to make sure that the fitting is done for values far beyond what would ever be used during simulation. This requires getting much more FEM simulation results, which is a very time-consuming process.

Modeling with rational functions

In [40], a simple version of the rational function inductance model was developed for L_{md} and L_{mq} and is repeated here slightly altered:

$$L(i_d, i_q) = \frac{k_1}{1 + k_2 |i_d|^{k_3} + k_4 |i_q|^{k_5}} + k_6, \tag{53}$$

where the k values are scalars to be tuned for the particular inductance (L_{md} or L_{mq}). The last coefficient, k_6, is not used for L_{md}. In addition to these k values, the effective stator-to-rotor turns ratio N_{sr} and the leakage inductances L_{sl} and L_{flN} are the coefficients tuned in order to fit the three flux linkage data sets: λ_d, λ_q, and λ_f. Altogether there are 14 coefficients. Maxwell 2D with RMxpert has a feature to automatically calculate the damper leakage inductances which are scalars and are far less critical.

The D-axis magnetizing flux linkage of the main as a rational function of currents is shown in Figure 56. The derived D-axis magnetizing inductance of the main is shown in Figure 57. The fit is fairly good; and, as discussed in [40], the rational function has the benefit of avoiding Runge's phenomenon [31]. The primary disadvantage of the rational function is that it saturates too quickly, an effect which only becomes apparent in very deep saturation. Figure 58 repeats the flux linkages of Figure 56 but up to a much higher current. In reality, flux linkage monotonically increases with current, but the behavior of the rational function approach as shown in Figure 58 does not follow that pattern. If going into deep saturation is a likely possibility during simulation, then this deviation becomes more than just an error in flux linkage. It can cause a positive feedback to saturation and instability of the simulation.

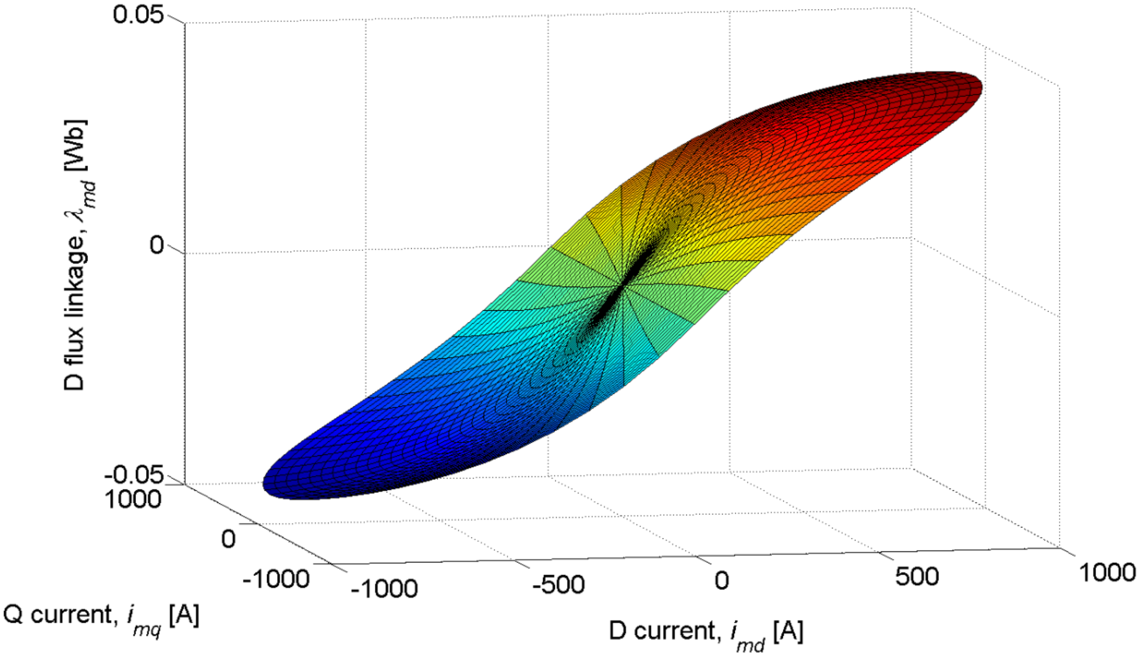

Figure 56. The D-axis magnetizing flux linkage (L_{md} i_{md}) of the main as a rational function of D and Q magnetizing currents.

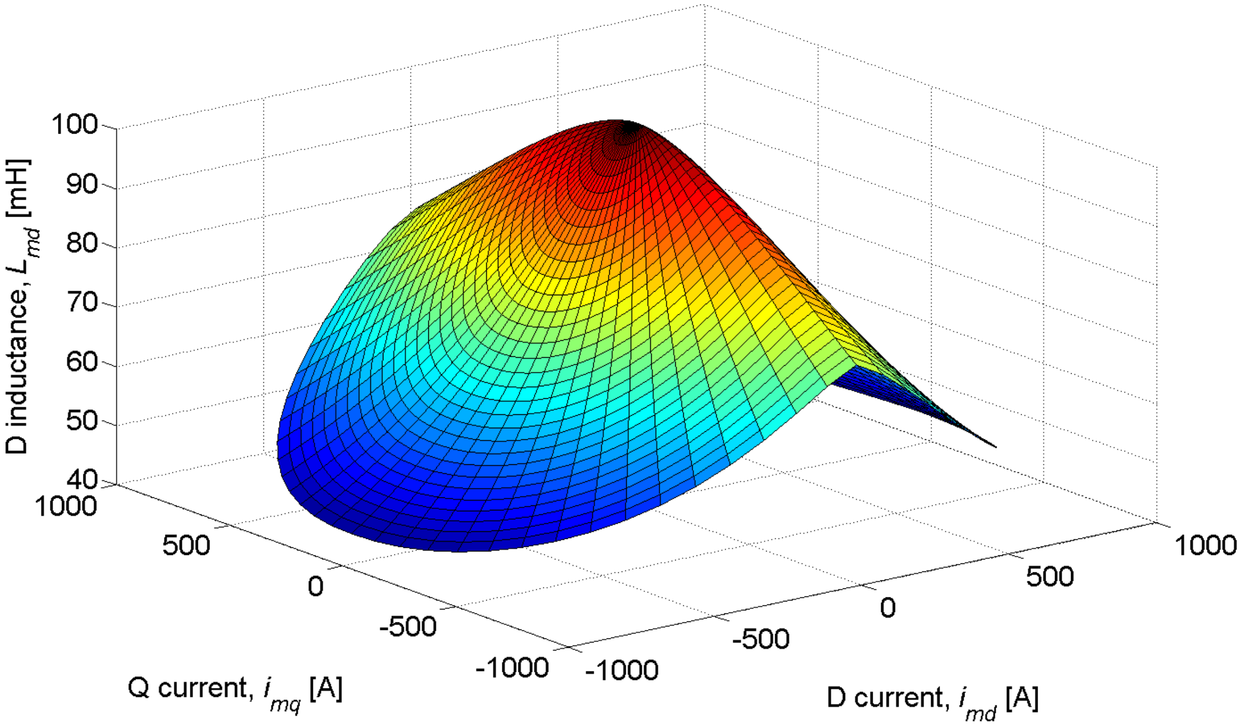

Figure 57. The D-axis magnetizing inductance, L_{md}, of the main as a rational function of D and Q magnetizing currents.

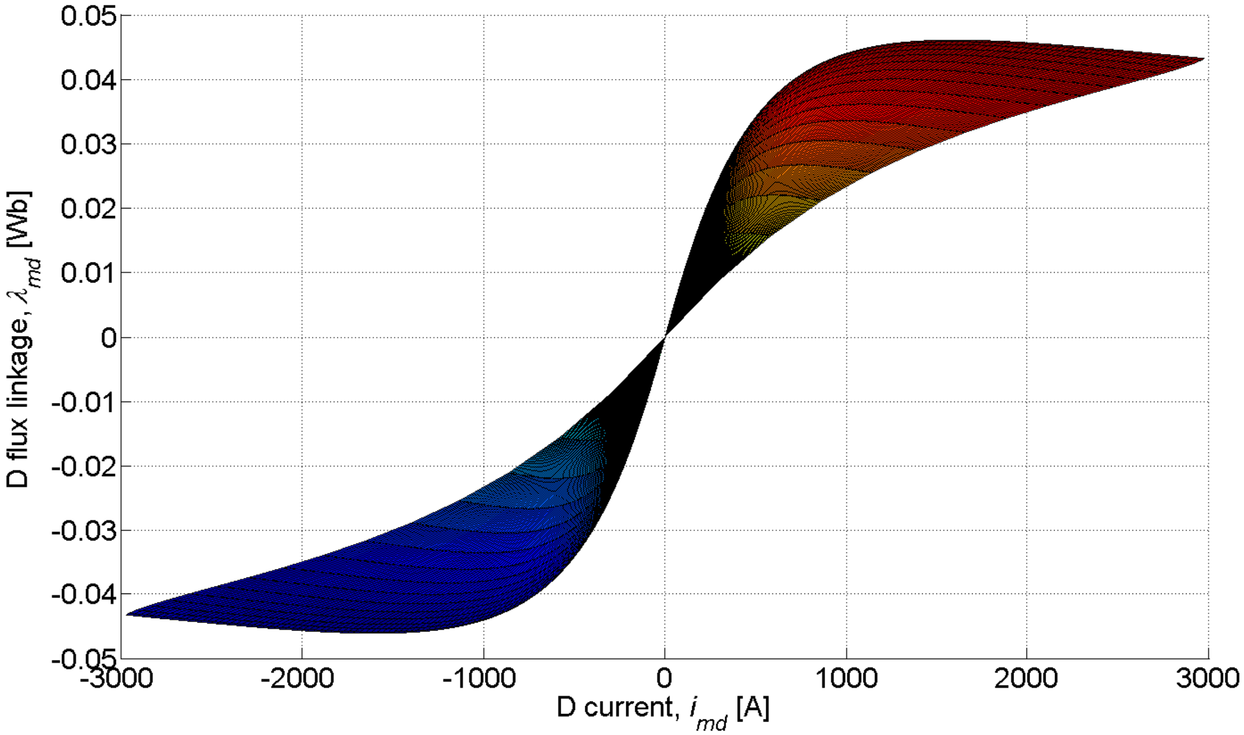

Figure 58. The D-axis magnetizing flux linkage (L_{md} i_{md}) of the main as a rational function of D and Q magnetizing currents.

Modeling with logistic functions

A few papers were found that use exponentials to model the magnetics of machines. In [42], the following equation is used:

$$\lambda(i,\theta) = a_1(\theta)[1-\exp[a_2(\theta)i]] + a_3(\theta)i \,, \tag{54}$$

where the subscripted *a* variables are coefficients of the mechanical rotor position θ and i is the phase current magnitude. The same idea shows up in [43]:

$$\psi_{ph} = \psi_s\left(1-e^{-f(\theta)i_{ph}}\right), \tag{55}$$

where ψ_{ph} is the phase flux linkage, ψ_s is a constant, θ is the phase angle, f is a trigonometric function, and i_{ph} is the phase current magnitude.

The magnetics modeling method used in this work depends on a logistic function [44] as shown here:

$$f(r)=\left(\frac{2}{1+e^{-r}}-1\right) \tag{56}$$

$$L_m = k_1 \frac{f(r)}{r}+k_2 \tag{57}$$

$$r=\sqrt{k_3 i_{md}{}^2+k_4 i_{mq}{}^2}\ . \tag{58}$$

Here, f is the logistic function, L_m is the magnetizing inductance, and r is the magnitude of scaled currents. Altogether, to model the three flux linkages, only 10 coefficients are needed. Figure 59 shows the difference between the logistic function of (56) and exponential functions like (55). The exponential function causes the inductance to be in saturation even at zero current, but the logistic function allows the inductance to remain fairly constant about the origin. An additional benefit is that deep saturation using a logistic function is always monotonically increasing (Figure 60). No other work has been found to use this method.

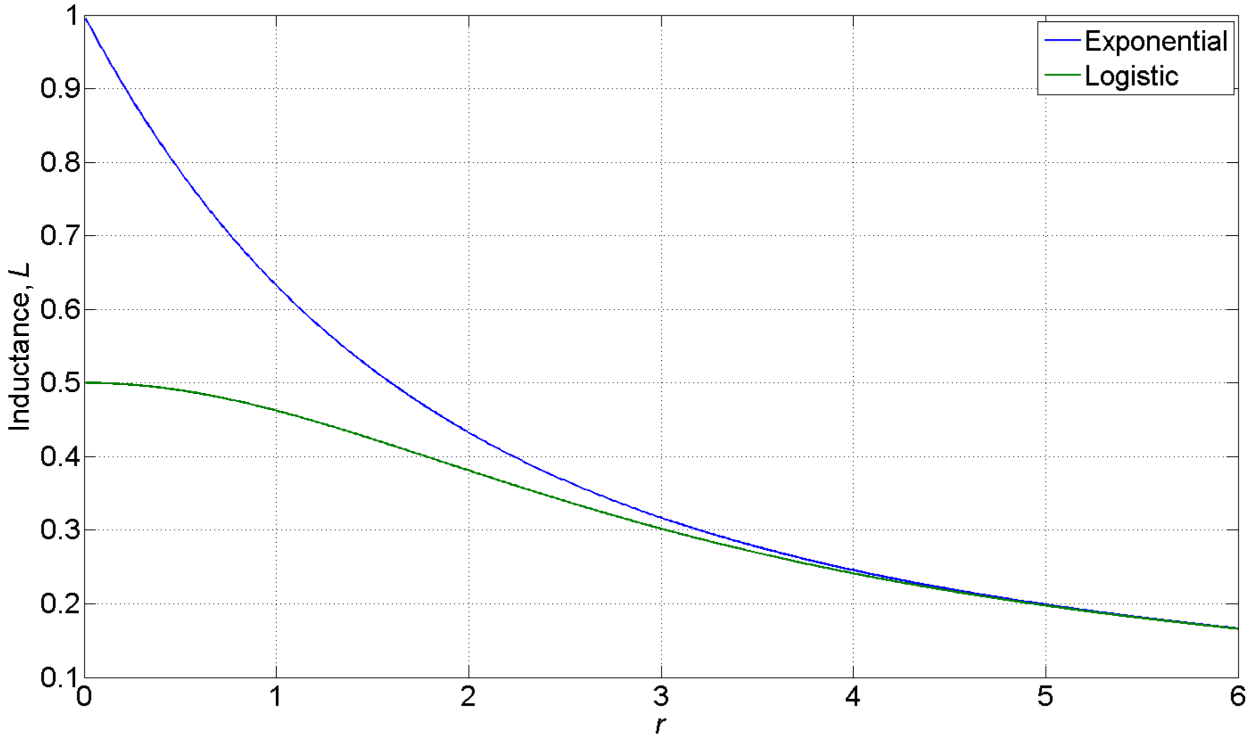

Figure 59. Generalized inductances developed using an exponential function (blue) and a logistic function (green).

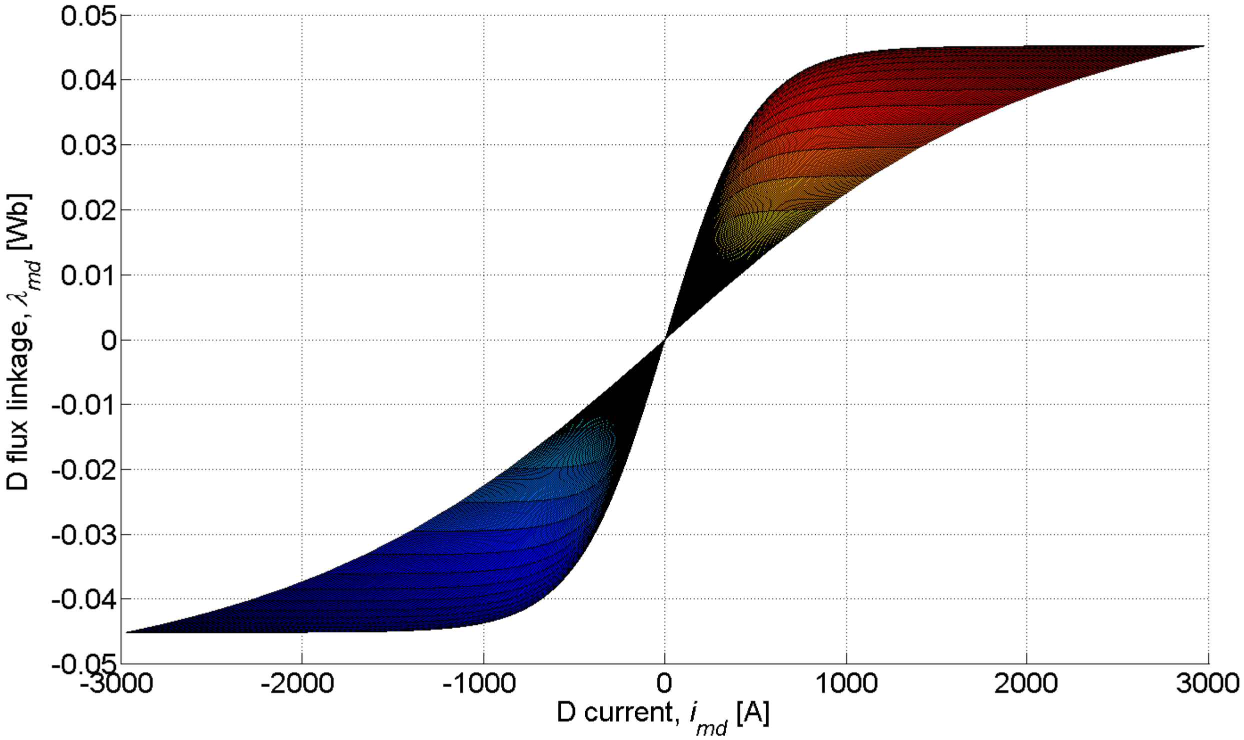

Figure 60. The D-axis magnetizing flux linkage (L_{md} i_{md}) of the main as a logistic function of D and Q magnetizing currents.

Modeling comparison

Figure 61 shows a comparison of the NMADs for fitting λ_d, λ_q, and λ_f using the polynomial, rational, and logistic methods. The number of coefficients required for each method are 347 for polynomial, 14 for rational, and 10 for logistic. The rational and logistic methods have nearly the same error of fitting; and while the polynomial method does fit better than the other two, it requires far more coefficients. For this reason and for its ability to properly model deep-saturation effects, the logistic method was chosen to model the magnetics in this work.

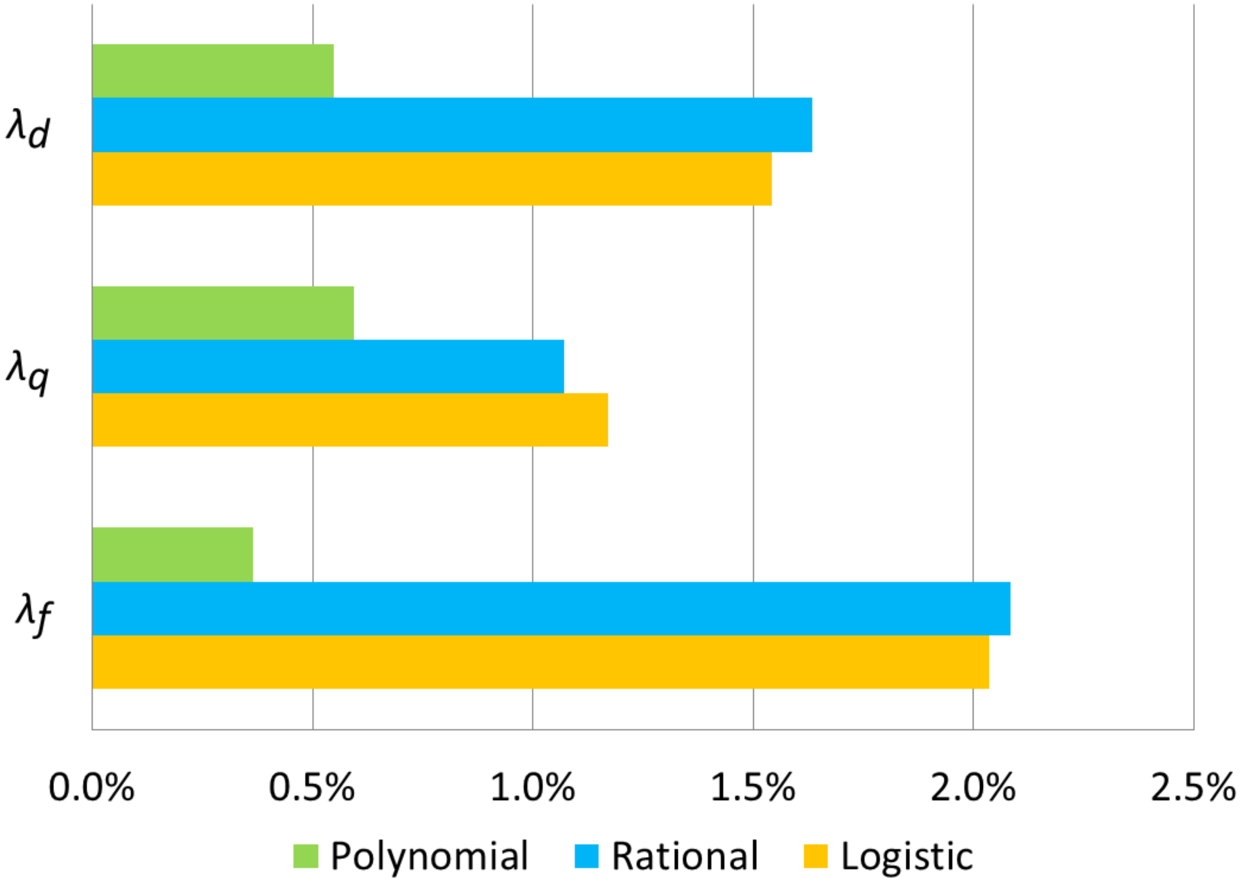

Figure 61. Comparison of the NMADs of for the polynomial, rational, and logistic methods for the main machine.

Full Flux Linkage Derivative

The relationship among flux linkage, inductance, and current is defined in (49) and (50). Taking the full derivative and solving for the current derivative gives the explicit solution

$$\frac{d}{dt}\underline{i} = \underline{\underline{M}}^{-1} \times \frac{d}{dt}\underline{\lambda} \tag{59}$$

$$\underline{\underline{M}} = \frac{d}{d\underline{i}}\underline{\underline{L}} \times \underline{i} + \underline{\underline{L}}, \tag{60}$$

where the time-derivatives of flux linkage are defined in (48). This *M* matrix is full and its analytical inverse is prohibitively complicated. To simplify matters, the first term in *M* is often neglected. So, while the inductance is allowed to be nonlinear, it is assumed that its derivative over current is relatively small. Yet, this can be a gross over-simplification. Using the logistic method for the D-axis magnetizing flux linkage, the percent difference is shown in Figure 62. This shows $\left|\underline{\underline{M}} - \underline{\underline{L}}\right| / \underline{\underline{L}}$ converted to a percentage. Figure 63 shows a comparison of *M* and *L*. The derivative of inductance has the effect of weakening the inductance, and this effect is not negligible.

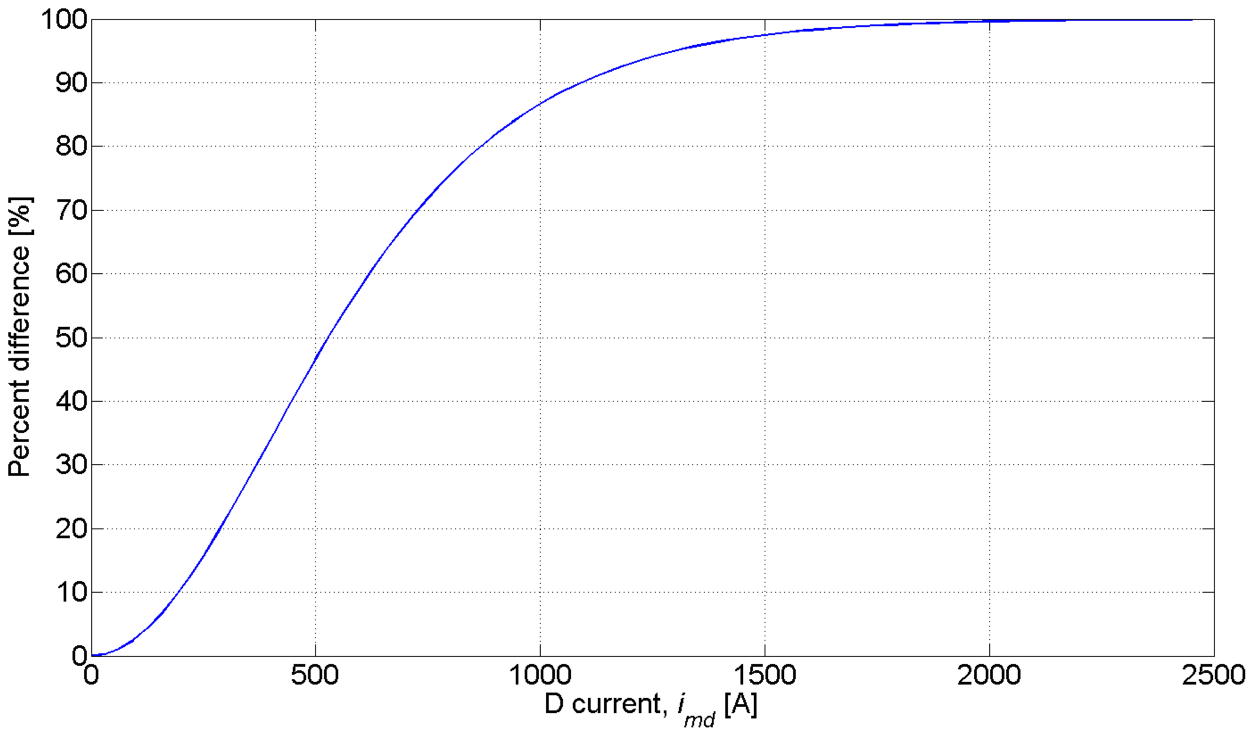

Figure 62. Percent difference of *M* relative to *L*.

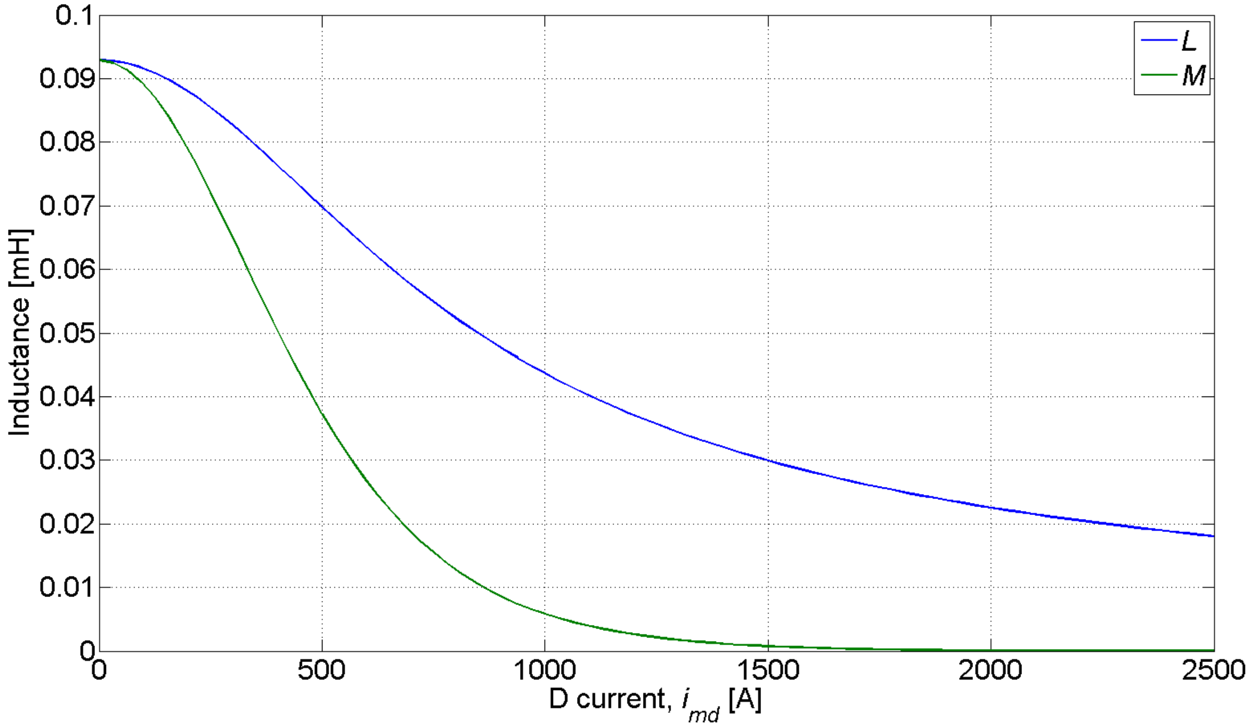

Figure 63. D-axis magnetizing inductance (blue) and *M* (green).

Rather than using the explicit solution to get the full derivative, the derivative of inductance is numerically calculated during simulation. The basis of this approximate solution is the use of the last time-step's change in inductance in place of this time-step's change in inductance:

$$\begin{gathered}\underline{\lambda} \underset{\downarrow}{=} \underline{\underline{L}} \times \underline{i} \\ \frac{d}{dt}\underline{\lambda} \underset{\downarrow}{=} \frac{d}{dt}\underline{\underline{L}} \times \underline{i} + \underline{\underline{L}} \times \frac{d}{dt}\underline{i} \\ \frac{d}{dt}\underline{i} = \underline{\underline{L}}^{-1} \times \left(\frac{d}{dt}\underline{\lambda} - \frac{d}{dt}\underline{\underline{L}} \times \underline{i} \right)\end{gathered} \quad . \tag{61}$$

If the time step is very small, then this approximation is quite reasonable [45]. This means that only the sparse *L* matrix needs to be inverted, which is relatively easy.

Full-bridge Rectifier with Freewheeling

The full generator model uses a full-wave rectifier. When using a full-wave rectifier, it is critical to recognize that the freewheeling condition can and does occur easily. In this condition, both diodes in a leg are conducting and the DC current freely flows independent of the phase current. To properly model the rectifier, the problem is simplified by using a piecewise model of a diode where only the forward voltage drop, U_{fw}, and on resistance, R_{on}, are considered. To build a model of the full-wave rectifier, each leg can be considered individually (Figure 64).

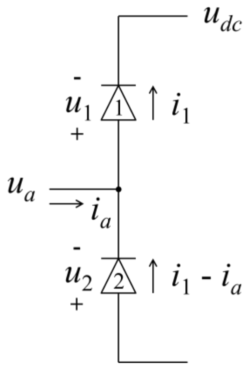

Figure 64. One leg of a full-wave rectifier showing voltage drops across both top (1) and bottom (2) diodes.

The phase current i_a is oriented into the rectifier and the phase voltage u_a has the same reference as the DC voltage, u_{DC}. For this derivation, it is given that i_a and u_{DC} are known and i_1 and u_a are not.

In the non-freewheeling condition, only one of the two diodes on the leg is conducting: diode 1 or 2. If i_a is positive, then u_a will be slightly higher than u_{DC} due to the voltage drop of diode 1, and i_1 will equal i_a. If i_a is negative, then the u_a will be slightly less than 0 due to the voltage drop of diode 2, and i_1 will be 0. These non-freewheeling relationships can be summarized in (62) and (63).

$$u_a = \begin{cases} u_{dc} + U_{fw} + R_{on} i_a : i_a \geq 0 \\ -U_{fw} + R_{on} i_a : i_a < 0 \end{cases} \tag{62}$$

$$i_1 = \begin{cases} i_a : i_a \geq 0 \\ 0 : i_a < 0 \end{cases} \tag{63}$$

If, however, the rectifier is in freewheeling mode, it means that both diodes in a leg are conducting. If we define the critical voltage of a diode as the voltage across the diode such that it only just barely conducts, then freewheeling occurs when the DC voltage u_{DC} has dropped far enough below zero so as to exceed the critical voltages of both diodes. However, the phase current i_a can disrupt this condition by increasing the total voltage drop across one diode such that the headroom for the voltage drop across the other diode is too small for it to conduct. This means there is a critical current i_{crit} that the magnitude of i_a must not exceed for the freewheeling condition to exist. Using Figure 64 as a reference, we begin with the following voltage relationships which are true during the freewheeling condition:

$$\begin{aligned} u_1 &= U_{fw} + R_{on} i_1 \\ u_2 &= U_{fw} + R_{on}(i_1 - i_a). \\ u_1 + u_2 &= -u_{dc} \end{aligned} \tag{64}$$

If the freewheeling condition just barely exists, then either i_1 or $(i_1 - i_a)$ equals zero. Either situation will lead to the same conclusion. Supposing then that it is the current through diode 2 which is zero, we can rewrite the voltage relationships of (64) taking into account that i_a now equals i_{crit} as

$$\begin{aligned} &u_1 = U_{fw} + R_{on} i_{crit} \\ &u_2 = U_{fw} \qquad , \\ &u_1 + u_2 = -u_{dc} \end{aligned} \tag{65}$$

where i_{crit} must equal i_1. We can then solve for i_{crit}:

$$\begin{aligned} &U_{fw} + R_{on} i_{crit} + U_{fw} = -u_{dc} \\ &\Rightarrow i_{crit} = \frac{-u_{dc} - 2U_{fw}}{R_{on}} \qquad . \end{aligned} \tag{66}$$

This is the critical current, and the magnitude of i_a must be less than or equal to it for the freewheeling condition to exist in that leg:

$$|i_a| \le i_{crit} \equiv \frac{-u_{dc} - 2U_{fw}}{R_{on}} . \tag{67}$$

The current through diode 1, i_1, can be found by starting with (64) and rearranging:

$$\begin{aligned} &u_1 + u_2 = -u_{dc} \\ &\Rightarrow U_{fw} + R_{on} i_1 + U_{fw} + R_{on}(i_1 - i_a) = -u_{dc} \\ &\Rightarrow 2R_{on} i_1 = -u_{dc} - 2U_{fw} + R_{on} i_a \\ &\Rightarrow i_1 = \frac{1}{2}\left[\frac{(-u_{dc} - 2U_{fw})}{R_{on}} + i_a\right] \\ &\Rightarrow i_1 = \frac{1}{2}(i_{crit} + i_a) \end{aligned} \tag{68}$$

We can now solve for the phase voltage u_a during the freewheeling condition:

$$\begin{aligned} &u_a = u_{dc} + u_1 \\ &\Rightarrow u_a = u_{dc} + (U_{fw} + R_{on} i_1) \\ &\Rightarrow u_a = u_{dc} + U_{fw} + R_{on} \frac{1}{2}\left[\frac{(-u_{dc} - 2U_{fw})}{R_{on}} + i_a\right]. \\ &\Rightarrow u_a = u_{dc} + U_{fw} - \frac{1}{2} u_{dc} - U_{fw} + \frac{1}{2} R_{on} i_a \\ &\Rightarrow u_a = \frac{1}{2}(u_{dc} + R_{on} i_a) \end{aligned} \tag{69}$$

Therefore, in freewheeling mode, the following are true:

$$u_a = \frac{1}{2}(u_{dc} + R_{on} i_a) \tag{70}$$

$$i_1 = \frac{1}{2}\left(i_{crit} + i_a\right) \tag{71}$$

So, given the phase current i_a and the DC voltage u_{DC}, the first step to evaluating the full-wave rectifier is to evaluate the critical current (67) and check if the magnitude of i_a is less than or equal to it. If it is not then that leg is not in freewheeling mode and (62) and (63) apply. If the magnitude of i_a is less than i_{crit}, then the leg is freewheeling, and (70) and (71) apply.

This logic must be applied to each leg of the rectifier and the total current from the rectifier would be the sum of the currents coming out of each top diode. In this model, a capacitor exists on the DC side of the rotating rectifier in order to pair the current source main machine with the current source DC side of the rectifier.

Power Analysis

In this work, power has been defined such that it is positive when flowing into the machine. Multiplying (48) by the respective currents results in the following power equations:

$$\begin{aligned}
u_d i_d &= R_s i_d^{\,2} - \lambda_q \omega_s i_d + \frac{d}{dt}\lambda_d i_d \\
u_q i_q &= R_s i_q^{\,2} + \lambda_d \omega_s i_q + \frac{d}{dt}\lambda_q i_q \\
u_{fN} i_{fN} &= R_{fN} i_{fN}^{\,2} + \frac{d}{dt}\lambda_{fN} i_{fN} \qquad . \\
0 &= R_{kdN} i_{kdN}^{\,2} + \frac{d}{dt}\lambda_{kdN} i_{kdN} \\
0 &= R_{kqN} i_{kqN}^{\,2} + \frac{d}{dt}\lambda_{kqN} i_{kqN}
\end{aligned} \tag{72}$$

The terms on the left represent electrical power flowing into the system. The resistive terms represent the power losses. The second terms on the right of the first two equations represent the mechanical power flowing out of the system. The last terms in each equation represent the power stored in the magnetic field. So, the electrical, mechanical, thermal, and magnetic powers flowing into the system are respectively

$$p_e = u_d i_d + u_q i_q + u_{fN} i_{fN} \tag{73}$$

$$p_m = \underbrace{\left(\lambda_q i_d - \lambda_d i_q\right)}_{\tau_s}\omega_s \Rightarrow \tau_s \omega_s \Rightarrow \left(\frac{\tau}{P/2}\right)\left(\omega\frac{P}{2}\right) \Rightarrow \tau\omega \tag{74}$$

$$p_Q = -\left(R_s {i_d}^2 + R_s {i_q}^2 + R_{fN} {i_{fN}}^2 + R_{kdN} {i_{kdN}}^2 + R_{kqN} {i_{kqN}}^2\right) \tag{75}$$

$$p_H = -\left(\frac{d\lambda_d}{dt} i_d + \frac{d\lambda_q}{dt} i_q + \frac{d\lambda_{fN}}{dt} i_{fN} + \frac{d\lambda_{kdN}}{dt} i_{kdN} + \frac{d\lambda_{kqN}}{dt} i_{kqN}\right). \tag{76}$$

The total power balance equation is

$$0 = p_e + p_Q + p_m + p_H\,. \tag{77}$$

Note that the above power equations might differ from some other publications, but this depends on the form of the DQ0 transform used and the orientation of power vectors.

Simulation Results

The generator is designed with a DC-DC inverter controlling a synchronous exciter which feeds a full-wave rotating rectifier connected to a synchronous main which is then rectified by a full-wave rectifier, as seen in Figure 51.

The efficiency of the exciter is about 55%, suggesting it is undersized for the task. The efficiency of the main is about 95%. The powers of the exciter and main are shown in Figure 65 and Figure 66, respectively. Note, that core losses and friction have are not included here.

The ABC and DC voltages on the rotating rectifier are shown in Figure 67.

The control for the generator is a simple PI loop closing on the load voltage with a sampling frequency of 10 kHz and a switching frequency of 20 kHz. The reference is 270 V. The load voltage is shown in Figure 68.

The simulation is quite fast at less than 9 real-world seconds per simulated second on a 3.3 GHz Intel Core i5. This is a tremendous advantage. The tuning of the PI loop is automated, running through one simulation after another while varying the control coefficients procedurally. The speed of the simulation becomes very significant when trying to run so many simulations in a row. And, the speed of this code made the process take only a few minutes.

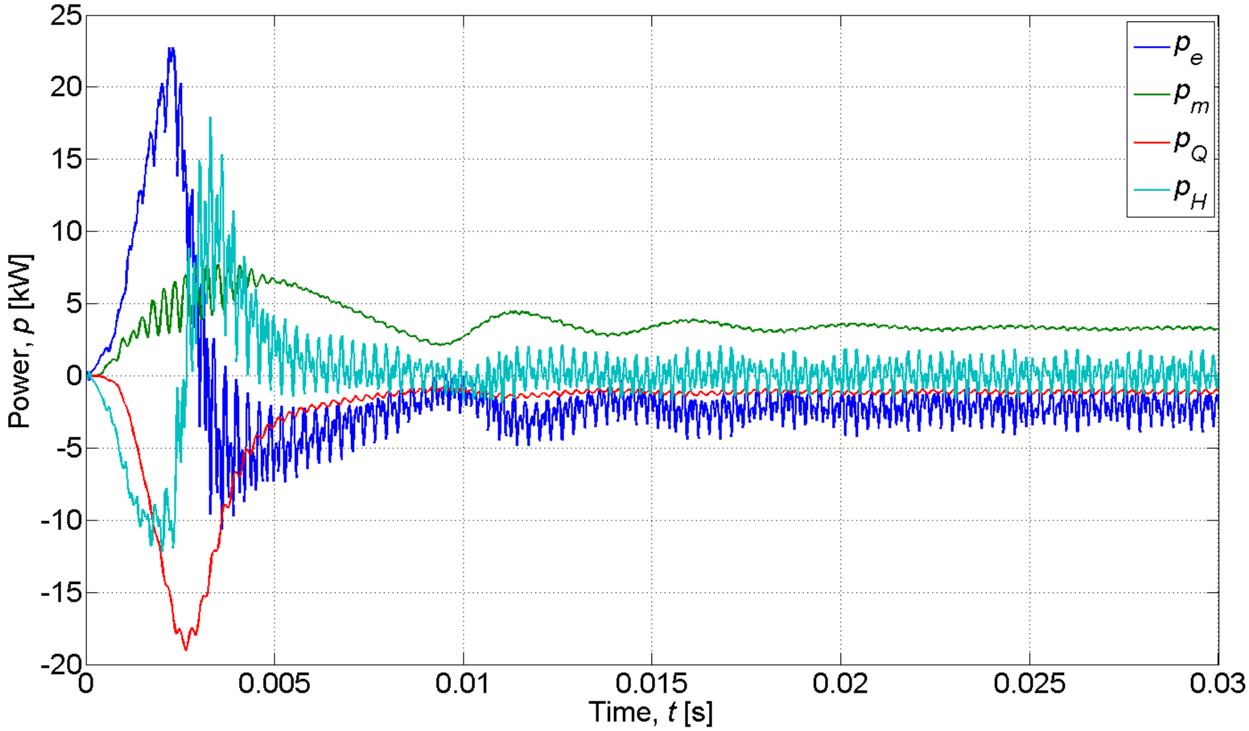

Figure 65. Powers into the exciter.

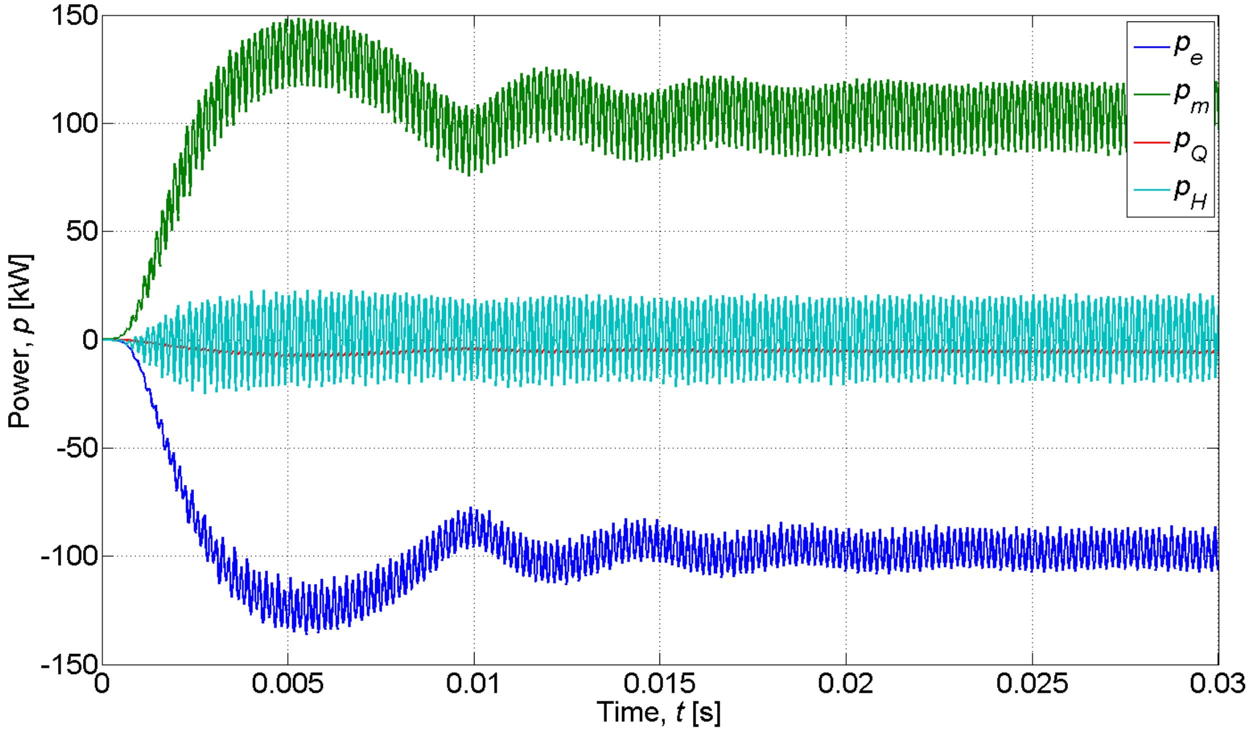

Figure 66. Powers into the main.

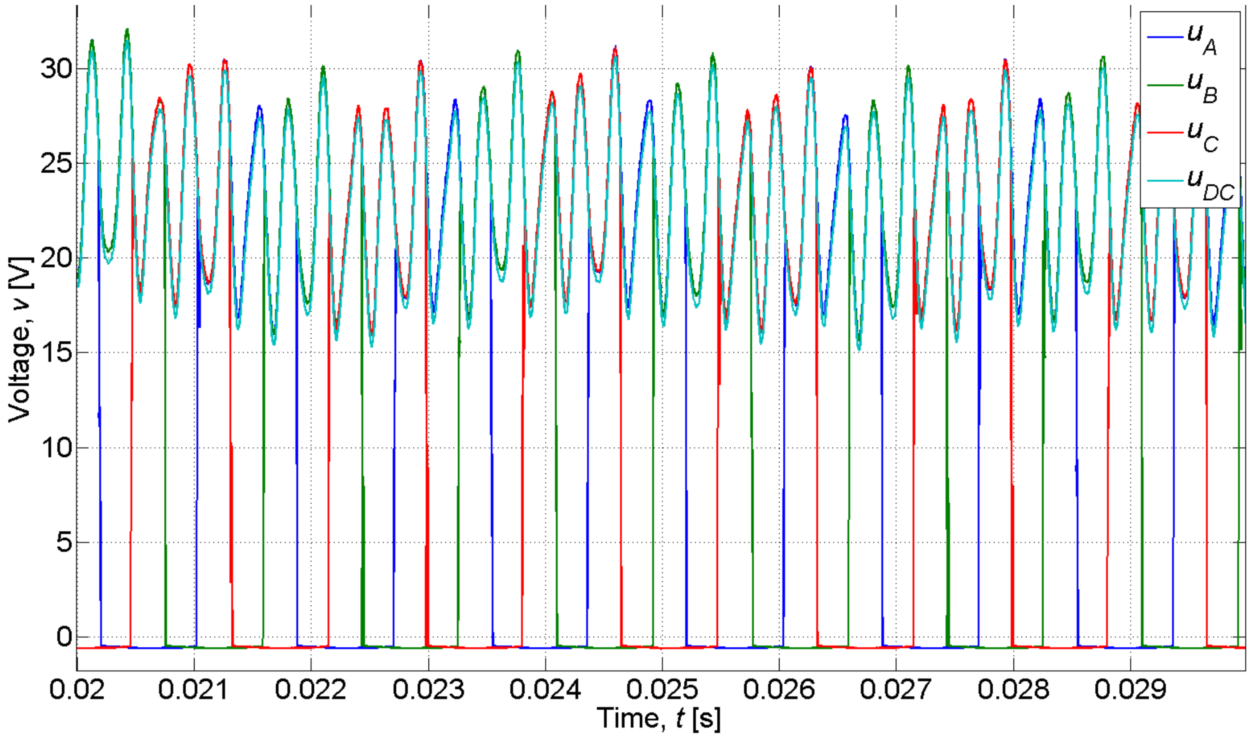

Figure 67. Voltages on the rotating rectifier. The DC voltage is slightly less than the peaks of the ABC voltages because of the forward voltage drop and on resistance of the diodes.

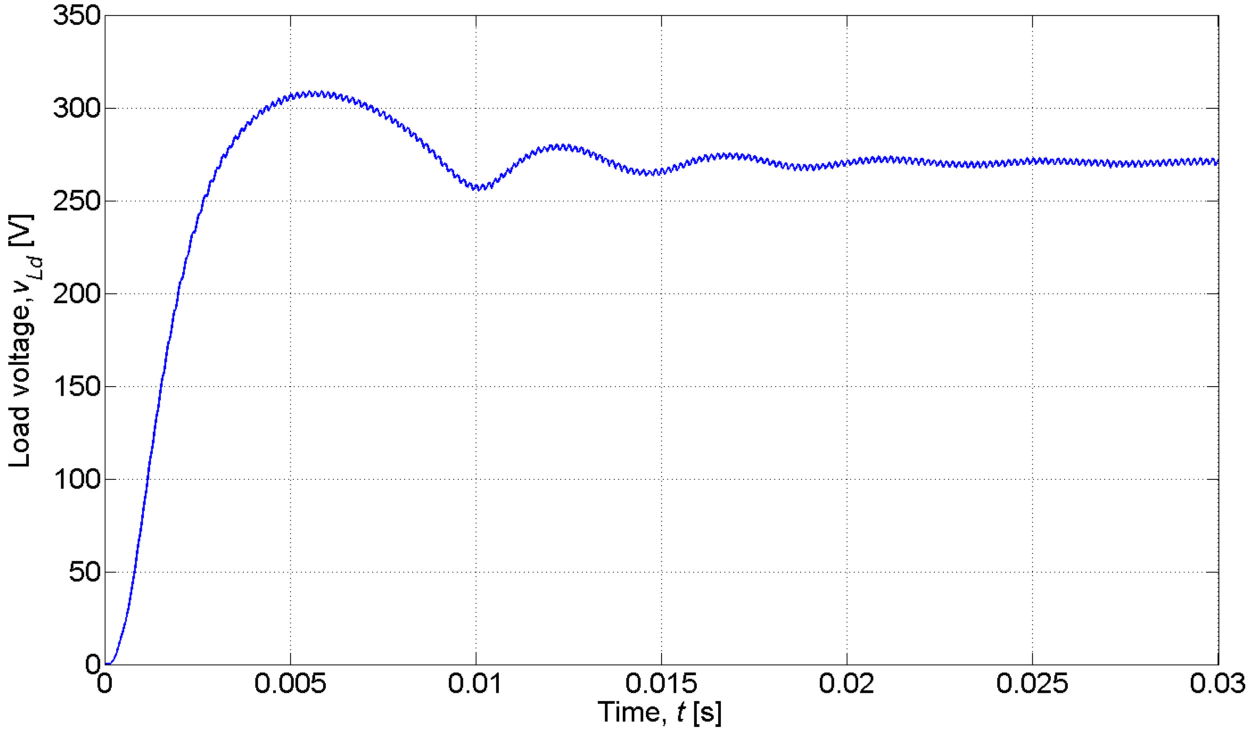

Figure 68. Load voltage controlled to 270 V.

Conclusion

In this work, much emphasis is placed on the magnetics modeling. There are potential risks of positive feedback, instability, poor saturation modeling even at low currents, and the requirement for excessive coefficients to model the magnetics. The logistic function method presented here solves all these problems.

Using nonlinear inductances suggests that the inductances can change over time. A full derivative of flux linkage should include derivatives of inductances. The work shows a practical method for doing so.

Choosing to model a generator using explicit mathematical models means that components such as full-wave rectifiers need careful consideration. Especially with rotating rectifiers, the freewheeling condition can occur. The model presented here treats that condition.

Finally, this generator model is able to quickly control the output voltage to 270 V while fully loaded at 100 kW. Tuning the control is a quick, automated process given each simulation runs at 9 s/s.

CHAPTER FIVE: CONCLUSION

The work described in this dissertation details the design of nonlinear, transient models of a permanent magnet electromechanical actuator (EMA) and a synchronous generator. Chapter 2 covers all the details of a full EMA simulation model, including electromagnetic dynamics, thermal networks, mechanical dynamics (such as friction and inertia), and control. Chapter 3 covers the methodology of building rational function fits of inductances for the EMA. Given the constant rotor flux linkage, an inductance model is simple enough and makes good sense. In Chapter 4, the development of a synchronous generator with field windings introduces a new layer of complexity. The methodology developed in Chapter 3 is extended to a synchronous generator, and a new method using logistic functions is developed.

The work of Chapters 2 and 3 was, to some degree, validated by experimentation. This was the culmination of about three years of work with the Air Force Research Laboratory. The magnetics modeling work of Chapter 4 in purely analytical in nature and is validated by fitting the given tables of data.

Altogether, this work represents the primary components of an electrically powered EMA system for an aircraft. These tools can be used to test new designs of EMAs or generators, test the interaction of a particular EMA with a particular generator, analyze the power demands of the system as a whole, evaluate the heating of a component during a specific mission profile, or test a new generator or motor control scheme. All of this leads to supporting the journey towards a more electric aircraft.

APPENDIX A: PERMANENT MAGNET MACHINE DYNAMICS

Voltage Equations

To begin the derivation of the dynamical equations of a permanent magnet (PM) machine, we start with the voltage equations:

$$u_d = R_s i_d + \frac{d}{dt}\lambda_d^* - \lambda_q \omega_{me} \tag{78}$$

$$u_q = R_s i_q + \frac{d}{dt}\lambda_q + \lambda_d^* \omega_{me}\,, \tag{79}$$

where λ_d^* and λ_q are defined as

$$\lambda_d^* = L_d i_d + \lambda_{PM} \tag{80}$$

$$\lambda_q = L_q i_q \tag{81}$$

and λ_{PM} is the flux linkage from the permanent magnets, which is constant.

Dynamical Equations

Rearranging (78) and (79) in terms of derivatives of flux linkage and reformatting into matrices, we get

$$\frac{d}{dt}\begin{bmatrix}\lambda_d^* \\ \lambda_q\end{bmatrix} = \begin{bmatrix} u_d - R_s i_d + \lambda_q \omega_{me} \\ u_q - R_s i_q - \lambda_d^* \omega_{me}\end{bmatrix} \tag{82}$$

where

$$\frac{d}{dt}\begin{bmatrix}\lambda_d^* \\ \lambda_q\end{bmatrix} = \begin{bmatrix} L_d \cdot \frac{di_d}{dt} + \frac{dL_d}{di_d}\cdot\frac{di_d}{dt}\cdot i_d + \frac{dL_d}{di_q}\cdot\frac{di_q}{dt}\cdot i_d \\ L_q \cdot \frac{di_q}{dt} + \frac{dL_q}{di_d}\cdot\frac{di_d}{dt}\cdot i_q + \frac{dL_q}{di_q}\cdot\frac{di_q}{dt}\cdot i_q \end{bmatrix}. \tag{83}$$

For simplification, the following substitutions are made:

$$L_{dd} = L_d + i_d \frac{dL_d}{di_d} \tag{84}$$

$$L_{dq} = i_d \frac{dL_d}{di_q} \tag{85}$$

$$L_{qd} = i_q \frac{dL_q}{di_d} \tag{86}$$

$$L_{qq} = L_q + i_q \frac{dL_q}{di_q}\,. \tag{87}$$

This turns (83) into

$$\frac{d}{dt}\begin{bmatrix} \lambda_d{}^* \\ \lambda_q \end{bmatrix} = \begin{bmatrix} L_{dd} & L_{dq} \\ L_{qd} & L_{qq} \end{bmatrix} \cdot \frac{d}{dt}\begin{bmatrix} i_d \\ i_q \end{bmatrix}. \tag{88}$$

Setting (88) equal to (82) and making two more substitutions, we get

$$\begin{bmatrix} L_{dd} & L_{dq} \\ L_{qd} & L_{qq} \end{bmatrix} \cdot \frac{d}{dt}\begin{bmatrix} i_d \\ i_q \end{bmatrix} = \begin{bmatrix} G_d \\ G_q \end{bmatrix}, \tag{89}$$

where

$$G_d = u_d - R_s i_d + \lambda_q \omega_{me} \tag{90}$$

$$G_q = u_q - R_s i_q - \lambda_d{}^* \omega_{me}\,. \tag{91}$$

Finally, by taking the inverse of the inductance matrix on the left, the dynamical equations with respect to current can be found to be

$$\frac{di_d}{dt} = \frac{L_{qq} G_d - L_{dq} G_q}{L_{dd} L_{qq} - L_{dq} L_{qd}} \tag{92}$$

$$\frac{di_q}{dt} = \frac{L_{dd} G_q - L_{qd} G_d}{L_{dd} L_{qq} - L_{dq} L_{qd}}\,. \tag{93}$$

APPENDIX B: SYNCHRONOUS MACHINE DYNAMICS

Introduction

As a first step, the dynamical equations for synchronous machines (SM) are developed with a simplifying assumption. Much of the analysis involves the inversion of the inductance matrix. After this analysis is complete, further analysis is done to remove the simplifying assumption and show the full derivation. Throughout, the derivations are divided into sections for the various types of synchronous machines: with a nontrivial zero axis and dampers (SMZk), with only a nontrivial zero axis (SMZ), with only dampers (SMk), or without either (SM).

Dynamical Equations without Inductances Derivatives

Premise

The following derivations assume that the inductances, though nonlinear, have negligible time derivatives. So, in taking the derivative of flux linkage, we get the derivative of current with an inductance factor. To solve for the time derivatives of currents, the inverse of the inductances are used as shown in (94).

$$\begin{aligned} &\underline{\lambda} \underset{\downarrow}{=} \underline{\underline{L}} \cdot \underline{i} \\ &\frac{d}{dt}\underline{\lambda} \underset{\downarrow}{=} \underline{\underline{L}} \cdot \frac{d}{dt}\underline{i} \\ &\frac{d}{dt}\underline{i} = \underline{\underline{L}}^{-1} \cdot \frac{d}{dt}\underline{\lambda} \end{aligned} \tag{94}$$

The inductance matrix inverse $\underline{\underline{L}}^{-1}$ is the main focus throughout these derivations.

Six Dynamics (SMZk)

Beginning with the governing voltage equations of a synchronous machine with damper windings and a nontrivial zero axis, we have (95) through (100), where variables subscripted with N have been referenced to the stator through the stator-to-rotor turns ratio, N_{sr}.

$$u_d = R_s i_d + \frac{d}{dt}\lambda_d - \lambda_q \omega_s \tag{95}$$

$$u_q = R_s i_q + \frac{d}{dt}\lambda_q + \lambda_d \omega_s \tag{96}$$

$$u_z = R_s i_z + \frac{d}{dt}\lambda_z \tag{97}$$

$$u_{fN} = R_{fN} i_{fN} + \frac{d}{dt}\lambda_{fN} \tag{98}$$

$$0 = R_{kdN} i_{kdN} + \frac{d}{dt}\lambda_{kdN} \tag{99}$$

$$0 = R_{kqN} i_{kqN} + \frac{d}{dt}\lambda_{kqN} \tag{100}$$

These six equations can be rearranged in terms of time derivatives of flux linkages and then combined into a single matrix equation. The zero axis does not need to be included in the matrix equation because it is not coupled with any other axis and would, therefore, not benefit from the matrix format. So, (95) through (100) become (101) and (102).

$$\frac{d}{dt}\begin{bmatrix} \lambda_d \\ \lambda_q \\ \lambda_{fN} \\ \lambda_{kdN} \\ \lambda_{kqN} \end{bmatrix} = \begin{bmatrix} u_d - R_s i_d + \lambda_q \omega_s \\ u_q - R_s i_q - \lambda_d \omega_s \\ u_{fN} - R_{fN} i_{fN} \\ -R_{kdN} i_{kdN} \\ -R_{kqN} i_{kqN} \end{bmatrix} \tag{101}$$

$$\frac{d}{dt}\lambda_z = u_z - R_s i_z \tag{102}$$

The flux linkages can be defined in terms of stator-referenced leakage (*l*) and mutual (*m*) inductances as shown in (103) and (104).

$$\begin{bmatrix} \lambda_d \\ \lambda_q \\ \lambda_{fN} \\ \lambda_{kdN} \\ \lambda_{kqN} \end{bmatrix} = \underbrace{\begin{bmatrix} L_{sl} + L_{md} & 0 & L_{md} & L_{md} & 0 \\ 0 & L_{sl} + L_{mq} & 0 & 0 & L_{mq} \\ L_{md} & 0 & L_{flN} + L_{md} & L_{md} & 0 \\ L_{md} & 0 & L_{md} & L_{kldN} + L_{md} & 0 \\ 0 & L_{mq} & 0 & 0 & L_{klqN} + L_{mq} \end{bmatrix}}_{\underline{\underline{L}}} \cdot \begin{bmatrix} i_d \\ i_q \\ i_{fN} \\ i_{kdN} \\ i_{kqN} \end{bmatrix} \tag{103}$$

$$\lambda_z = L_{sl} \cdot i_z \tag{104}$$

This relationship comes from the orthogonal nature of the D and Q axes, the symmetrical nature of the materials, and the use of the stator-to-rotor turns ratio, N_{sr}. To simplify the derivation, some symbolic substitutions are made and the inductance matrix in (103) becomes

$$\underline{\underline{L}} = \begin{bmatrix} (c+a) & 0 & a & a & 0 \\ 0 & (c+b) & 0 & 0 & b \\ a & 0 & (d+a) & a & 0 \\ a & 0 & a & (e+a) & 0 \\ 0 & b & 0 & 0 & (f+b) \end{bmatrix} : \begin{cases} a = L_{md} & d = L_{flN} \\ b = L_{mq} & e = L_{kldN} \\ c = L_{sl} & f = L_{klqN} \end{cases} . \tag{105}$$

The inverse of this matrix is

$$\underline{\underline{L}}^{-1} = \begin{bmatrix} \frac{de + a\cdot(d+e)}{r} & 0 & -\frac{ae}{r} & -\frac{ad}{r} & 0 \\ 0 & \frac{(b+f)}{s} & 0 & 0 & -\frac{b}{s} \\ -\frac{ae}{r} & 0 & \frac{ce + a\cdot(c+e)}{r} & -\frac{ac}{r} & 0 \\ -\frac{ad}{r} & 0 & -\frac{ac}{r} & \frac{cd + a\cdot(c+d)}{r} & 0 \\ 0 & -\frac{b}{s} & 0 & 0 & \frac{(b+c)}{s} \end{bmatrix} . \tag{106}$$

$$: \begin{cases} r = cde + a\cdot(de + c\cdot(d+e)) \\ s = cf + b\cdot(c+f) \end{cases}$$

We can further simplify this matrix with another set of substitutions:

$$\underline{\underline{L}}^{-1} = \begin{bmatrix} A & 0 & B & C & 0 \\ 0 & D & 0 & 0 & E \\ B & 0 & F & G & 0 \\ C & 0 & G & H & 0 \\ 0 & E & 0 & 0 & I \end{bmatrix} : \begin{cases} A = \frac{de + a\cdot(d+e)}{r} & D = \frac{(b+f)}{s} & G = -\frac{ac}{r} \\ B = -\frac{ae}{r} & E = -\frac{b}{s} & H = \frac{cd + a\cdot(c+d)}{r} \\ C = -\frac{ad}{r} & F = \frac{ce + a\cdot(c+e)}{r} & I = \frac{(b+c)}{s} \end{cases} . \tag{107}$$

So, the dynamical equations for a synchronous machine with dampers can be written as

$$\frac{d}{dt}\begin{bmatrix} i_d \\ i_q \\ i_{fN} \\ i_{kdN} \\ i_{kqN} \end{bmatrix} = \underline{\underline{L}}^{-1} \cdot \begin{bmatrix} u_d - R_s i_d + \lambda_q \omega_s \\ u_q - R_s i_q - \lambda_d \omega_s \\ u_{fN} - R_{fN} i_{fN} \\ -R_{kdN} i_{kdN} \\ -R_{kqN} i_{kqN} \end{bmatrix} \tag{108}$$

$$\frac{d}{dt}i_z = \frac{1}{L_{sl}}\left(u_z - R_s i_z\right), \tag{109}$$

where $\underline{\underline{L}}^{-1}$ is as defined in (105) through (107).

Without Zero Axis (SMk)

If the zero axis is always null (the machine is balanced, there is no access to the neutral line, or simply no current ever flows on the zero axis), then there is no reason to carry that dynamic through the simulation and the number of dynamics can be reduced to five. Because the zero axis is completely uncoupled with all other axes, we can simply remove (109). Therefore, the full set of dynamical equations for this machine is

$$\frac{d}{dt}\begin{bmatrix} i_d \\ i_q \\ i_{fN} \\ i_{kdN} \\ i_{kqN} \end{bmatrix} = \underline{\underline{L}}^{-1} \cdot \begin{bmatrix} u_d - R_s i_d + \lambda_q \omega_s \\ u_q - R_s i_q - \lambda_d \omega_s \\ u_{fN} - R_{fN} i_{fN} \\ -R_{kdN} i_{kdN} \\ -R_{kqN} i_{kqN} \end{bmatrix}, \tag{110}$$

where $\underline{\underline{L}}^{-1}$ is as defined in (105) through (107).

Without Dampers (SMZ)

If there are no damper bars but there is a zero axis, then the number of dynamics can be reduced to four. This will reduce the inductance matrix in (105) to

$$\underline{\underline{L}} = \begin{bmatrix} (c+a) & 0 & a \\ 0 & (c+b) & 0 \\ a & 0 & (d+a) \end{bmatrix} : \begin{cases} a = L_{md} \\ b = L_{mq} \\ c = L_{sl} \\ d = L_{flN} \end{cases} \tag{111}$$

which inverted becomes

$$\underline{\underline{L}}^{-1} = \begin{bmatrix} \frac{(d+a)}{p} & 0 & -\frac{a}{p} \\ 0 & \frac{1}{(c+b)} & 0 \\ -\frac{a}{p} & 0 & \frac{(c+a)}{p} \end{bmatrix} : p = cd + a \cdot (c+d). \tag{112}$$

This can be further simplified by substitution:

$$\underline{\underline{L}}^{-1} = \begin{bmatrix} A & 0 & B \\ 0 & C & 0 \\ B & 0 & D \end{bmatrix} : \begin{cases} A = \frac{(d+a)}{p} & C = \frac{1}{(c+b)} \\ B = -\frac{a}{p} & D = \frac{(c+a)}{p} \end{cases}. \tag{113}$$

Note that the variables *A*, *B*, *C*, and *D* are not defined the same as in (107). The dynamic equations are then

$$\begin{cases} \frac{d}{dt}\begin{bmatrix} i_d \\ i_q \\ i_{fN} \end{bmatrix} = \underline{\underline{L}}^{-1} \cdot \begin{bmatrix} u_d - R_s i_d + \lambda_q \omega_s \\ u_q - R_s i_q - \lambda_d \omega_s \\ u_{fN} - R_{fN} i_{fN} \end{bmatrix} \\ \frac{d}{dt} i_z = \frac{1}{L_{sl}} (u_z - R_s i_z) \end{cases}. \tag{114}$$

Without Zero Axis or Dampers (SM)

If there is no zero axis and there are no damper bars, then the dynamics reduce to three:

$$\frac{d}{dt}\begin{bmatrix} i_d \\ i_q \\ i_{fN} \end{bmatrix} = \underline{\underline{L}}^{-1} \cdot \begin{bmatrix} u_d - R_s i_d + \lambda_q \omega_s \\ u_q - R_s i_q - \lambda_d \omega_s \\ u_{fN} - R_{fN} i_{fN} \end{bmatrix}, \tag{115}$$

where $\underline{\underline{L}}^{-1}$ is as defined in (111) through (113).

Simulation Speeds

There is value to using the appropriate model. Saving on states does significantly reduce the time to process. A test was run wherein each of the above four models was run for 10 s of simulation time, three times each. The results are shown in Figure 69.

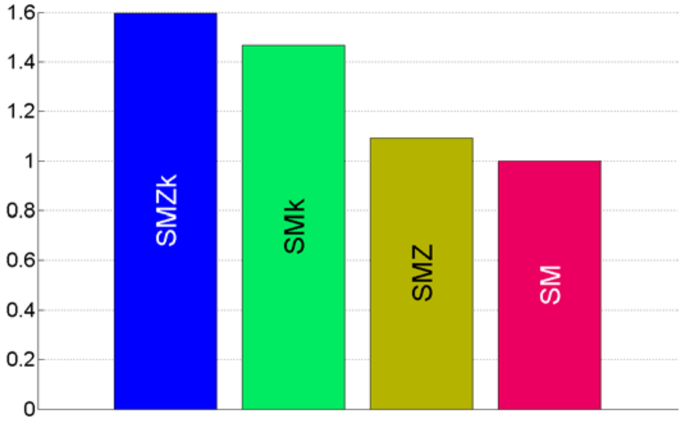

Figure 69. Normalized mean simulation times for four machine types.

Dynamical Equations with Inductance Derivatives

Premise of Exact Solution

If the assumption of negligible time derivatives of inductances were no longer made, then the derivation in (94) would change to

$$\begin{aligned}
&\underline{\lambda} \underset{\downarrow}{=} \underline{\underline{L}} \cdot \underline{i} \\
&\frac{d}{dt}\underline{\lambda} \underset{\downarrow}{=} \frac{d}{dt}\underline{\underline{L}} \cdot \underline{i} + \underline{\underline{L}} \cdot \frac{d}{dt}\underline{i} \\
&\frac{d}{dt}\underline{\lambda} \underset{\downarrow}{=} \frac{d}{d\underline{i}}\underline{\underline{L}} \cdot \frac{d}{dt}\underline{i} \cdot \underline{i} + \underline{\underline{L}} \cdot \frac{d}{dt}\underline{i} \\
&\frac{d}{dt}\underline{i} = \left(\frac{d}{d\underline{i}}\underline{\underline{L}} \cdot \underline{i} + \underline{\underline{L}}\right)^{-1} \cdot \frac{d}{dt}\underline{\lambda}
\end{aligned} \qquad (116)$$

This is the explicit derivation of the time derivative of current. (Note that not including the effects of time-changing inductance can cause significant error, depending on the current magnitude.) This derivation has the same conclusion as (94) except that the apparent inductance matrix has been replaced by the incremental inductance matrix:

$$\underline{\underline{L_{inc}}} = \frac{d}{d\underline{i}}\underline{\underline{L}} \cdot \underline{i} + \underline{\underline{L}}\,. \qquad (117)$$

Full, Six-dynamics Derivation of Exact Solution

To develop the dynamical equations, we begin by rewriting (103) in a systems of equations format, as in (118), and then rearranging it, as in (119).

$$\begin{cases} \lambda_d = L_{sl} \cdot i_d + L_{md} \cdot i_d + L_{md} \cdot i_{fN} + L_{md} \cdot i_{kdN} \\ \lambda_q = L_{sl} \cdot i_q + L_{mq} \cdot i_q + L_{mq} \cdot i_{kqN} \\ \lambda_z = L_{sl} \cdot i_z \\ \lambda_{fN} = L_{md} \cdot i_d + L_{flN} \cdot i_{fN} + L_{md} \cdot i_{fN} + L_{md} \cdot i_{kdN} \\ \lambda_{kdN} = L_{md} \cdot i_d + L_{md} \cdot i_{fN} + L_{kldN} \cdot i_{kdN} + L_{md} \cdot i_{kdN} \\ \lambda_{kqN} = L_{mq} \cdot i_q + L_{klqN} \cdot i_{kqN} + L_{mq} \cdot i_{kqN} \end{cases} \tag{118}$$

$$\begin{cases} \lambda_d = L_{sl} \cdot i_d + L_{md} \cdot \left(i_d + i_{fN} + i_{kdN}\right) \\ \lambda_q = L_{sl} \cdot i_q + L_{mq} \cdot \left(i_q + i_{kqN}\right) \\ \lambda_z = L_{sl} \cdot i_z \\ \lambda_{fN} = L_{flN} \cdot i_{fN} + L_{md} \cdot \left(i_d + i_{fN} + i_{kdN}\right) \\ \lambda_{kdN} = L_{kldN} \cdot i_{kdN} + L_{md} \cdot \left(i_d + i_{fN} + i_{kdN}\right) \\ \lambda_{kqN} = L_{klqN} \cdot i_{kqN} + L_{mq} \cdot \left(i_q + i_{kqN}\right) \end{cases} \tag{119}$$

Then, we begin to take the derivative of the equations, as in (120).

$$\begin{cases} \frac{d}{dt}\lambda_d = L_{sl} \cdot \frac{di_d}{dt} + \frac{dL_{md}}{dt} \cdot \left(i_d + i_{fN} + i_{kdN}\right) + L_{md} \cdot \left(\frac{di_d}{dt} + \frac{di_{fN}}{dt} + \frac{di_{kdN}}{dt}\right) \\ \frac{d}{dt}\lambda_q = L_{sl} \cdot \frac{di_q}{dt} + \frac{dL_{mq}}{dt} \cdot \left(i_q + i_{kqN}\right) + L_{mq} \cdot \left(\frac{di_q}{dt} + \frac{di_{kqN}}{dt}\right) \\ \frac{d}{dt}\lambda_z = L_{sl} \cdot \frac{di_z}{dt} \\ \frac{d}{dt}\lambda_{fN} = L_{flN} \cdot \frac{di_{fN}}{dt} + \frac{dL_{md}}{dt} \cdot \left(i_d + i_{fN} + i_{kdN}\right) + L_{md} \cdot \left(\frac{di_d}{dt} + \frac{di_{fN}}{dt} + \frac{di_{kdN}}{dt}\right) \\ \frac{d}{dt}\lambda_{kdN} = L_{kldN} \cdot \frac{di_{kdN}}{dt} + \frac{dL_{md}}{dt} \cdot \left(i_d + i_{fN} + i_{kdN}\right) + L_{md} \cdot \left(\frac{di_d}{dt} + \frac{di_{fN}}{dt} + \frac{di_{kdN}}{dt}\right) \\ \frac{d}{dt}\lambda_{kqN} = L_{klqN} \cdot \frac{di_{kqN}}{dt} + \frac{dL_{mq}}{dt} \cdot \left(i_q + i_{kqN}\right) + L_{mq} \cdot \left(\frac{di_q}{dt} + \frac{di_{kqN}}{dt}\right) \end{cases}$$

$$: \begin{cases} \frac{dL_{md}}{dt} = \frac{dL_{md}}{di_d} \cdot \frac{di_d}{dt} + \frac{dL_{md}}{di_q} \cdot \frac{di_q}{dt} + \frac{dL_{md}}{di_{fN}} \cdot \frac{di_{fN}}{dt} + \frac{dL_{md}}{di_{kdN}} \cdot \frac{di_{kdN}}{dt} + \frac{dL_{md}}{di_{kqN}} \cdot \frac{di_{kqN}}{dt} \\ \frac{dL_{mq}}{dt} = \frac{dL_{mq}}{di_d} \cdot \frac{di_d}{dt} + \frac{dL_{mq}}{di_q} \cdot \frac{di_q}{dt} + \frac{dL_{mq}}{di_{fN}} \cdot \frac{di_{fN}}{dt} + \frac{dL_{mq}}{di_{kdN}} \cdot \frac{di_{kdN}}{dt} + \frac{dL_{mq}}{di_{kqN}} \cdot \frac{di_{kqN}}{dt} \end{cases} \tag{120}$$

Given that the magnetizing inductances L_{md} and L_{mq} can be defined in terms of the magnetizing currents i_{md} and i_{mq} alone, the derivatives of inductance with respect to the components of the magnetizing currents are equivalent. This allows us to group the current derivatives of inductance:

$$\begin{cases} \dfrac{dL_{md}}{dt} = \dfrac{dL_{md}}{di_{md}} \cdot \left(\dfrac{di_d}{dt} + \dfrac{di_{fN}}{dt} + \dfrac{di_{kdN}}{dt} \right) + \dfrac{dL_{md}}{di_{mq}} \cdot \left(\dfrac{di_q}{dt} + \dfrac{di_{kqN}}{dt} \right) \\ \dfrac{dL_{mq}}{dt} = \dfrac{dL_{mq}}{di_{md}} \cdot \left(\dfrac{di_d}{dt} + \dfrac{di_{fN}}{dt} + \dfrac{di_{kdN}}{dt} \right) + \dfrac{dL_{mq}}{di_{mq}} \cdot \left(\dfrac{di_q}{dt} + \dfrac{di_{kqN}}{dt} \right) \end{cases} . \tag{121}$$

Substituting (121) into the first line of (120), we get

$$\begin{aligned} \frac{d}{dt}\lambda_d = {} & L_{sl} \cdot \frac{di_d}{dt} + \left(\frac{dL_{md}}{di_{md}} \cdot \left(\frac{di_d}{dt} + \frac{di_{fN}}{dt} + \frac{di_{kdN}}{dt} \right) + \frac{dL_{md}}{di_{mq}} \cdot \left(\frac{di_q}{dt} + \frac{di_{kqN}}{dt} \right) \right) \cdot i_{md} \\ & + L_{md} \cdot \left(\frac{di_d}{dt} + \frac{di_{fN}}{dt} + \frac{di_{kdN}}{dt} \right) \end{aligned} . \tag{122}$$

which can be rearranged to

$$\begin{aligned} \frac{d}{dt}\lambda_d = {} & L_{sl} \cdot \frac{di_d}{dt} + \frac{dL_{md}}{di_{md}} \cdot i_{md} \cdot \left(\frac{di_d}{dt} + \frac{di_{fN}}{dt} + \frac{di_{kdN}}{dt} \right) + \frac{dL_{md}}{di_{mq}} \cdot i_{md} \cdot \left(\frac{di_q}{dt} + \frac{di_{kqN}}{dt} \right) \\ & + L_{md} \cdot \left(\frac{di_d}{dt} + \frac{di_{fN}}{dt} + \frac{di_{kdN}}{dt} \right) : \begin{cases} i_{md} = i_d + i_{fN} + i_{kdN} \\ i_{mq} = i_q + i_{kqN} \end{cases} \end{aligned} \tag{123}$$

and then

$$\frac{d}{dt}\lambda_d = L_{sl} \cdot \frac{di_d}{dt} + \left(L_{md} + \frac{dL_{md}}{di_{md}} \cdot i_{md} \right) \cdot \left(\frac{di_d}{dt} + \frac{di_{fN}}{dt} + \frac{di_{kdN}}{dt} \right) + \left(\frac{dL_{md}}{di_{mq}} \cdot i_{md} \right) \cdot \left(\frac{di_q}{dt} + \frac{di_{kqN}}{dt} \right) . \tag{124}$$

Applying this same process to all of the lines in (120), we get (125).

$$\begin{cases} \frac{d}{dt}\lambda_d = L_{sl}\cdot\frac{di_d}{dt} + \left(L_{md} + \frac{dL_{md}}{di_{md}}\cdot i_{md}\right)\cdot\left(\frac{di_d}{dt} + \frac{di_{fN}}{dt} + \frac{di_{kdN}}{dt}\right) + \left(\frac{dL_{md}}{di_{mq}}\cdot i_{md}\right)\cdot\left(\frac{di_q}{dt} + \frac{di_{kqN}}{dt}\right) \\ \frac{d}{dt}\lambda_q = L_{sl}\cdot\frac{di_q}{dt} + \left(\frac{dL_{mq}}{di_{md}}\cdot i_{mq}\right)\cdot\left(\frac{di_d}{dt} + \frac{di_{fN}}{dt} + \frac{di_{kdN}}{dt}\right) + \left(L_{mq} + \frac{dL_{mq}}{di_{mq}}\cdot i_{mq}\right)\cdot\left(\frac{di_q}{dt} + \frac{di_{kqN}}{dt}\right) \\ \frac{d}{dt}\lambda_z = L_{sl}\cdot\frac{di_z}{dt} \\ \frac{d}{dt}\lambda_{fN} = L_{flN}\cdot\frac{di_{fN}}{dt} + \left(L_{md} + \frac{dL_{md}}{di_{md}}\cdot i_{md}\right)\cdot\left(\frac{di_d}{dt} + \frac{di_{fN}}{dt} + \frac{di_{kdN}}{dt}\right) + \left(\frac{dL_{md}}{di_{mq}}\cdot i_{md}\right)\cdot\left(\frac{di_q}{dt} + \frac{di_{kqN}}{dt}\right) \\ \frac{d}{dt}\lambda_{kdN} = L_{kldN}\cdot\frac{di_{kdN}}{dt} + \left(L_{md} + \frac{dL_{md}}{di_{md}}\cdot i_{md}\right)\cdot\left(\frac{di_d}{dt} + \frac{di_{fN}}{dt} + \frac{di_{kdN}}{dt}\right) + \left(\frac{dL_{md}}{di_{mq}}\cdot i_{md}\right)\cdot\left(\frac{di_q}{dt} + \frac{di_{kqN}}{dt}\right) \\ \frac{d}{dt}\lambda_{kqN} = L_{klqN}\cdot\frac{di_{kqN}}{dt} + \left(\frac{dL_{mq}}{di_{md}}\cdot i_{mq}\right)\cdot\left(\frac{di_d}{dt} + \frac{di_{fN}}{dt} + \frac{di_{kdN}}{dt}\right) + \left(L_{mq} + \frac{dL_{mq}}{di_{mq}}\cdot i_{mq}\right)\cdot\left(\frac{di_q}{dt} + \frac{di_{kqN}}{dt}\right) \end{cases} \tag{125}$$

This can now be turned back into a matrix format:

$$\frac{d}{dt}\begin{bmatrix} \lambda_d \\ \lambda_q \\ \lambda_z \\ \lambda_{fN} \\ \lambda_{kdN} \\ \lambda_{kqN} \end{bmatrix} = \underbrace{\left(\begin{bmatrix} u\,v\,0\,u\,u\,v \\ w\,x\,0\,w\,w\,x \\ 0\,0\,0\,0\,0\,0 \\ u\,v\,0\,u\,u\,v \\ u\,v\,0\,u\,u\,v \\ w\,x\,0\,w\,w\,x \end{bmatrix} + \underline{\underline{L}}\right)}_{\underline{\underline{M}}}\cdot\frac{d}{dt}\begin{bmatrix} i_d \\ i_q \\ i_z \\ i_{fN} \\ i_{kdN} \\ i_{kqN} \end{bmatrix}, \tag{126}$$

where

$$\begin{aligned} u &= \frac{dL_{md}}{di_{md}}\cdot i_{md} \\ v &= \frac{dL_{md}}{di_{mq}}\cdot i_{md} \\ w &= \frac{dL_{mq}}{di_{md}}\cdot i_{mq} \\ x &= \frac{dL_{mq}}{di_{mq}}\cdot i_{mq} \end{aligned}\ . \tag{127}$$

Before moving further, it is noteworthy that wherever there is a magnetizing inductance in (103), the current derivative of that inductance times the current is added to it in (126). Given the general bell-curve shape of inductance surfaces over D and Q currents, these derivatives are normally negative. Therefore, including the time derivatives has the effect of weakening the inductances. So, if a voltage were applied to the field winding of a synchronous machine, the field current would rise more quickly if these derivative terms are included.

In solving for the time derivatives of current, the inverse of the $\underline{\underline{M}}$ matrix must be taken, instead of the inverse of $\underline{\underline{L}}$. The $\underline{\underline{M}}$ matrix is a full matrix and, therefore, much more difficult to invert. However, because the Z axis is independent of all other states, at least it can be removed from the matrix equation for simplification.

$$\begin{cases} \dfrac{d}{dt}\begin{bmatrix} \lambda_d \\ \lambda_q \\ \lambda_{fN} \\ \lambda_{kdN} \\ \lambda_{kqN} \end{bmatrix} = \underbrace{\left(\begin{bmatrix} u\,v\,u\,u\,v \\ w\,x\,w\,w\,x \\ u\,v\,u\,u\,v \\ u\,v\,u\,u\,v \\ w\,x\,w\,w\,x \end{bmatrix} + \underline{\underline{L}} \right)}_{\underline{\underline{M}}} \cdot \dfrac{d}{dt}\begin{bmatrix} i_d \\ i_q \\ i_{fN} \\ i_{kdN} \\ i_{kqN} \end{bmatrix} \\ \dfrac{d}{dt}\lambda_z = L_{sl} \cdot \dfrac{d}{dt} i_z \end{cases} \tag{128}$$

The matrix $\underline{\underline{M}}$ can then be expressed as

$$\underline{\underline{M}} = \begin{bmatrix} a+c+u & v & a+u & a+u & v \\ w & b+c+x & w & w & b+x \\ a+u & v & a+d+u & a+u & v \\ a+u & v & a+u & a+e+u & v \\ w & b+x & w & w & b+f+x \end{bmatrix}, \tag{129}$$

where *a*, *b*, *c*, *d*, *e*, and *f* are as defined in (105). By substitution, the matrix of (129) can be simplified to

$$\underline{\underline{M}} = \begin{bmatrix} G & v & A & A & v \\ w & C & w & w & B \\ A & v & D & A & v \\ A & v & A & E & v \\ w & B & w & w & F \end{bmatrix} : \begin{cases} A = a+u \\ B = b+x \\ C = B+c \\ D = A+d \\ E = A+e \\ F = B+f \\ G = A+c \end{cases}, \tag{130}$$

where the capitalized variables are newly defined and not the same as in (107). The analytical inverse of this matrix is exceedingly complicated, even with the simplifying substitutions made thus far. This is due in large part to the non-sparse nature of the matrix. So, this method of including the time-derivatives of inductances is not recommended.

Premise of Approximate Solution

Because the exact solution is prohibitively complicated, there is good reason to look for a close approximation. The basis of the approximate solution is the use of the observed time-derivative of inductance, as shown in (131). If the time step is very small, then this approximation is quite reasonable:

$$\begin{gathered}
\underline{\lambda} \underset{\downarrow}{=} \underline{\underline{L}} \cdot \underline{i} \\
\frac{d}{dt}\underline{\lambda} \underset{\downarrow}{=} \frac{d}{dt}\underline{\underline{L}} \cdot \underline{i} + \underline{\underline{L}} \cdot \frac{d}{dt}\underline{i} \\
\frac{d}{dt}\underline{i} = \underline{\underline{L}}^{-1} \cdot \left(\frac{d}{dt}\underline{\lambda} - \frac{d}{dt}\underline{\underline{L}} \cdot \underline{i} \right)
\end{gathered} \quad . \tag{131}$$

Here, the time derivative of inductance must be approximated. Note that (131) is a modified version of (116).

Full, Six-dynamics Derivation of Approximate Solution

Starting with (120) and rearranging, we have

$$\begin{cases} \frac{d}{dt}\lambda_d - \frac{dL_{md}}{dt}\cdot i_{md} = L_{sl}\cdot\frac{di_d}{dt} + L_{md}\cdot\left(\frac{di_d}{dt}+\frac{di_{fN}}{dt}+\frac{di_{kdN}}{dt}\right) \\ \frac{d}{dt}\lambda_q - \frac{dL_{mq}}{dt}\cdot i_{mq} = L_{sl}\cdot\frac{di_q}{dt} + L_{mq}\cdot\left(\frac{di_q}{dt}+\frac{di_{kqN}}{dt}\right) \\ \frac{d}{dt}\lambda_z = L_{sl}\cdot\frac{di_z}{dt} \\ \frac{d}{dt}\lambda_{fN} - \frac{dL_{md}}{dt}\cdot i_{md} = L_{flN}\cdot\frac{di_{fN}}{dt} + L_{md}\cdot\left(\frac{di_d}{dt}+\frac{di_{fN}}{dt}+\frac{di_{kdN}}{dt}\right) \\ \frac{d}{dt}\lambda_{kdN} - \frac{dL_{md}}{dt}\cdot i_{md} = L_{kldN}\cdot\frac{di_{kdN}}{dt} + L_{md}\cdot\left(\frac{di_d}{dt}+\frac{di_{fN}}{dt}+\frac{di_{kdN}}{dt}\right) \\ \frac{d}{dt}\lambda_{kqN} - \frac{dL_{mq}}{dt}\cdot i_{mq} = L_{klqN}\cdot\frac{di_{kqN}}{dt} + L_{mq}\cdot\left(\frac{di_q}{dt}+\frac{di_{kqN}}{dt}\right) \end{cases} . \tag{132}$$

This leads us to a solution that is very similar to (108) but includes these derivatives of inductances:

$$\frac{d}{dt}\begin{bmatrix} i_d \\ i_q \\ i_{fN} \\ i_{kdN} \\ i_{kqN} \end{bmatrix} = \underline{\underline{L}}^{-1}\cdot\begin{bmatrix} u_d - R_s i_d + \lambda_q\omega_s - \frac{dL_{md}}{dt}\cdot i_{md} \\ u_q - R_s i_q - \lambda_d\omega_s - \frac{dL_{mq}}{dt}\cdot i_{mq} \\ u_{fN} - R_{fN} i_{fN} - \frac{dL_{md}}{dt}\cdot i_{md} \\ -R_{kdN} i_{kdN} - \frac{dL_{md}}{dt}\cdot i_{md} \\ -R_{kqN} i_{kqN} - \frac{dL_{mq}}{dt}\cdot i_{mq} \end{bmatrix}, \tag{133}$$

where $\underline{\underline{L}}^{-1}$ is as defined in (105) through (107). Because the $\underline{\underline{L}}$ matrix is not affected by this method, all of the solutions already found for the various dynamics are still valid, given the inclusion of these time derivatives of inductances. Note that (109) still applies for the zero axis.

A close approximation to the derivative can be made using the Laplace gain

$$\frac{s}{1+Ts}, \tag{134}$$

where *T* is very small. As *T* approaches zero, the gain approaches *s*, which is the Laplace form of the derivative. The limiting factor here is that making *T* very small forces the simulation to take smaller time steps or suffer instability.

Power Analysis

The dynamic equations for six states as seen in (101) and (102) are restated here in terms of voltage:

$$\begin{aligned}
u_d &= R_s i_d - \lambda_q \omega_s + \frac{d}{dt}\lambda_d \\
u_q &= R_s i_q + \lambda_d \omega_s + \frac{d}{dt}\lambda_q \\
u_z &= R_s i_z + \frac{d}{dt}\lambda_z \\
u_{fN} &= R_{fN} i_{fN} + \frac{d}{dt}\lambda_{fN} \\
0 &= R_{kdN} i_{kdN} + \frac{d}{dt}\lambda_{kdN} \\
0 &= R_{kqN} i_{kqN} + \frac{d}{dt}\lambda_{kqN}
\end{aligned} \tag{135}$$

Power is the product of voltage and current. So, (135) becomes (72) when multiplied by the respective currents.

$$\begin{aligned}
u_d i_d &= R_s {i_d}^2 - \lambda_q \omega_s i_d + \frac{d}{dt}\lambda_d i_d \\
u_q i_q &= R_s {i_q}^2 + \lambda_d \omega_s i_q + \frac{d}{dt}\lambda_q i_q \\
u_z i_z &= R_s {i_z}^2 + \frac{d}{dt}\lambda_z i_z \\
u_{fN} i_{fN} &= R_{fN} {i_{fN}}^2 + \frac{d}{dt}\lambda_{fN} i_{fN} \\
0 &= R_{kdN} {i_{kdN}}^2 + \frac{d}{dt}\lambda_{kdN} i_{kdN} \\
0 &= R_{kqN} {i_{kqN}}^2 + \frac{d}{dt}\lambda_{kqN} i_{kqN}
\end{aligned} \tag{72}$$

This set of equations is now a set of power balance equations. The terms on the left represent electrical power flowing into the system. The resistive terms represent the power losses. The second terms on the right of the first two equations represent the mechanical power flowing out of the system. The last terms in each equation represent the power stored in the system. So, the electrical, thermal, magnetic, and mechanical powers flowing into the system are respectively

$$p_e = u_d i_d + u_q i_q + u_z i_z + u_{fN} i_{fN} \tag{73}$$

$$p_Q = -\left(R_s i_d{}^2 + R_s i_q{}^2 + R_s i_z{}^2 + R_{fN} i_{fN}{}^2 + R_{kdN} i_{kdN}{}^2 + R_{kqN} i_{kqN}{}^2\right) \tag{75}$$

$$p_H = -\left(\frac{d\lambda_d}{dt} i_d + \frac{d\lambda_q}{dt} i_q + \frac{d\lambda_z}{dt} i_z + \frac{d\lambda_{fN}}{dt} i_{fN} + \frac{d\lambda_{kdN}}{dt} i_{kdN} + \frac{d\lambda_{kqN}}{dt} i_{kqN}\right). \tag{76}$$

$$p_m = \underbrace{\left(\lambda_q i_d - \lambda_d i_q\right)}_{\tau_s} \omega_s \Rightarrow \tau_s \omega_s \Rightarrow \left(\frac{\tau}{P/2}\right)\left(\omega \frac{P}{2}\right) \Rightarrow \tau\omega \tag{74}$$

The mechanical power stored in the system comes from the moment of inertia, *J*, and is found by

$$p_J = \left(-J \cdot \frac{d\omega}{dt}\right) \cdot \omega. \tag{141}$$

The machine is treated as a node, and all stored energy is external to the system. So, the minus in (141) signifies that the power is leaving the node and being stored in the inertia of the machine. The power balance equation is

$$0 = p_e + p_Q + p_H + p_m + p_J\ . \tag{77}$$

Given a shaft speed, ω, the torque extraction (oriented into the machine) would be the sum of all the component torques:

$$\tau_{ex} = \left(\lambda_q i_d - \lambda_d i_q\right) + \left(-J \cdot \frac{d\omega}{dt}\right). \tag{143}$$

REFERENCES

[1] J. M. Pointon, “Thermal Management of Electromechanical Actuation on an All-Electric Aircraft,” M.S. thesis, Cranfield University, Bedfordshire, UK, 2007.

[2] I. Moir, “The All-Electric Aircraft - Major Challenges”, *Proceedings of the IEE Colloquium on All-Electric Aircraft*, 17 June 1998, Ref. no. 1998/260, The Institution of Electrical Engineers (IEE), Savoy Place, London, UK.

[3] C. R. Spitzer, R. V. Hood, “The All Electric Airplane - Benefits and Challenges,” *Proceedings of the Aerospace Congress and Exposition*, Anaheim, CA; United States; 25-28 Oct. 1982, SAE 821434, Society of Automotive Engineers (SAE), Warrendale, PA, USA.

[4] S. L. Botten, C. R. Whitley, and A. D. King, "Flight Control Actuation for Next Generation All-Electric Aircraft", *Technology Review Journal*, vol. Fall/Winter 2000, pp. 55-68.

[5] N. Bataille, “Electrically Powered Control Surface Actuation (MS thesis),” Cranfield University, Bedfordshire, UK. 2006.

[6] M. J. Cronin, "The All Electric Airplane Revisited", *Proceedings of the Aerospace Technology Conference and Exposition*, Anaheim, CA, 3-6 Oct. 1988, SAE 881407, Society of Automotive Engineers (SAE), Warrendale, PA, USA.

[7] Jensen, S. C., Jenney, G. D., Raymond, B. and Dawson, D. (2000), "Flight Test Experience with an Electromechanical Actuator on the F-18 Systems Research Aircraft", *Proceedings of the 19th AIAA Digital Avionics Systems Conference*, 7-13 Oct. 2000,

Philadelphia, PA, USA, American Institute of Aeronautics and Astronautics (AIAA), Reston, VA, USA.

[8] Rubertus, D. P., Hunter, L. D. and Cecere, G. J. (1984), "Electromechanical Actuation Technology for the All-Electric Aircraft", *IEEE Transactions on Aerospace and Electronic Systems*, vol. AES-20, pp. 243-249.

[9] Charrier, J. J. and Kulshreshtha, A. (2007), “Electric Actuation for Flight & Engine Control System: Evolution, Current Trends & Future Challenges,” AIAA 2007-1391, *American Institute of Aeronautics and Astronautics* (AIAA), Reston, VA, USA.

[10] Bland, T. J. and Funke, K. D. (1992), "Advanced Cooling for High Power Electric Actuators", *SAE, Aerospace Atlantic Conference*, Dayton, OH; USA; 7-10 Apr. 1992, SAE 921022, Society of Automotive Engineers (SAE), Warrendale, PA, USA.

[11] Mazda, F. (2003), *Power Electronics Handbook*, 3rd ed., Elsevier Science, Oxford, UK.

[12] Schneider, M. G., Thomson, S. M., Bland, T. J. and Yerkes, K. L. (1994), “Test Results of Reflux-Cooled Electromechanical Actuator,” SAE 942176, *Society of Automotive Engineers* (SAE), Warrendale, PA, USA.

[13] Gernert, N. J., Sarraf, D. B. and Steinberg, M. (1992), “A Thermal Analysis of an F/A-18 Wing Section for Actuator Thermal Management,” SAE 921023, *Society of Automotive Engineers* (SAE), Warrendale, PA, USA.

[14] S. J. Cutts, “A collaborative approach to the More Electric Aircraft,” *Power Electronics, Machines and Drives, 2002. International Conference on* (Conf. Publ. No. 487), University of Bath, UK, 2002, pp. 223-228.

[15] “Superconducting motors could propel all-electric aircraft,” *Drives&Controls*, July 2007. Online. http://www.drives.co.uk/fullstory.asp?id=2033, Accessed: 4/18/2012.

[16] K. McCarthy et al., “A Reduced-Order Enclosure Radiation Modeling Technique for Aircraft Actuators,” *SAE Power Systems Conference*, Fort Worth, TX, 2010, SAE Technical Paper 2010-01-1741, 2010. doi: 10.4271/2010-01-1741

[17] M. J. Melfi et al., "Permanent-Magnet Motors for Energy Savings in Industrial Applications," *IEEE Trans. Ind. Appl.*, vol. 44, no. 5, pp. 1360-1366, Sept.-oct. 2008.

[18] K. L. Shi et al., "Modeling and Simulation of the Three-phase Induction Motor Using Simulink," *Int. J. Elect. Enging. Educ.*, vol. 36, pp. 163-172, Manchester U. P., Great Britain, 1999.

[19] M. A. Mohamed and M. H. Nagrial, "Modelling and Simulation of Vector-controlled Reluctance Motors Drive System," *International Conference on Simulation*, No. 457, pp. 380-384, ISBN: 0-85296-709-8, 1998.

[20] F. Sun et al., "Modeling and Simulation of Vector Control AC Motor Used by Electric Vehicle," *Journal of Asian Electric Vehicles,* vol. 3, No. 1, pp. 669-672, Asian Electric Vehicle Society, 2005.

[21] N. N. Soe, "Dynamic Modeling and Simulation of Three-phase Small Power Induction Motor," *World Academy of Science, Engineering and Technology*, vol. 42, No. 79, pp. 421-424, 2008.

[22] T. A. Lipo and A. Consoli, “Modeling and Simulation of Induction Motors with Saturable Leakage Reactances,” *IEEE Trans. Ind. Appl.*, vol. IA-20, no. 1, pp. 180-189, Jan. 1984.

[23] D. Dolinar et al., “Calculation of two-axis induction motor model parameters using finite elements,” *IEEE Trans. Energy Convers.*, vol. 12, no. 2, pp. 133-142, Jun. 1997.

[24] E. E. Topcu et al., “Simplified numerical solution of electromechanical systems by look-up tables,” *Mechatronics*, vol. 18, no. 10, pp. 559-565, Dec. 2008.

[25] A. H. Fitzgerald et al., *Electric Machinery*, 6th ed., NY: McGraw-Hill, 2003.

[26] H. Jianhui et al., "Finite element calculation of the saturation DQ-axes inductance for a direct drive PM synchronous motor considering cross-magnetization," *Power Electronics and Drive Systems*, The Fifth International Conference on, vol.1, no., pp. 677- 681 vol.1, 17-20 Nov. 2003.

[27] G. Sefkat, "Investigating Static and Dynamic Characteristics of Electromechanical Actuators (EMA) With MATLAB GUIs," *Computer Applications in Engineering Education*, vol. 18, No. 2, pp. 383-396, Wiley, 2008.

[28] P. Milanfar, J. Lang, "Monitoring the thermal condition of permanent-magnet synchronous motors," *IEEE Trans. Aerosp. Electron. Syst.*, vol.32, no.4, pp.1421-1429, Oct 1996, doi: 10.1109/7.543863.

[29] “Temperature coefficient of resistance,” All About Circuits, Online. http://www.allaboutcircuits.com/vol_1/chpt_12/6.html, Accessed: 4/18/2012.

[30] S. Campbell and H. A. Toliyat, *DSP-Based Electromechanical Motion Control*. CRC Press, 2003, pp. 209-222. Available: http://www.crcnetbase.com/doi/abs/10.1201/9780203486337.ch10

[31] Runge C. “Über empirische Funktionen und die Interpolation zwischen äquidistanten Ordinaten.” *Zeitschrift für Mathematik und Physik*. 1901. pp. 46:224–243. Available at: www.archive.org. Accessed November 22, 2013.

[32] M. Riedmiller, "Rprop - Description and Implementation Details: Technical Report," *Inst. f. Logik, Komplexität u. Deduktionssysteme*, 1994.

[33] J. F. Reynaud and P. Pillay, "Modeling of saturation effects in the magnetizing branch of an induction motor using PSpice," *Southeastcon '92, Proceedings., IEEE* , vol. 2, pp. 513-516, 12-15 Apr 1992.

[34] V. Petrović and A. M. Stanković, "Modeling of PM synchronous motors for control and estimation tasks," *Decision and Control, 2001. Proceedings of the 40th IEEE Conference* on, pp. 2229-2234, vol. 3, 2001.

[35] Y. Yan, J. Zhu, and Y. Guo, “Space vector modulated direct torque control of PM synchronous motor with initial rotor estimation,” *Proceedings of the Australasian Universities Power Engineering Conference*, Melbourne, Australia, pp. 1-6, 2006.

[36] F. Messai et al., “Nonlinear Modeling & Simulation of a Four-phase Switched Reluctance Generator (SRG DS 8/6) Under Matlab/Simulink Environment,” *Canadian Journal on Electrical and Electronics Engineering*, vol. 3, no. 6, pp. 266-270, Jul., 2012.

[37] Y. Ying et al., “Space Vector Modulated Direct Torque Control of PM Synchronous Motor with Initial Rotor Estimation,” *Proceedings of the Australasian Universities Power Engineering Conference,* Melbourne, Australia, 2006, pp. 1-6.

[38] D. Woodburn et al., “Dynamic Heat Generation Modeling of High Performance Electromechanical Actuator,” *IEEE Trans. Aerosp. Electron. Syst.*, submitted for publication.

[39] G. Stumberger et al., “Evaluation of saturation and cross-magnetization effects in interior permanent magnet synchronous motor,” *IEEE Trans. Ind. Appl.*, vol. 39, no. 5, pp. 1264-1271, Oct., 2003.

[40] D. Woodburn et al., “Novel Nonlinear Inductance Modeling of Permanent Magnet Motor,” to be submitted.

[41] Ion Boldea, *Synchronous Generators: The Electric Generators Handbook*. p. 5-21, CRC Press, 2010.

[42] D. Torrey et al., "Analytical modelling of variable-reluctance machine magnetisation characteristics," *Electric Power Applications, IEE Proceedings*, vol. 142, no. 1, pp. 14, Jan 1995.

[43] S. Mir et al., "Switched reluctance motor modeling with on-line parameter identification," *Industry Applications, IEEE Transactions on*, vol. 34, no. 4, pp. 776,783, July-Aug. 1998.

[44] Eric W. Weisstein, "Logistic Equation." From *MathWorld--A Wolfram Web Resource*. http://mathworld.wolfram.com/LogisticEquation.html.

[45] A. Pawlak, *Sensors and Actuators in Mechatronics: Design and Applications*, p. 102, CRC Press, July 2006.